RÉPUBLIQUE FRANÇAISE
Liberté Égalité Fraternité

Université de Toulouse

Doctorat de l'Université de Toulouse

délivré en co-tutelle avec University Stefan cel Mare

préparé à l'Université Toulouse III - Paul Sabatier

Contributions au développement des dispositifs électroniques basés sur des molécules à transition de spin

---

Thèse présentée et soutenue, le 16 décembre 2024 par

Ion SOROCEANU

École doctorale
SDM - SCIENCES DE LA MATIERE - Toulouse

Spécialité
Physique

Unité de recherche
LCC - Laboratoire de Chimie de Coordination

Thèse dirigée par
Gabor MOLNAR et Adrian GRAUR

Composition du jury
M. Olivier EICHWALD, Président, Université Toulouse III - Paul Sabatier
M. Jean-François LETARD, Rapporteur, CNRS Aquitaine
M. Gheorghe BREZEANU, Rapporteur, University Politehnica
Mme Doina RADUCANU, Examinatrice, University Politehnica
M. Gabor MOLNAR, Directeur de thèse, CNRS Occitanie Ouest
M. Adrian GRAUR, Co-directeur de thèse, tefan cel Mare University

Membres invités
M. Azzedine BOUSSEKSOU, CNRS Occitanie Ouest
M. Aurelian ROTARU, tefan cel Mare University

Contents

List of figures ---------- 5
List of abbreviations ---------- 12
GENERAL INTRODUCTION ---------- 13
References ---------- 14
Chapter 1. Literature Review of Hybrid Materials and Systems Combining Spin Crossover Complexes and Electroactive Compounds ---------- 16
1.1. Introduction to the spin crossover phenomenon ---------- 16
1.1.1. Thermally Induced Spin State Change ---------- 18
1.1.2. Pressure-Induced Spin Crossover ---------- 19
1.1.3. Light-Induced Spin State Change ---------- 20
1.1.4. Properties changes of the spin crossover materials and associated detection methods ---------- 21
1.1.5. Electrical properties of spin crossover materials ---------- 22
1.2.Coupling SCO compounds with 2D materials for synergistic electrical properties ----- 23
1.3.Coupling SCO compounds with metallic nanoparticles ---------- 29
1.4. Coupling SCO compounds with electroactive polymers and polymer composites ----- 31
1.4.1.Freestanding spin crossover/polymer multilayers ---------- 31
1.4.2. Spin crossover/polymer multilayers on rigid substrates ---------- 33
1.4.3. Spin-crossover@polymer composites displaying electromechanical couplings --- 36
1.5. Conclusions and outlook ---------- 37
References ---------- 38
Chapter 2. Investigation of the effect of ferroelectric polarization on the spin state of spin crossover complexes embedded in a piezopolymer matrix ---------- 44
2.1. Introduction ---------- 44
2.2. Sample preparation ---------- 47
2.3. Analysis of poling effect on the SCO behavior in composites ---------- 47
2.4. Analysis of poling effect on the SCO behavior in films deposited on a ferroelectric substrate ---------- 53
2.5. Conclusions ---------- 56
References ---------- 56
Chapter 3. Electrospinning of spin crossover polymer nanofibers ---------- 59
3.1. Introduction ---------- 59
3.2. Electrospinning fabrication method ---------- 61
3.3.Fabrication and characterization of SCO@PVP nanofibers ---------- 62
3.4.Fabrication and characterization of SCO@P(VDF-TrFE) nanofibers ---------- 64

3.5. Conclusions---------- 73
References ---------- 74
Chapter 4. Thermal Energy Harvesting Using a Hybrid Pyroelectric - Spin Crossover System ---------- 77
4.1. Introduction---------- 77
4.2. Device fabrication and characterization ---------- 80
4.3. Harvesting experiments---------- 87
4.4. Discussion ---------- 91
References ---------- 93
Chapter 5. Novel Approaches for Electrical Sensing of Molecular Spin State Switching in Spin Crossover Materials ---------- 95
5.1. Spin transition sensing in percolation devices---------- 95
5.1.1. Introduction to percolation based strain sensors ---------- 95
5.1.2. Percolation device fabrication ---------- 95
5.1.3. Results and discussion of percolation device properties ---------- 98
5.2. Spin crossover detection with the tunnel diode oscillator (TDO) technique---------- 102
5.2.1. Introduction to the tunnel diode oscillator (TDO) technique---------- 102
5.2.2. Construction and characterization of SCO/PVP thin film based capacitors ------ 103
5.2.3. Dielectric properties of SCO this films using a tunnel diode oscillator technique 105
5.2.4. Results and discussion of TDO measured capacitive devices---------- 109
5.3. Magnetic measurements of spin crossover composites. ---------- 111
5.4. Conclusions---------- 114
References ---------- 115
GENERAL CONCLUSIONS AND PERSPECTIVES ---------- 117

List of figures

***Figure 1.1**. Electronic configurations of the two possible ground states for an iron(II) ion in an octahedral complex.*

***Figure 1.2.** Adiabatic potentials for the HS and LS states of an octahedral Fe(II) complex as a function of the metal-ligand bond length.*

***Figure 1.3.** Different types of spin transition behaviors: (a) gradual, (b) abrupt, (c) hysteresis, (d) two-step, and (e) incomplete spin transitions. From [3]*

***Figure 1.4.** Schematic representation of the pressure effect on LS and HS potential wells of Fe(II) SCO compounds.*

***Figure 1.5.** Conductivity of the SCO complex $[Fe(Htrz)_2(trz)](BF_4)$ in thermal cycles at constant pressures of 1 bar, 1 kbar and 2 kbar*

Figure 1.6. *Simplified Jablonski diagram showing the LIESST and reverse LIESST effects.*

Figure 1.7. *Color change in the $Fe(ptz)_{62}$ SCO compound from dark purple (LS state) at liquid nitrogen temperature to white (HS state) at room temperature.*

Figure 1.9. *Magnetic susceptibility and electrical resistivity of the SCO compound $[Fe(dppTTF)_2][Ni(mnt)_2]_2(BF_4)\cdot PhCN$ at variable temperature.*

Figure 1.10. *(a) Schematic representation of the device based on graphene covered with a layer of particulate SCO film.(b) Top view image of the device.(c-d) Sheet resistance of the graphene/SCO device as a function of (c) the gate voltage (at selected temperatures) and (d) the temperature (at selected gate voltages).*

Figure 1.11.*(a) Schematic view of the epoxy (green)/SCO single crystal (red)/PMMA (blue)/graphene (black)/PMMA device.(b) Device resistance measured in 4 cycles (indicated I–IV) in the cooling regime and the HS fraction (black) of the bulk sample.*

Figure 1.12.*(a) Temperature dependent (red/blue lines) and photo-thermally induced conductivity change (green arrow) in an SCO/graphene bilayer device. Reprinted with permission from ref. [24].(b) Temperature dependence of conductance of a SCO/graphene device displaying both light induced (green arrow) and thermal (red/blue lines) spin transition.*

Figure 1.13. *Temperature dependence of the resistivity for SCO-graphene and SCO-$NbSe_2$ devices with different configurations. The insets show the scheme of the devices. (The SCO, FLG, h-BN, and $NbSe_2$ layers are represented in yellow, purple, bright-blue, and green colors, respectively.)*

Figure 1.14.*(a) Chemical structure of the SCO molecules encapsulated in carbon nanotubes.(b) Schematic representation of SCO molecules inside a carbon nanotube.(c) SEM image depicting a SCO@SWCNT hybrid material connecting metallic electrodes. The scale bar is 500 nm.(d) Current versus temperature curve recorded for a SCO@SWCNT hybrid upon heating and cooling.*

Figure 1.15.*(a) SEM micrograph and schematic representation of a SCO molecules-gold nanoparticle array device. Reproduced with permission from ref. [37].(b) TEM image and (c) structural model of the self-assembly made of Pt nanoparticles and chain-like SCO coordination polymers.*

Figure 1.16.*a-d) Scheme and SEM images of the interdigitated electrode device connected by densely packed Au@SCO core-shell particles.e) I–V curves in the high-conductivity (purple) and low-conductivity (orange) states associated to the LS and HS forms, respectively.Inset: Thermal variation of the electrical current in the heating and cooling modes.*

Figure 1.17.*(a) Scheme of a U-shaped bilayer SCO@polymer/Ag@polymer device actuated electrothermally and controlled in closed-loop using an external position sensor.(b) Photographs of a device lifting a payload.(c) Closed-loop test of the positioning accuracy of a device operated during two weeks over 35,000 endurance cycles.*

Figure 1.18.*(a) Scheme and (b) photograph of the bilayer SCO@PC/constantan@PI heterostructure(c) The change in resistance at the SCO.*

Figure 1.19.*(a) Scheme of the SCO/ferroelectric bilayer and the influence of the ferroelectric polarization direction on the molecular spin states.(b) X-ray absorption measurement of the ratio of LS and HS molecules in the film depending on the polarization direction in the underlying piezopolymer substrate.(c) Scheme of an interdigitated electrode device with an SCO film and current vs. voltage curves recorded at 150 K and 298 K.(d) Scheme of the ferroelectric/SCO bilayer on the interdigitated electrodes and current vs. voltage curves in the two polarization directions (isothermal).*

Figure 1.20.*(a) Scheme of the cross-section of the SCO-OFET device.(b) SEM image of the device cross-section.(c) Temperature dependent charge transport in the transistor ON state (gate voltage: -10 V). For comparison, the UV absorbance change at 350 nm of the SCO@PVP-P3HT bilayer film is also shown.(d) Drain-source current during ten successive thermal cycles for an SCO-OFET device.*

Figure 1.21.*Electrical conductivity as a function of the temperature measured in $[Fe(trz)(Htrz)_2][BF_4]$@PPY (left) and $\{[Fe(trz\text{-}NH_2)_3][BF_4]_2\}$@PPY (right) composite materials.*

Figure 2.1.*Real part of the dielectric permittivity of 1 as a function of the frequency, measured at selected temperatures in the heating mode. The inset shows the thermal hysteresis loop of ε' recorded at 1 kHz $Fe(Htrz)_2(trz)$.*

Figure 2.2.*a) Simulated temperature dependence of the HS fraction in the absence and presence of an electric field. The field-induced shift of the spin transition is indicated by the arrow.*
b) Electric field switch experiment performed at 82 °C. The left panel shows the current recorded when cooling the device from 130 to 82 °C under 10 kV/cm. The middle panel depicts the temporal evolution of the current at fixed temperature (82 °C) and bias (40 kV/cm) followed by a complete thermal cycle (right panel) between 82 and 130 °C [16].

Figure 2.3.*a) Scheme of a bilayer SCO/PVDF-HFP device with I-V curves in the two spin states.b) The effect of the polarization direction on the HS fraction of the SCO layer [18].*

Figure 2.4.*Electrical properties of the P(VDF-TrFE)/SCO composite. Short-circuit current under zero applied bias on heating and cooling at rates of ±2 K min⁻¹. Measurements were done after poling the sample in a 13.6 MV m⁻¹ electrical field. The inset shows the modulation of the amplitude and temperature of the discharge current peak (cooling mode) controlled by the initial polarization [22].*

Figure 2.5.*The schematic representation of blade casting (left) and hot pressing (right) techniques.*

Figure 2.6.*Photographs of the neat P(VDF$_{80}$-TrFE$_{20}$) film (from left to right): blade-casted, annealed at 120 °C, and hot pressed.*

Figure 2.7.*(a-b) Selected room temperature optical images of the composites (a) 1@PVP and (b) 2@PVP with different concentrations of SCO particles (5 wt.% and 2 wt.%).
(c-d) Variable temperature optical reflectivity (normalized to the highest temperature) of the composites (c) 1@PVP and (d) 2@PVP integrated for the poled (black) and non-poled (red) regions, as well as for the entire image (green).*

Figure 2.8.*DSC measurements on sample 1Apoled through multiple thermal cycles, with identical starting temperatures (20 °C) and increasing end temperatures (from 100 to 160 °C).*

Figure 2.9.*Spin transition temperatures in the heating (a) and cooling (b) modes as well as the associated width of the hysteresis (c) as a function of the 'highest heating temperature' for samples 1Apoled (black), 1Anon-poled (red), 1Bpoled (green), and 1Bnon-poled (blue).*

Figure 2.10.*Spin transition temperatures in the heating (a) and cooling (b) modes as well as the associated width of the hysteresis (c) as a function of the 'highest heating temperature' for the neat powder sample 1. Two series of experiments are shown: a first experiment (in red) and a second experiment (in green) conducted on the same DSC sample pan following one month storage in ambient air.*

Figure 3.1.*SEM images of SCO@PS composite nanofibers with 5 and 13.5% load [10].*

Figure 3.2. *Schematic representation of the coaxial electrospinning process and SEM image of the coaxial spun SCO@PMMA (25 wt.%) composite nanofibers [12].*

Figure 3.3.*Schematic representation of the electrospinning process and photograph of the Spinbox instrument.*

Figure 3.4. *Representative SEM images for the composite nanofibers 1@PVP (left panel) and 2@PVP (right panel) with different concentrations of SCO particles (5 wt.% and 2 wt.%).*

Figure 3.5.*Temperature dependence of the normalized magnetic moment, recorded for the SCO complex 1 (left panel) and 2 (right panel), compared with the magnetic properties of the composite fibers 1@PVP and 2@PVP with different filler concentrations.*

Figure 3.6.*Representative SEM images for the composite nanofibers 3@P(VDF-TrFE) with 10 wt.% (left) and 25 wt.% (right) particle concentration.*

Figure 3.7. *Temperature dependence of the normalized magnetic moment, recorded for the pure SCO complex 3 and for the composite fibers 3@P(VDF-TrFE) with two different filler concentrations.*

Figure 3.8.*Left panel: Scheme of the impedance spectroscopy measurement showing also the variation of the applied electrical field and the induced polarization of the sample. Right panel: Photograph of the broadband dielectric spectrometer.*

Figure 3.9.*Photographs of the blade-casted (left) and electrospun (right) samples of 3@P(VDF-TrFE).*

Figure 3.10.*Top panel: Real part of the complex conductivity (at 10 kHz) as a function of the temperature for nanofibers of the pure complex 3, the pure P(VDF-TrFE) fibers, and 3@P(VDF-TrFE) composite fibers with 10 and 25 wt.% particle load.*
Bottom panel: The same data for the pure complex 3, the nanocomposite fibers (25% SCO), and the blade-casted composite film (25% SCO).

Figure 3.11.*Left panel: Schematic representation of the real part (solid line) and imaginary part (dashed line) of the dielectric permittivity over the frequency spectrum.*
Middle and right panels: Cole-Cole plots simulated for various values of the shape parameters β and γ, respectively.

Figure 3.12.*Imaginary part of the permittivity as a function of the frequency of the applied electrical field at different temperatures for the neat P(VDF-TrFE) fibers (left) and the pure SCO complex 3 (right).*

Figure 3.13. *Havriliak-Negami fit of the imaginary part of permittivity of the 10% SCO@P(VDF-TrFE) nanofiber composite (left) and of the pure SCO material (right) recorded at 20 °C. A good global fit of the experimental data could be obtained in both cases using 3 HN components.*

Figure 3.14. *Havriliak-Negami fit of the imaginary part of permittivity of the 10% SCO@P(VDF-TrFE) nanofiber composite acquired at 77 °C in the heating mode, LS state, (left) and in the cooling mode, HS state, (right).*

Figure 3.15. *Temperature dependence of the dielectric strength (left) and the relaxation time (right) associated with the conductivity relaxation phenomenon acquired for the pure SCO powder and for the 10% SCO@P(VDF-TrFE) nanofiber composite during a complete heating-cooling cycle. The left-hand y-axis in black (resp. right-hand in red) refers to the pure SCO material (resp. the composite fibers).*

Figure 4.1. *Interrelationship between piezoelectric, pyroelectric, ferroelectric, and dielectric materials.*

Figure 4.2.*a) Short-circuit current (at 0 V) upon thermal cycling of a SCO@P(VDF70-TrFE30) composite showing discharge peaks at the spin transition.*
b) CTE of the same composite as a function of the temperature showing thermal expansion peaks at the spin transition [4].

Figure 4.3. *From left to right: Photograph of an SMA/P(VDF-TrFE) multilayer cantilever device and its output voltage under finger tapping as well as thermal loading [7].*

Figure 4.4.*Conceptual representation of the asymmetrical (left) and symmetrical (right) cantilever designs. Colour code: SCO composite (pink), Ag composite (dark grey), and pure P(VDF-TrFE) (light grey).*

Figure 4.5. *Representative SEM image of the SCO particles $Fe\{(Htrz)_{1.8}(trz)\}_1(NH_2\text{-}trz)_{0.21}\cdot 0.7H_2O$, characterized by ca. 1 μm length and an aspect ratio of ca. 30.*

Figure 4.6. *Calorimetric measurement on the $Fe\{(Htrz)_{1.8}(trz)\}_1(NH_2\text{-}trz)_{0.21}\cdot 0.7H_2O$@$P(VDF_{80}\text{-}TrFE_{20})$ composite (25 vol%). The SCO and Curie transitions occur on heating at ca. 85 °C and 136 °C, respectively. The third peak is associated with the melting of the polymer near 150 °C.*

Figure 4.7. *Left: SEM image of the silver particles used.Right: Electrical resistivity as a function of the thicknesses of the Ag@P(VDF-TrFE) film for three different concentrations of silver particles (per weight). The resistivity should be independent of the film thickness, but below a critical thickness it shows a strong dependence (blue ellipse region).*

Figure 4.8. *Photographs of the last stages of the device fabrication.Left: The three casted layers after drying.Middle-left: Multilayer stack after hot pressing.Middle-right: Film polarization.Right: The cantilever device with the connected electrodes for harvesting measurement.*

Figure 4.9.*SEM images of a 4-layer (asymmetrical) cantilever device cross-section clearly revealing a ca. 52 μm thick SCO@P(VDF-TrFE) layer and a ca. 77 μm thick P(VDF-TrFE) layer, the latter being sandwiched between two, ca. 6-10 μm thick, Ag@P(VDF-TrFE) layers (top). The EDX image of an asymmetrical cantilever that shows the distribution of the materials in the layers (bottom).*

Figure 4.10.*Storage modulus measured in heating and cooling modes (3 K/min, 1 Hz, amplitude 20 μm, constant 1.5:1 ratio of static force and dynamical force amplitude) for a hot pressed layer of the pure P(VDF-TrFE) film (top, left), a 66 wt.% Ag@P(VDF-TrFE) composite film (top, middle), and a 25 wt% SCO@P(VDF-TrFE) composite film (top right). For the SCO composite the loss tangent, strain, and coefficient of thermal expansion (CTE) are also shown as a function of the temperature.*

Figure 4.11.*Schematic images showing the piezoelectric modes 33 (both electric voltage and mechanical force are normal to the film surface) and 31 (V is out-of-plane, but F is in-plane, along the beam axis). In this two-subscript notation, we identify length (1), width (2), and thickness (3). The first number indicates the electrical poling axis, which is usually the thickness (3) direction, whereas the second number denotes the axis of mechanical stress.*

Figure 4.12.*Piezo current generated by finger pressing the cantilever. The green arrows indicate the two finger pressing events.*

Figure 4.13.*Top left: Measurement setup with the heated oil bath.*
Top right: Microscope image of the symmetrical cantilever in the oil bath.
Bottom panel: Microscope images of the asymmetrical cantilever at different temperatures (in the heating mode). From left to right: 30 °C, 70 °C, and 110 °C.

Figure 4.14.*Short-circuit current (U = 0 V) acquired upon thermal cycling a 5 layers symmetrical (SCO/Ag/PE/Ag/SCO) device at rates of 5 °C/min (blue) and 3 °C/min (orange). Prior to the measurements the piezoelectric (PE) layer was poled to reach a d_{33} of -15 pC/N. The green curve shows the simultaneously recorded optical reflectivity of the device.*

Figure 4.15.*Short-circuit current (U = 0 V) acquired upon two successive thermal cycles for a 5 layers symmetrical (SCO/Ag/PE/Ag/SCO) device. Prior to the measurements the piezoelectric (PE) layer was poled to reach a d_{33} of -15 pC/N.*

Figure 4.16.*Short-circuit current (U = 0 V) acquired upon three successive thermal cycles for a 4 layers asymmetrical (SCO/Ag/PE/Ag) device. Prior to the measurements the piezoelectric (PE) layer was poled to reach a d_{33} of -20 pC/N.*

Figure 4.17.*Schematic axial stress and strain distribution across the height for a bending bilayer beam.*

Figure 5.1.*The sandwich-like device used for the study of SCO transition impact on electrical resistance. The gray (purple) layer represents Ag (SCO) composites.*

Figure 5.2.*SEM image of a percolation device containing a 60% silver composite (a), and the corresponding Energy-Dispersive X-ray (EDX) spectroscopy image of the same cantilever (b) showing the distribution of silver (Ag) in the middle layer (depicted in navy) and iron (Fe) from the Spin Crossover (SCO) composite layers (shown in green).*

Figure 5.3.*The percolation device in the measurement setup in LS (left) and HS (right) states.*

Figure 5.4.*The measured values of the resistances for the percolation devices.*

Figure 5.5.*The value of the resistances of the devices after the subtraction of thermal coefficient of resistance effect.*

Figure 5.6.*The relative change in resistance of the percolation device between the LS and HS state, for the 80 °C temperature value state inside the hysteresis loop.*

Figure 5.7.*The SEM image of the samples associated with 150 μm blade height fabrication of:a) 55% silver concentration, b) 60% silver concentration, c) 65% silver concentration, d) 65% silver concentration in a region of weak contact.*

Figure 5.8.*The average thicknesses of the silver layer as a function of casting blade height of the percolation devices as extracted from SEM imaging.*

Figure 5.9.*Photograph of a double ITO-type capacitor with SCO+PVP (left) and an image of the thin high concentration SCO to PVP layer (right) obtained using spin coating.*

Figure 5.10.*Capacitance (left) and Impedance (right) vs. temperature for a double ITO-type capacitor with SCO+PVP, from impedance measurement at different excitation frequencies.*

Figure 5.11.*Transmittance (left) and Reflectivity (right) vs. temperature for a double ITO-type capacitor with SCO+PVP.*

Figure 5.12.*Reflectivity spectrum and relative count value at 550 nm vs. temperature for a double ITO-type capacitor with SCO+PVP, from reflectivity and spectrometry measurements.*

Figure 5.13.*Fabrication process of ITO glass SCO+PVP based capacitor.*

Figure 5.14.*(a) ITO Glass SCO+PVP intermix based dielectric capacitor;(b) Frequency dependent Capacity and Impedance values of the capacitor at RT as measured using broadband dielectric spectroscopy;(c) 50x optical image of the SCO+PVP intermix dielectric;(d) SEM image of $Fe[(Htrz)_2(trz)]BF_4$ particles used.*

Figure 5.15.*TDO circuit design used for temperature measurements.*

Figure 5.16.*(a) High-spin fraction (nHS) as a function of temperature for the SCO-PVP composite, measured using an MPMS3 SQUID magnetometer;*
(b) TDO frequency relative shift as a function of temperature for both the PVP only and SCO+PVP dielectric capacitor at ~ 0.9 MHz.

Figure 5.17.*Capacity variation with temperature "δC_T" of $Fe(Htrz)_2(Trz)$ particles in PVP dielectric ITO glass capacitor (in pF) as extracted from TDO frequency measurements, for lower frequencies (left) and higher frequencies (right).*

Figure 5.18.*Dielectric permittivity of $Fe(Htrz)_2(Trz)$ particles in PVP matrix, for lower measured TDO frequencies (left) and higher measured TDO frequencies (right).*

Figure 5.19.*Capacity shift from RT value as a function of TDO resonant frequency for 6 temperature values in:(left) heating mode;(right) cooling mode.*

Figure 5.20.*The images of coils used for magnetic measurements with Impedance spectroscopy.*

Figure 5.21.*The temperature values of the measured inductance of the coil with SCO in temperature (a). The integral of the inductance that reveals the spin transition hysteresis.*

Figure 5.22.*The image of the coil used in magnetic measurements under pressure covered in epoxy with spin crossover particles.*

Figure 5.23.*The temperature values of inductance measured for a flat spiral coil with spin crossover particles under pressure.*

Figure 5.24.*The temperature values of TDO frequency measured for a coil containing spin crossover particles (left) and the integral (right) showing the SCO hysteresis.*

List of abbreviations

AC – Alternating Current
AcS-BPP – S-(4-{[2,6-(Dipyrazol-1-yl)pyrid-4-yl]ethynyl}-phenyl)ethanethioate
AuNP – Gold Nanoparticles
CVD – Chemical Vapor Deposition
CNTs – Carbon Nanotubes
CTE – Coefficient of Thermal Expansion
d_{33}, d_{31} – Piezoelectric Charge Coefficients
DSC – Differential Scanning Calorimetry
DMA – Dynamical Mechanical Analysis
EDX – Energy-Dispersive X-ray
FE-SEM – Field Emission Scanning Electron Microscopy
FLG – Few Layer Graphene
h-BN – Hexagonal Boron Nitride
HS – High Spin
ITO – Indium Tin Oxide
LC – Inductor-Capacitor
LC tank – Inductor-Capacitor Tank
LED – Light Emitting Diode
LIESST – Light-Induced Excited Spin State Trapping
MEK – Methyl Ethyl Ketone
MPMS – Magnetics Property Measurement System
MPMS3 – Magnetics Property Measurement System
NP0 – A Type of Dielectric Capacitor with Zero Temperature Coefficient
OFET – Organic Field-Effect Transistor
PL – Photoluminescence
PMMA – Poly(methyl methacrylate)
PMNPT – $[Pb(Mg_{1/3}Nb_{2/3})O_3]_{0.68}[PbTiO_3]_{0.32}$
PANI – Polyaniline-Sulfate
P3HT – Poly(3-hexylthiophene)
PC – Polycarbonate
PEDOT-PT – Poly(3,4–ethylenedioxythiophene)-paratoluenesulfonate
PEDOT-PSS – Poly(3,4-ethylenedioxythiophene)-poly(styrenesulfonate)
PE – Piezoelectric
PFM – Piezo-Force Microscopy
PI – Polyimide
PID – Proportional-Integral-Derivative
Pt – Platinum
PVP – Polyvinylpyrrolidone
P(VDF-TrFE) – *Poly(vinylidene fluoride-co-trifluoroethylene)*
PPY – Polypyrrole
RF – Radio-Frequency
SMA – Shape Memory Alloy
SEM – Scanning Electron Microscopy
SOXIESST – Soft X-ray Induced Excited Spin State Trapping
SWCNT – Single-Walled Carbon Nanotubes
TDO – Tunnel Diode Oscillator
UV – Ultraviolet
XAS – X-ray Absorption Spectroscopy

GENERAL INTRODUCTION

This thesis recounts the work dedicated to the conception, fabrication and characterization of hybrid materials and systems combining spin crossover (SCO) complexes and electroactive materials.

Molecule-based SCO complexes of $3d^4$-$3d^7$ transition metal ions display a bistability between their high spin (HS) and low spin (LS) forms, which is accompanied by a spectacular change of their physical properties (optical, electrical, mechanical, caloric and magnetic) [1]. These unique properties provide an appealing perspective for using SCO compounds in a variety of technological applications, including information processing devices, sensors, actuators and heat management devices [2]. To construct useful devices, it appears often necessary to use electric fields or currents to sense and to actuate the spin state changes. However, due to the highly insulating nature and relatively feeble electrical response of bulk SCO materials, it is usually not possible to achieve electrical sensing or actuation using just the neat SCO compound [3].

To render SCO compounds "electroactive", researchers proposed two main strategies. In a first approach, the chemical synthesis of novel SCO complexes incorporating electroactive (most often conducting) molecular bricks has been proposed [4]. However, it is extremely difficult to optimize at the same time both the electrical and SCO properties of a given compound. In a second approach, SCO complexes were combined with various electroactive materials (e.g. graphene [5], metallic nanoparticles [6] and electroactive polymers [7]) into composite materials and other hybrid systems. For both strategies, the common objective is to establish synergy between the SCO bistability and the electrical properties of the 'partner' material. These hybrids can then be used to either detect the SCO phenomenon by electrical means (sensing), or, the other way around, to modulate the electrical output of the device through the SCO phenomenon (actuation). Beyond these primary aims, researchers also explore other couplings between SCO and electroactive materials to develop unprecedented properties and thus create novel opportunities for the applications of SCO materials, for example in energy harvesting technologies [8].

To contribute to the development of novel synergies and applications using a combination of SCO and electroactive materials, the present thesis proposes a series of original experimental approaches, which are discussed over five chapters:

In a first chapter, we briefly introduce the spin crossover phenomenon, followed by an exhaustive literature overview of the characteristics of hybrid materials and devices, including graphene, metallic nanoparticles and electroactive polymers, combined with SCO complexes, while also addressing the challenges and future perspectives of this field.

The second chapter focuses on the fabrication and properties of composite materials that incorporate SCO nanoparticles within a ferroelectric polymer matrix poly(vinylidene fluoride-co-trifluoroethylene), P(VDF-TrFE). The chapter begins with a brief overview of the appealing but controversial topic of the effect of intense electric fields on the SCO phenomenon. Then, we describe the composite fabrication process, based on blade casting and hot pressing, and the characterization methods, which are then used to evaluate the effect of electrical poling of the

matrix on the SCO properties of the embedded particles. Additionally, the chapter explores the same question for the case of SCO films deposited on top of P(VDF-TrFE) substrates.

Chapter 3 is devoted to the manufacturing of SCO@P(VDF-TrFE) polymer composites using the electrospinning method. It also includes work on electrospun SCO@PVP (polyvinylpyrrolidone) nanofiber composites. In both cases, the sample morphologies are studied by SEM and the SCO properties by magnetometry. The P(VDF-TrFE) based composites are then further investigated by means of broadband dielectric spectroscopy in the frame of the Havriliak-Negami formalism, which allow for detailed discussions of the different mechanisms that contribute to the overall dielectric response of the material as well as the interplay between the SCO phenomenon and the dielectric properties.

In Chapter 4 we describe the fabrication and characterization of a series of devices aimed at thermal energy harvesting. The multilayer devices consist of a pyro/piezoelectric film, combined with one (or two) SCO@P(VDF-TrFE) composite film(s) and two Ag@P(VDF-TrFE) layers. Capitalizing on the SCO actuation, the devices provide two current outputs under thermal load: one due to the ordinary pyroelectric effect and another due to the piezoelectric effect brought into by the SCO thermal strain. We show that by adjusting the sign of the piezoelectric effect it is possible to obtain a harvester output, which effectively sums up these two contributions.

In the 5TH and last chapter, we propose two novel approaches for the electrical sensing of the spin state switching in SCO@polymer composites. The first approach uses a strain sensor, made of Ag@P(VDF-TrFE), which is attached to the SCO@polymer layer, which works on the basis of percolation effects. In addition, we show how one can study the dielectric permittivity of spin crossover molecular materials using a radio-frequency (RF) resonant tunnel diode oscillator (TDO) circuit.

The thesis ends with the general conclusions and perspectives. Literature references are provided at the end of each chapter.

References

[1] Gütlich P., Hauser A., & Spiering H., Thermal and Optical Switching of Iron(II) Complexes, Angew. Chem. Int. Ed. 33.20 (1994) 2024-2054.

[2] G. Molnár, S. Rat, L. Salmon, W. Nicolazzi, A. Bousseksou, Spin Crossover Nanomaterials: From Fundamental Concepts to Devices, Adv. Mater., 2018, 30, 1703862.

[3] C. Lefter, et al. "Charge transport and electrical properties of spin crossover materials: towards nanoelectronic and spintronic devices." Magnetochemistry 2.1 (2016): 18.

[4] M. Wang, Z. Y. Li, R. Ishikawa, M. Yamashita, Spin crossover and valence tautomerism conductors, Coord. Chem. Rev., 2021, 435, 213819

[5] J. Dugay, M. Aarts, M. Giménez-Marqués, T. Kozlova, H.W. Zandbergen, E. Coronado, H.S.J. van der Zant, Phase Transitions in Spin-Crossover Thin Films Probed by Graphene Transport Measurements, Nano Letters, 2017, 17, 186.

[6] Devid, E. J., Martinho, P. N., Kamalakar, M. V., Salitros, I., Prendergast, U., Dayen, J. F., ... & van der Molen, S. J. (2015). Spin transition in arrays of gold nanoparticles and spin crossover molecules. ACS Nano 9, 4496–4507.

[7] Y.-S. Koo, J.R. Galán-Mascarós, Spin Crossover Probes Confer Multistability to Organic Conducting Polymers, Advanced Materials, 2014, 26, 6785.

[8] S. Rat, M. Piedrahita-Bello, L. Salmon, G. Molnar, P. Demont, A. Bousseksou, Coupling Mechanical and Electrical Properties in Spin Crossover Polymer Composites, Advanced Materials, 30 (2018) 1705275.

Chapter 1. Literature Review of Hybrid Materials and Systems Combining Spin Crossover Complexes and Electroactive Compounds

In this chapter, following a brief general introduction to the molecular spin crossover phenomenon, we review different strategies explored towards coupling molecular spin crossover complexes with electroactive materials within hybrid systems. These include composites, core-shell and multilayer structures made with atomically flat, 2D materials (e.g. graphene), metallic nanoparticle arrays and electroactive polymers. The global objective of these different approaches is common: one seeks to use electric voltage or current to trigger and/or to sense the variation of the spin state of the molecules. In some cases, the multifunctionality can be even broader (e.g. electrical, optical, mechanical) and more intricate couplings might occur between the constituents, such as the modification of spin crossover behavior. Importantly, the coupling of materials provides also genuine prospects for energy transduction purposes.

1.1.*Introduction to the spin crossover phenomenon*

Molecular spin crossover (SCO) complexes of certain transition metal ions (Fe^{2+}, Fe^{3+}, Co^{2+}, Co^{3+}, Mn^{2+}, Mn^{3+}, Cr^{2+}) have gained significant attention due to their unique bistable behavior, wherein their physical properties suffer substantial changes upon the spin state switching of the central metal ion between the low spin (LS) and high spin (HS) forms. Since the middle of the past century, numerous studies have explored the SCO behavior in bulk materials (single crystals and microcrystalline powders) and associated changes in the optical, electrical, mechanical, caloric and magnetic properties. In the following we will give a brief account on this spectacular phenomenon, based on the references [1-3].

When the central metal ion is situated in a perfectly octahedral coordination environment, the five d orbitals split into two subsets due to the crystal field effect (Fig. 1.1):

- t_{2g} orbitals: d_{xy}, d_{yz}, d_{xz}

- e_g orbitals: d_{z^2}, $d_{x^2-y^2}$

The orbitals labeled d_{xy}, d_{xz}, and d_{yz} represent orbitals that are oriented in regions away from negative centers of the ligands. Thus, the electrons of the central atom need less energy to occupy these orbitals. The orbitals d_{z^2} and $d_{x^2-y^2}$ are oriented directly toward the negative nodes of the ligands. Due to electrical repulsion, the electrons need more energy to occupy these orbitals.

The energy difference between these two levels is determined by the crystal field strength and depends on the metal-ligand distance. Additionally, electron-electron repulsion, known as the spin pairing energy, must be considered. If the spin pairing energy is larger than the ligand field splitting, electrons can occupy the higher energy e_g orbitals, leading to the paramagnetic high spin (HS) state. Conversely, if the spin pairing energy is smaller, electrons will pair up in the lower energy t_{2g} orbitals, resulting in the diamagnetic low spin (LS) state.

This difference in electron configuration causes a variation in metal-ligand bond lengths, with bonds in the HS state being considerably longer than those in the LS state.

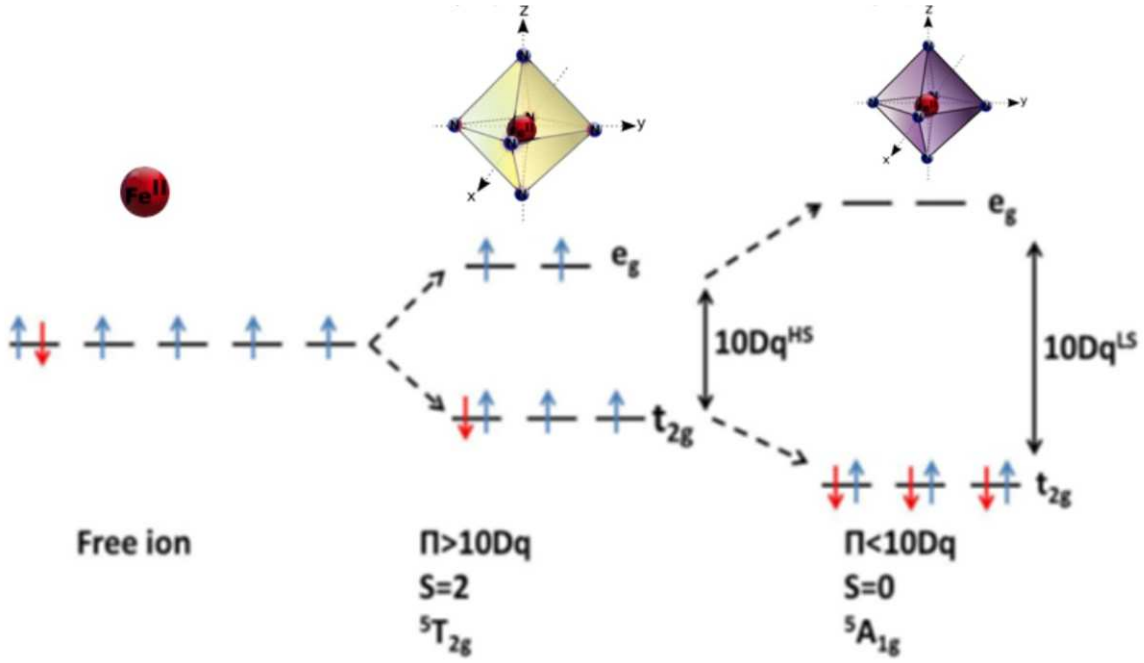

Figure 1.1. *Electronic configurations of the two possible ground states for an iron(II) ion in an octahedral complex.*

The change in crystal field strength (*10Dq*) between the two states is influenced by the metal-ligand distances and can be described by the equation:

$$\frac{10D_q^{LS}}{10D_q^{HS}} = \left(\frac{r_{HS}}{r_{LS}}\right)^n \tag{1.1}$$

where n = 5-6. For the most common, Fe(II)N6 coordination sphere, the metal-ligand distances in the LS and HS states are r_{LS}~2.0 Å and r_{HS}~2.2 Å, respectively. Hence, the ratio of ligand field strengths can be estimated to be approximately 1.75 [3]. In a configurational coordinate diagram (see Fig. 1.2), the minima of the potential wells for the LS and HS states are displaced relative to each other. For a thermal spin transition to occur, the zero-point energy difference between the two states must be comparable to thermal energy.

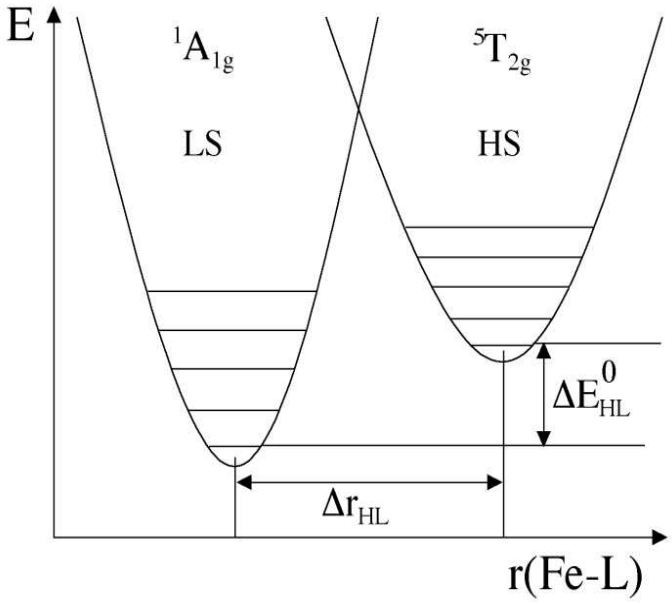

Figure 1.2. *Adiabatic potentials for the HS and LS states of an octahedral Fe(II) complex as a function of the metal-ligand bond length. From [3]*

Considering the dependence of ligand field strength on the metal-ligand bond lengths and the relatively constant spin pairing energy, the ground state energy difference between the HS and LS states can be estimated as a function of their respective ligand field strengths. Three regimes can be observed:

1. *HS ground state*: The HS state is thermodynamically stable at all temperatures under atmospheric pressure.

2. *LS ground state*: The LS state remains stable up to very high temperatures.

3. *Spin crossover region*: Thermal spin crossover may occur in this narrow region where the energy difference between the HS and LS states is small.

1.1.1. Thermally Induced Spin State Change

The spin state can be affected by various stimuli such as temperature changes, pressure, light irradiation, intense magnetic fields, or chemical stimuli. Temperature variation is the most common method to detect spin transitions. The thermally induced spin transition is driven by entropy, with significant portions of the total entropy gain resulting from the change in spin degeneracy between the two states (electronic entropy) and from the change of the vibrational density of states (vibrational entropy). A spin transition curve plotting the high spin fraction versus temperature can reveal various behaviors depending on its shape, as shown in Figure 1.3. The diversity in spin crossover curves primarily arises from the degree of cooperativity between molecules, determined by lattice properties and how metal-ligand deformations propagate through the solid.

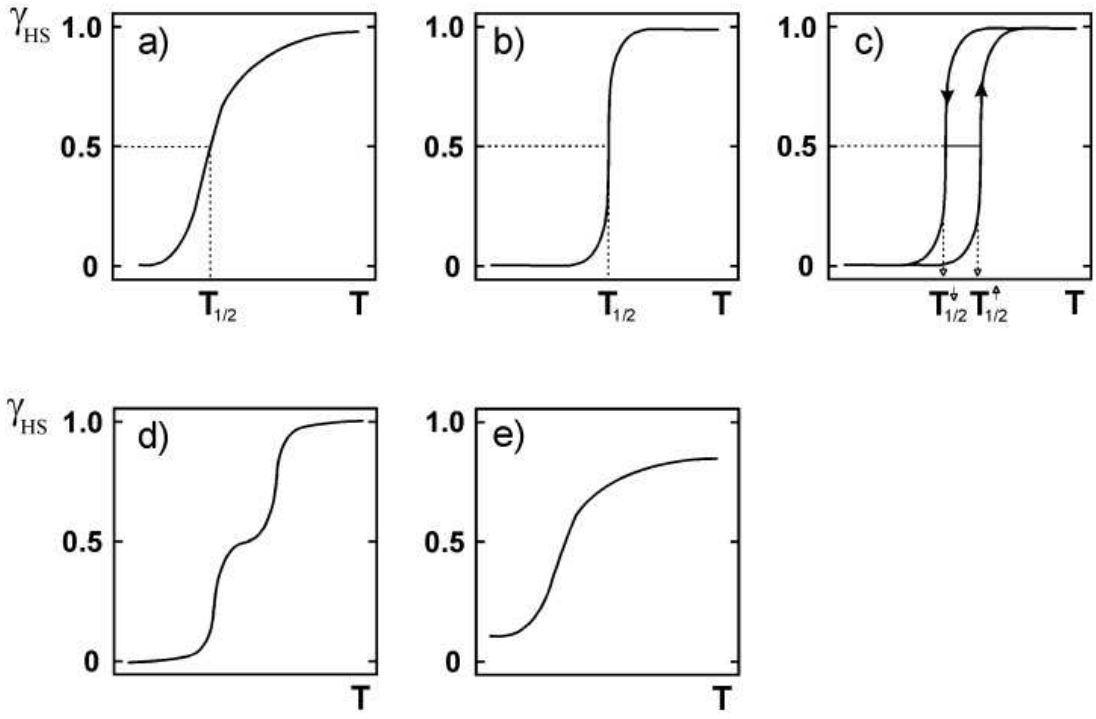

Figure 1.3. *Different types of spin transition behaviors: (a) gradual, (b) abrupt, (c) hysteresis, (d) two-step, and (e) incomplete spin transitions. From [3]*

- *Gradual Transition*: Occurs at the weak cooperative interactions among molecules.

- *Abrupt Transition*: Occurs when there is increased cooperativity.

- *Hysteresis*: High cooperativity leads to hysteretic behavior, where the transition temperatures during heating and cooling are different, resulting in a loop (Figure 1.3c). This can arise from structural phase changes in the lattice or from effective intermolecular interactions.

- *Two-Step Transition*: Observed in materials where metal ions occupy different lattice sites or due to preferential formations of LS-HS pairs (Figure 1.3d).

- *Incomplete Transition*: May be caused by lattice defects or kinetic effects at low temperatures that prevent complete conversion between spin states (Figure 1.3e).

1.1.2. Pressure-Induced Spin Crossover

Applying pressure can trigger or modify the spin transition because the LS state has a smaller molecular volume than the HS state. Pressure favors the LS state by increasing the energy gap between the LS and HS states. This effect can be visualized as a vertical displacement of the potential wells in a configurational diagram (Figure 1.4). For iron(II) SCO compounds, the transition temperature increases by approximately 15–20 K for each kbar of applied pressure (Fig. 1.5).

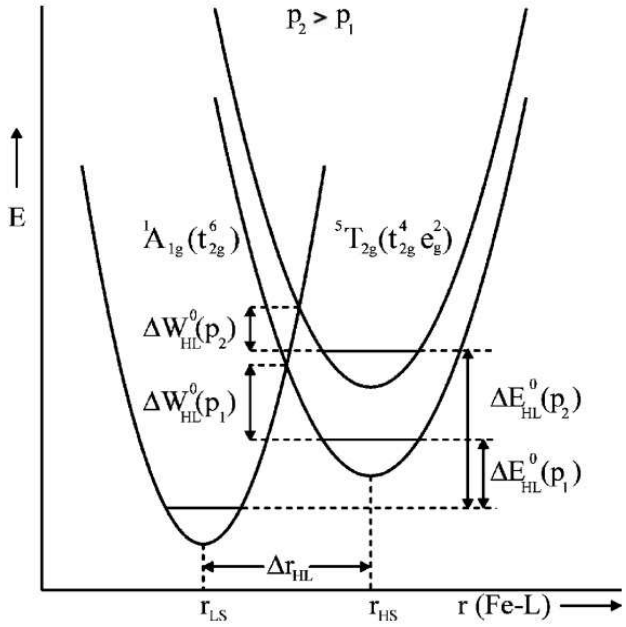

Figure 1.4. *Schematic representation of the pressure effect on LS and HS potential wells of Fe(II) SCO compounds. From [3]*

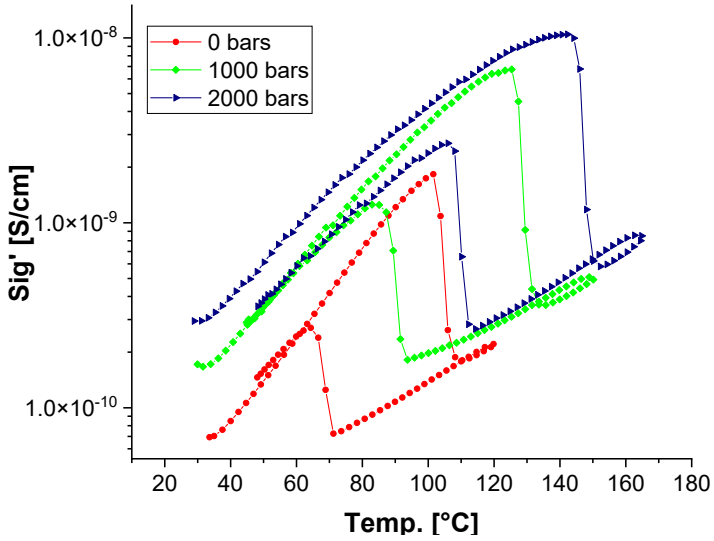

Figure 1.5. *Conductivity of the SCO complex [Fe(Htrz)$_2$(trz)](BF$_4$) in thermal cycles at constant pressures of 1 bar, 1 kbar and 2 kbar.*

1.1.3. Light-Induced Spin State Change

Light can also induce spin state changes By irradiating solid samples with specific wavelengths of light, it is possible to excite the LS state into a metastable HS state with a long lifetime at low temperatures (typically below 50 K), a phenomenon known as "Light-Induced Excited Spin State Trapping" (LIESST). The reverse-LIESST effect involves converting the HS state back to the LS state using light of a different wavelength. This process is illustrated in a Jablonski diagram (Fig. 1.6), which shows the energy levels and transitions involved.

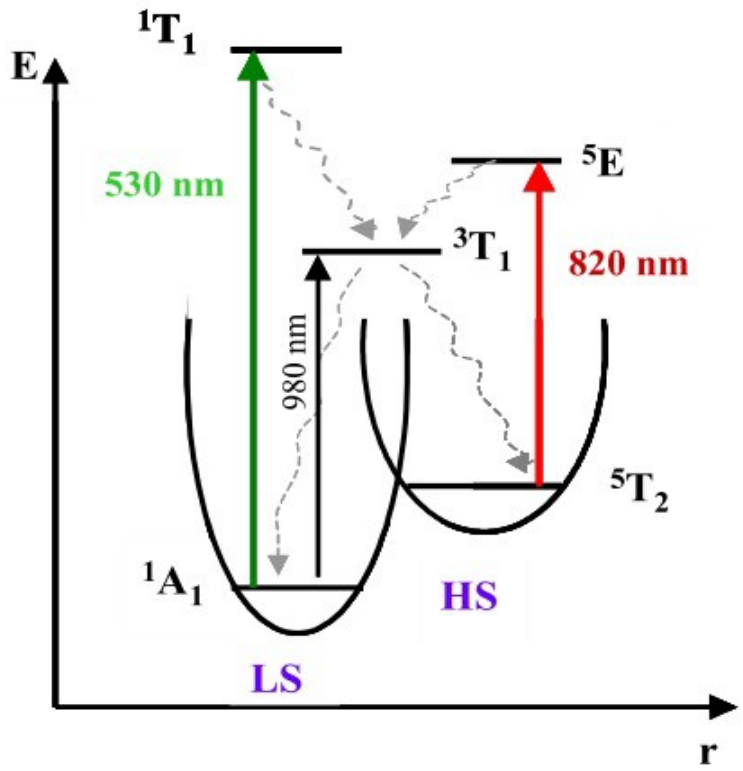

Figure 1.6. *Simplified Jablonski diagram showing the LIESST and reverse LIESST effects. [1]*

1.1.4. Properties changes of the spin crossover materials and associated detection methods

Spin crossover (SCO) materials change their color during the spin transition, making optical detection the most accessible method for identifying the SCO phenomenon. Initially, the transition can be visually observed by altering the temperature of the material (Fig. 1.7). More precise optical detection involves measuring the intensity of light reflected or absorbed by the sample as the temperature changes. This method allows for an inexpensive monitoring of the transition temperature and its characteristics. Magnetic measurements provide a more quantitative method for detecting the spin transition. Since SCO molecules exhibit different magnetic susceptibility in two spin states, these measurements can determine the proportion of molecules in each state, thus mapping the transition and its profile. However, for accurate measurements a calibration of the magnetic curves, using for example Mössbauer spectroscopy, is necessary. Among the most common detection methods we should mention the x-ray diffraction technique (powder or single crystal), which clearly detects the SCO phenomenon through changes of lattice parameters and variations of bond lengths/angles. In our work, we used also calorimetric measurements to detect the spin transition, which measures the enthalpy change associated with the SCO phenomenon.

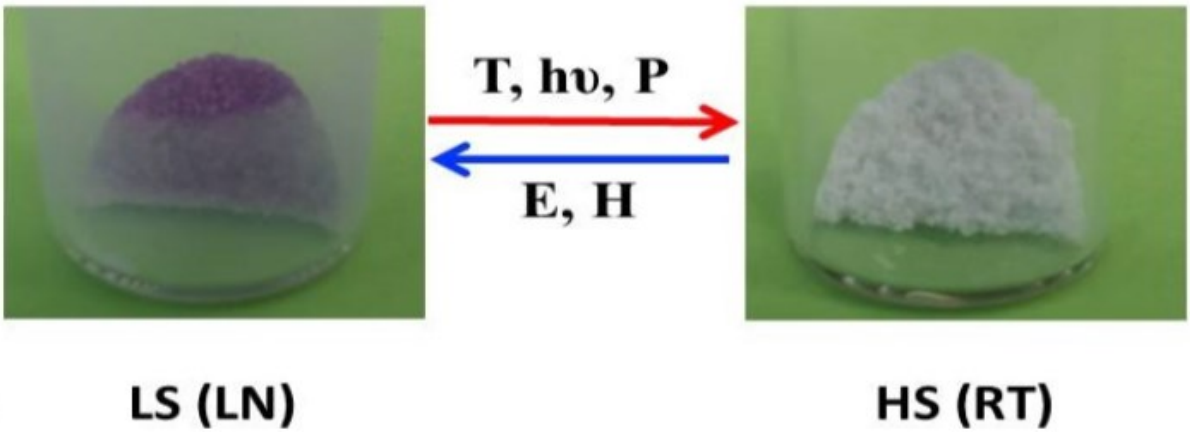

Figure 1.7. *Color change in the $[Fe(ptz)_6](BF_4)_2$ SCO compound from dark purple (LS state) at liquid nitrogen temperature to white (HS state) at room temperature.*

1.1.5. Electrical properties of spin crossover materials

Recently, there have been considerable developments in the field of SCO nanomaterials, including nanoparticles, thin films, nano-patterns and nanocomposites [4]. Based on these advances, several propositions were made to use SCO compounds in different technological applications, such as displays, temperature and gas sensors, barocaloric refrigerators, mechanical actuators and so forth [5-13]. To harness the full potential of these materials in devices, in many cases it appears necessary to use electric voltage and/or current both to sense and to trigger the spin state changes. Considering bulk SCO materials, researchers explored both resistive [14] and capacitive [15] effects. However, it turned out that due to their high electrical resistance it is usually not possible to switch SCO materials directly by Joule heating and it is not an easy task either to detect with finesse the small resistance changes during spin transition. Furthermore, the permittivity changes at the SCO remain modest in most cases (Fig. 1.8), which renders also difficult the use of capacitance measurements to probe the SCO in a device context and practically impossible to switch the spin state by an applied electric field [16]. (The required field strength would be superior to the breakdown field of the material.)

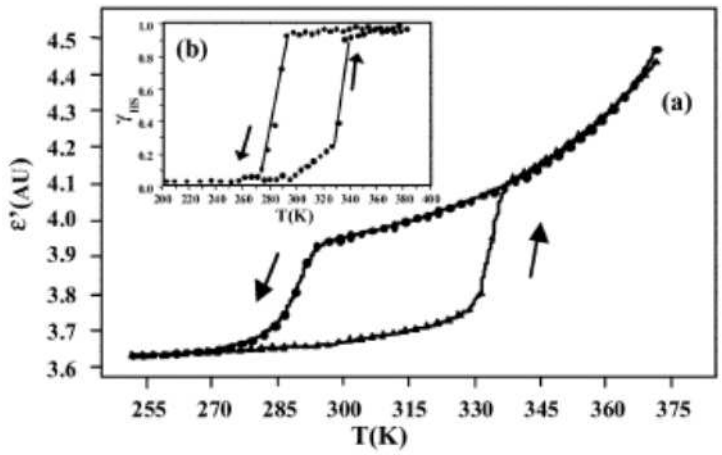

Figure 1.8. *Temperature dependence of the real part of the complex dielectric permittivity of the SCO complex $[Fe(NH2trz)_3](NO_3)_2$. The inset shows the HS fraction as a function of T [15].*

To overcome these issues, two main research strategies have been devised. On one hand, the chemical synthesis of novel SCO complexes incorporating conducting molecular bricks has afforded for several outstanding materials combining the two properties (see for example Fig. 1.9), sometimes even in a synergistic manner [17-19]. In addition, efforts have been also devoted to synthesize compounds with more pronounced permittivity changes [20-22]. Despite the remarkable sophistication of these different compounds, it appears, however, difficult to control simultaneously the electrical and SCO properties in a given compound to such an extent that they both fulfill technological requirements (e.g. high conductivity, room temperature SCO, robustness, etc.).

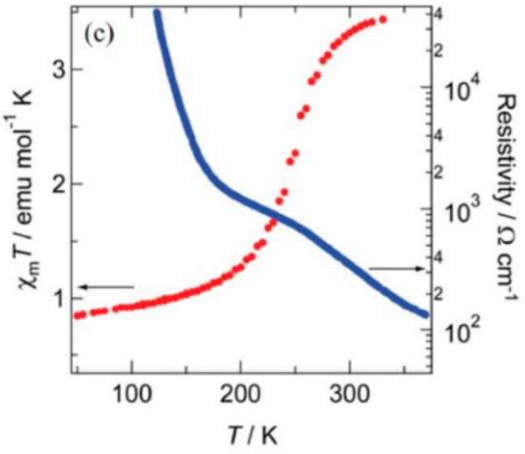

Figure 1.9. *Magnetic susceptibility and electrical resistivity of the SCO compound [Fe(dppTTF)2][Ni(mnt)2]2(BF4)·PhCN at variable temperature [18].*

On the other hand, a second research strategy aims at integrating SCO compounds together with various electroactive materials into hybrid systems, such as particulate composites, core-shell or multilayer structures. The goal here is to convey the SCO bistability into the electrical properties of other materials (e.g. resistance or capacitance switching, stimuli responsiveness, self-sensing) or, *vice versa*, to use the properties of the latter to influence the SCO behavior. Beyond these primary aims, researchers also seek to use the coupling between SCO and electroactive materials to develop unprecedented properties and thus devise novel applications of SCO materials, for instance, for transducing different forms of energy. The following sections of this chapter aim to provide an overview on this second research line, focusing on different classes of electroactive materials (2D materials, metallic nanoparticles, conducting polymers/composites, piezoresistive and piezo/ferroelectric materials), which have been used in combination with SCO materials.

1.2.*Coupling SCO compounds with 2D materials for synergistic electrical properties*

Recently, there have been remarkable advancements in the field of SCO research regarding the integration of graphene and other atomically thin 2D materials into heterostructures with SCO complexes. At the onset, these studies aimed at developing synergies between the SCO phenomenon and the attractive electrical properties of graphene, combining high conductivity and high sensitivity to external stimuli (mechanical, electrostatic, …). To this

aim, various graphene based transistor devices were made using spin crossover nanoparticles [23-25], single crystals [26-27] and thin films deposited by thermal evaporation [28-30]. Further works extended the scope to 2D transition metal dichalcogenides (MoS_2 [31], $NbSe_2$, WSe_2 [27]) as well as to carbon nanotubes, CNTs, [32]. (The latter can be seen as "rolled up", tubular sheets of graphene.) These works revealed interesting link(s) between the charge mobility in the 2D materials and the spin state of the SCO compounds, seen experimentally as a modulation of the electrical resistance of the former at the spin transition.

In 2017, Dugay et al. [23] fabricated a device that combined chemical vapor-deposited, CVD, graphene (deposited on a Si/SiO_2 substrate) and $\{[Fe(Htrz)_2(trz)](BF_4)\}$ (trz = 1,2,4-triazolato) spin crossover nanoparticles (Fig. 1.10). The latter were deposited on top of the graphene layer in the form of a thin particulate film using a micro-contact printing technique.

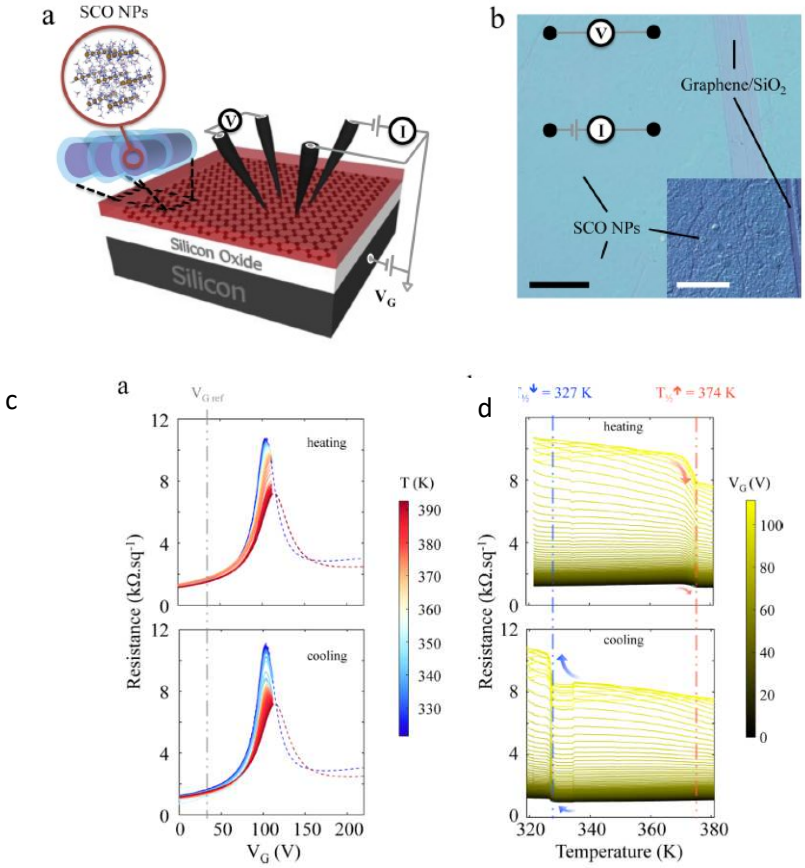

Figure 1.10. *(a) Schematic representation of the device based on graphene covered with a layer of particulate SCO film. (b) Top view image of the device. (c-d) Sheet resistance of the graphene/SCO device as a function of (c) the gate voltage (at selected temperatures) and (d) the temperature (at selected gate voltages). Reprinted with permission from Ref. [23].*

The resistance of the device was investigated both before and after the deposition of the SCO particles. After annealing the device, but before SCO deposition, the variation of the gate voltage revealed a resistance peak, associated with the Dirac point, at about +28 V. The temperature dependence of the resistance showed a monotonous and reversible linear change. Following the deposition of the SCO layer, an upshift of the Dirac point voltage and a general

rise in resistance values was observed, which could be attributed to combined effects of charge transfer and charge carrier scattering at the SCO/graphene interface. More importantly, significant and reversible changes in the resistance and associated charge carrier mobility of the graphene were observed at the spin transition, the device being ca. 25-30 % more conducting in the HS state (Fig. 1.10). On the other hand, the Dirac point of the device remained relatively stable at the spin state transition. The authors argued that the most likely mechanism coupling the SCO phenomenon to the charge carrier mobility could be a modification of the charge carrier scattering efficiency by interfacial phonons due to the different dielectric permittivity of the SCO particles in the HS and LS states. This first remarkable result was obtained in direct contact between the SCO material and the graphene layer. Later, in 2020, van Geest et al. [26] have shown that coupling of the SCO properties with the charge transport in the graphene can be also achieved by inserting a spacer between the two materials. The authors fabricated a graphene field effect transistor type device that had incorporated a single-crystal of [Fe(bapbpy)(NCS)2], (bapbpy = N,N′-di(pyrid-2-yl)-2,2′-bipyridine-6,6′-diamine). The crystals of SCO were grown directly on silicon wafer to the size of tens/hundreds of micrometers. A layer of epoxy resin was used to remove the crystals from the wafer surface. Then, a layer of PMMA (Poly(methyl methacrylate)) as well as source and drain electrodes were deposited on the free surface of the crystal. This was completed by a graphene layer and an additional layer of PMMA. Gating of the device was achieved using an ionic liquid (Fig. 1.11).

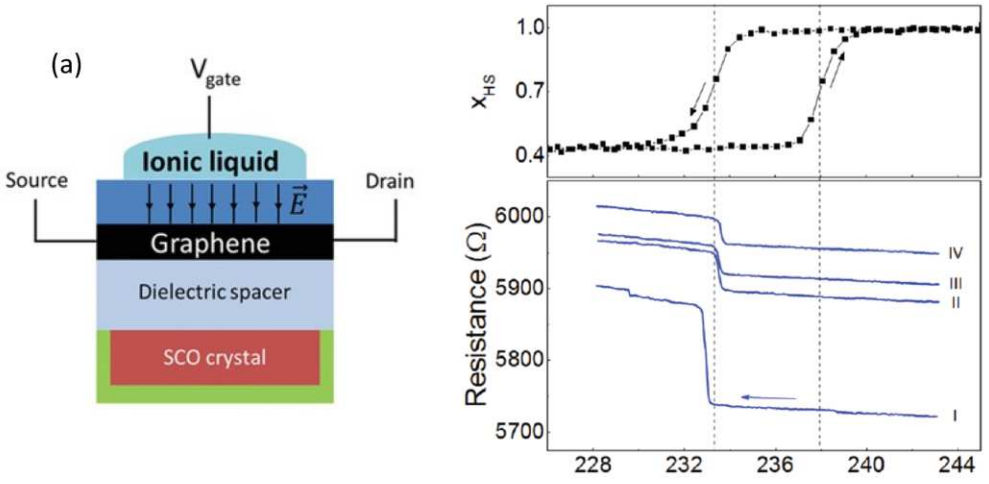

Figure 1.11. *(a) Schematic view of the epoxy (green)/ SCO single crystal (red)/ PMMA (blue)/ graphene (black)/ PMMA device. (b) Device resistance measured in 4 cycles (indicated I–IV) in the cooling regime and the HS fraction (black) of the bulk sample. Reproduced with permission from ref. [26].*

In the resulting device the SCO properties were retained and the device resistance showed repeatedly a small, but clear variation at the spin transition temperature. Again, the resistance of the graphene was found smaller in the HS state by a few percent. On the other hand, after each cycle the total resistance was increasing, most likely due to cracks that were formed in the SCO crystal. The authors have studied the spin state dependence of the device resistance for different PMMA spacer thicknesses (0, 0.1, 0.3 and 0.5 μm) between the SCO

crystal and graphene. Regardless the thickness of the PMMA spacer, a resistance modulation at the SCO temperature could be observed, but with different amplitudes and signs. For example, at a thickness of 0.5 μm, the coefficient of resistance variation $\Delta R/R_0$, where ΔR is the resistance difference before and after the spin transition, and R_0 is the resistance just before the transition, was positive (resp. negative) when going to the LS (resp. HS) state. For devices with thinner spacers (0 and 0.1 μm), the change of resistance was always positive regardless of spin state transition direction, showing the critical role of the polymer spacer in the mechanism. A change of Dirac point with changing temperature was also reported, but the correlation with the spin states was less obvious. Using Raman spectroscopy, the authors investigated if the spin transition might give rise to mechanical strain in the graphene layer, but within the experimental uncertainty, they could not reveal any significant effect. Given this observation and taking into account the presence of the spacer layer, they have thus argued that the main effect must be electrostatic and suggested it should be linked to the variation of the dipole moment of the molecules at the spin transition.

Instead of heating the whole device, one can also use more localized heating of the SCO layer. For example, Dayen et al. [24] used photo-thermal effect to this aim. In their approach, the device was fabricated using chemical vapor deposition (CVD) graphene, which was transferred on top of a SiO_2/Si substrate. A 300 μm channel was created between the source and drain electrodes, which were deposited on top of the graphene. The p-doped Si substrate was used as the gate electrode. SCO particles of $Fe(Htrz)_2(trz)](PF_6)$ were finally drop casted on the graphene surface. A specific interest of this particular SCO compound is that the thermal hysteresis loop associated with the spin transition encompasses the room temperature, i.e. a remnant photothermal switch (one way) could be achieved in ambient conditions using a red laser. Figure 1.12a shows an experiment, which combines both thermal cycling of the whole device as well as photothermal switching, while probing the spin state changes through the measurement of the electrical conductance of the graphene layer. In line with the above studies, switching to the HS state results in a resistance drop (here by ca. 2%).

A similar device was also reported wherein a thin film of the SCO complex $Fe[HB(3,5\text{-}(Me)_2pz)_3]_2$ (pz = pyrazolyl) was evaporated over a graphene layer in vacuum [28]. The temperature dependence of the conductivity of the graphene is shown in Figure 1.12b revealing a resistance switch of ca. 5 % upon the thermally induced spin transition near 150 K. Interestingly, though perhaps not surprisingly, light induced excited state spin trapping (LIESST) and reverse-LIESST effects give rise also to noticeable increase and decrease of the conductance, respectively. In both works [24, 28], the authors reported on a small, but significant difference in the current vs. gate voltage transfer curves recorded in the HS and LS states. Since these curves could be recorded at the same temperature (owing to the SCO memory effect), they concluded that the spin state switching gives rise to a change of the hole doping level of the graphene, most likely due to the modification of the electrical dipoles in the SCO material. Recent work on a SCO/graphene device using impedance spectroscopy and Hall measurements further confirmed the idea that graphene detects the SCO phenomenon through a change of the carrier densities in graphene due to electrostatic effects brought into by the SCO

nanoparticles [25]. Nevertheless, it should be noted that parallel studies on Fe[HB(3,5-(Me)$_2$pz)$_3$]$_2$/graphene devices incorporating a polymer spacer layer between the graphene and the SCO film reached a different conclusion [29]. Based on quantum chemical calculations, the authors argued that the dipole moment of this high symmetry SCO compound displays only negligible changes at the SCO (ca. 10^{-2} Debye). They then suggested that strain effects in the graphene, arising from the volume change of the SCO material, should be responsible for the resistance change of graphene at the spin transition. The same authors have also explored the behavior of a series of novel evaporable SCO molecules belonging to the {Fe[H$_2$B(pz)$_2$]$_2$(L)} family (with bidentate-α-diimine ligands, L) deposited on CVD-graphene [30]. Unfortunately, the SCO in the films becomes rather incomplete and gradual, making more difficult to establish a link between the spin state of the molecules and the electrical properties of graphene.

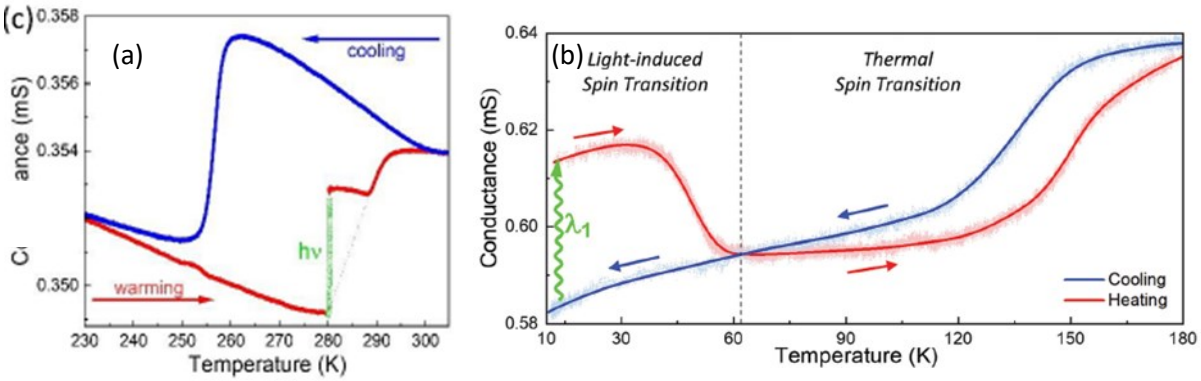

Figure 1.12. *(a) Temperature dependent (red/blue lines) and photo-thermally induced conductivity change (green arrow) in an SCO/graphene bilayer device. Reprinted with permission from ref. [24]. (b) Temperature dependence of conductance of a SCO/graphene device displaying both light induced (green arrow) and thermal (red/blue lines) spin transition. Reprinted with permission from ref. [28].*

Another very interesting SCO/graphene device configuration was reported by Boix-Constant et *al.* [27]. The authors used thin (few hundreds of nm) single crystals of the SCO complex {Fe-(3-Clpyridine)$_2$[Pt^{II}(CN)$_4$]} and a mechanically exfoliated few layer graphene (FLG) was placed either below or above the crystal. Similar configurations were also achieved using semiconducting WSe_2 and conductive $NbSe_2$ layers, instead of the FLG. In some devices, the SCO crystal and the FLG layer were separated by an insulating hexagonal boron nitride (h-BN) layer. As shown in Figure 1.13, the effect of the spin transition was observable in all types of FLG-based devices, whereas it was not observable in devices with $NbSe_2$. In the presence of the h-BN spacer, the device resistance decreased, but more importantly, the effect of the SCO on the resistance become relatively small. The authors suggested that mechanical strain, due to the ca. 8 % volume change at the SCO, should be at the origin of the coupling of the electrical resistance of the FLG with the spin transition. To support this hypothesis, they recorded the photoluminescence (PL) signal of similar van der Waals heterostructures made of WSe_2, including WSe_2/SCO, SCO/WSe_2, WSe_2/h-BN/SCO, SCO/h-BN/WSe_2 configurations. In each case, they observed an anomalous (reversible) blueshift and broadening of the PL signal when switching the SCO crystal to the LS state, similar to what could be observed from WSe_2 under

a compressive strain of ca. 3%. With a similar idea in mind, Torres-Cavanillas et al. [31] covalently grafted SCO nanoparticles onto semiconducting MoS_2 flakes. Transport measurements on the pelletized composite materials revealed unambiguous signature of the SCO phenomenon, with the HS state being ca. one order of magnitude more conducting. The role of covalent grafting was also substantiated by comparisons with simple mixtures of the SCO nanoparticles and MoS_2 flakes. Additionally, photoluminescence measurements conducted on the SCO/MoS_2 heterostructures revealed considerable variations of the PL peak position and width, compatible with the hypothesis of a ca. 0.6 % tensile strain in the flakes when switching the SCO particles to the HS state.

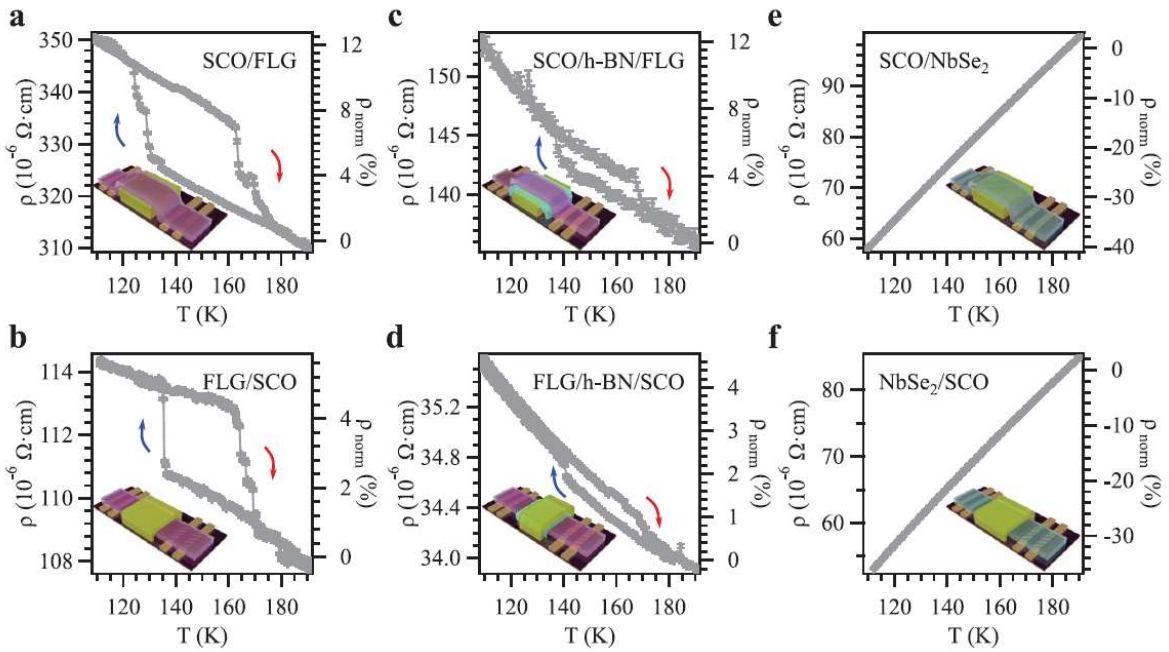

Figure 1.13. *Temperature dependence of the resistivity for SCO-graphene and SCO-NbSe2 devices with different configurations. The insets show the scheme of the devices. (The SCO, FLG, h-BN and NbSe2 layers are represented in yellow, purple, bright-blue and green colors, respectively.) Reproduced with permission from ref. [27].*

Besides the deposition of SCO materials on graphene sheets, it is also possible to encapsulate spin crossover molecules within carbon nanotubes to detect electrically the spin transition at the molecular level. In order to fabricate such a fine hybrid material, Villalva et.al. [32] used evaporable SCO molecules of formula $[Fe(H_2Bpz_2)_2(L)]$, where L is 1,10-phenanthroline or 2,2'-bipyridine (see Fig. 1.14a). The CVD-grown single-walled carbon nanotubes (SWCNT) with diameters ranging from 1.6 to 2.2 nm were opened by a thermal oxidation technique and where purified by using a series of acid washing processes. In order to encapsulate the SCO molecules inside, the molecules and the nanotubes were sealed under vacuum in a quartz ampoule and the mixture was heated to 150 °C for several days to sublimate the molecules (Fig. 1.14b). The presence of SCO molecules within the nanotubes was substantiated using a combination of thermogravimetry, electron microscopy and Raman spectroscopy analysis. Electron transport across individual SCO@SWCNT hybrids was probed in a solid-state field-effect tran-

sistor configuration (Fig. 1.14c), by trapping the nanotubes in electrode gaps using dielectrophoresis. The current vs. temperature measurements revealed abrupt changes upon cooling and heating (Fig. 1.14d), which could be ascribed to the effect of SCO molecules.

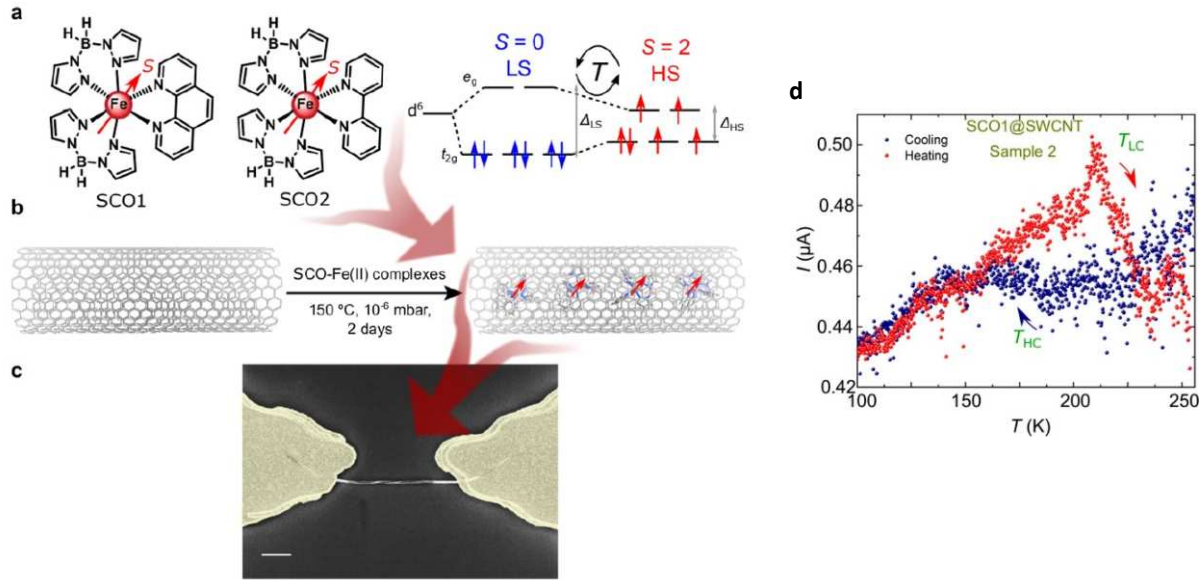

Figure 1.14. *(a) Chemical structure of the SCO molecules encapsulated in carbon nanotubes. (b) Schematic representation of SCO molecules inside a carbon nanotube. (c) SEM image depicting a SCO@SWCNT hybrid material connecting metallic electrodes. The scale bar is 500 nm. (d) Current versus temperature curve recorded for a SCO@SWCNT hybrid upon heating and cooling. Reproduced with permission from ref. [32].*

1.3.Coupling SCO compounds with metallic nanoparticles

Combining metallic nanoparticles (MNPs) with SCO materials could provide several benefits [33]. A potential advantage is that one can utilize the plasmonic effect of certain MNPs (Au, Ag, …) either to induce spin transition by efficient photothermal heating [34] or to detect the occurrence of SCO through the shift of the plasmonic resonance wavelength [35]. In the context of the present review, we will focus only on those works wherein MNPs were used to achieve high electrical conductivity within hybrid SCO-MNP systems. By this way, one can combine the stimuli-responsive properties of SCO complexes and the excellent electrical conductivity of MNPs. Of particular interest is the use of arrays of MNPs connected by SCO molecules (or thin SCO layers) wherein the charge transport can be assimilated to electrons jumping from one MNP to another. Since the limiting elements in the charge transport are the SCO molecules, any change in their length or polarizability, which could be expected to accompany the SCO event, should lead to a change of the current flow [36]. With this idea in mind, in 2014, Devid et al. [37] reported on 2D arrays of Au nanoparticles, which were bridged by SCO molecules of $[Fe(AcS\text{-}BPP)_2](ClO_4)_2$ (where AcS-BPP denotes S-(4-{[2,6-(Dipyrazol-1-yl)pyrid-4-yl]ethynyl}-phenyl)ethanethioate) and the ensemble was connected to patterned electrodes (Fig. 1.15a). These tiny junctions (AuNP-SCO-AuNP) were built by first constructing the MNP array with octanethiol-covered gold nanoparticles, followed by the exchange of the thiols with the SCO molecules. Temperature dependent Raman spectroscopy

and magnetic measurements were employed to detect the SCO in this hybrid system. The Raman data suggest that molecular binding to gold occurs via benzenethiol termini. However, it does not seem that the proximity and binding to the metal quench the spin transition. Interestingly, the arrays containing SCO molecules exhibit a pronounced minimum in the resistance vs. temperature curves, which is not observed in networks containing non-switching, passive molecules only. This finding was explained by a percolation model which assumes a spin transition, where the HS state is more resistive than the LS state. In a similar attempt, an MNP array with SCO complexes connecting 1.2 nm sized Pt nanoparticles was reported by Usmani et al. [38]. In this work, a chain-like FeL_3 complex was synthesized with the ligand L = (1E)-1-(thiophen-3-yl)-N- (4H-1,2,4-triazol-4-yl)ethan-1-imine. Due to the strong affinity between S and Pt, this SCO complex can coordinate to the Pt surface via self-assembly process affording for organized MNP arrays at sub-3 nm periodicity (Fig. 1.15b). By comparing the SCO properties of the complex itself and the Pt-SCO hybrid system, it was found that SCO in the latter case was much less complete and persisted only if the sample was not completely dry. Transport measurements were conducted on an interdigitated electrode device, where the 'gel state' hybrid system was drop casted on. Temperature dependent charge transport and magnetic measurements revealed connection between the SCO and charge transport properties between ~250-300 K.

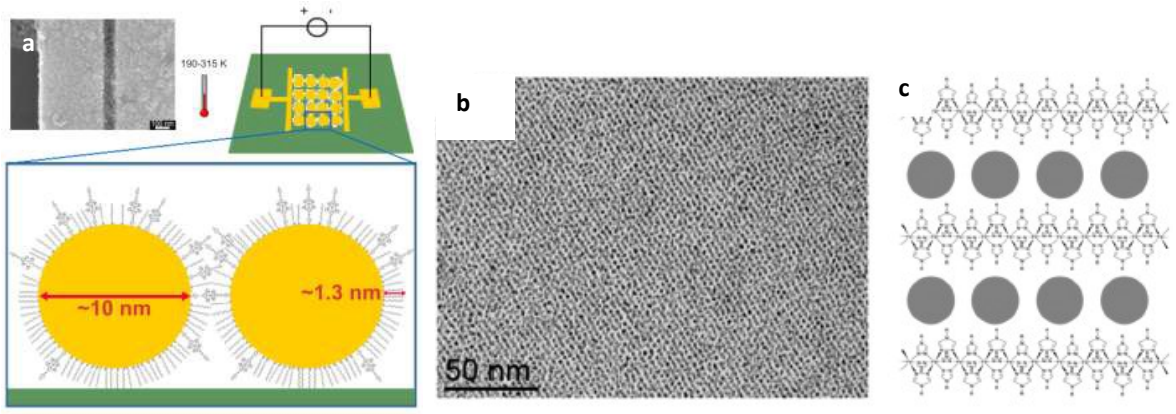

Figure 1.15. *(a) SEM micrograph and schematic representation of a SCO molecules-gold nanoparticle array device. Reproduced with permission from ref. [37]. (b) TEM image and (c) structural model of the self-assembly made of Pt nanoparticles and chain-like SCO coordination polymers. Reproduced with permission from ref. [38].*

In the previous examples, the SCO molecules were introduced either during or following the formation of the MNP arrays. Torres-Cavanillas et al. [39] proposed an approach the other way around. In this work Au particles of 12 nm were covered with a ca. 4 nm thin shell of the $\{[Fe(Htrz)_2(trz)](BF_4)\}$ SCO complex. The synthesis followed a two-step approach. First, they achieved a partial surface ligand substitution of the citrate-stabilized Au NPs. Secondly, the controlled growth of a very thin layer of the SCO complex was accomplished. The core-shell particles displayed cooperative spin transition in the range 340-360 K. Temperature-dependent charge transport measurements on interdigitated electrodes connected by assemblies of these Au@SCO NPs were carried out. The presence of the Au core allowed

for high current intensities and revealed a large change in conductance upon spin-state switching, with the LS state of the device being three orders of magnitude more conducting (Fig. 1.16). This is to be compared with the conductance switching in the neat {[Fe(Htrz)$_2$(trz)](BF$_4$)} SCO complex, which is typically observed between 1 – 2 orders of magnitude [40].

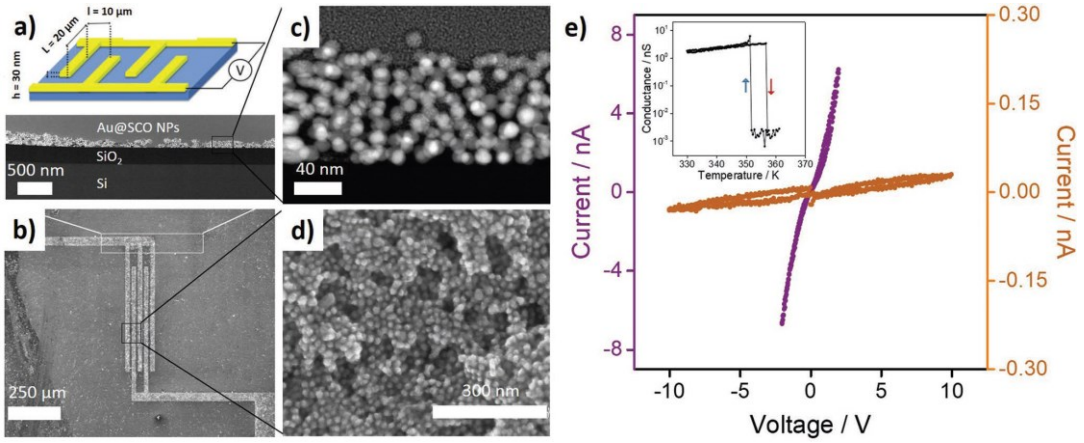

Figure 1.16. *a-d) Scheme and SEM images of the interdigitated electrode device connected by densely packed Au@SCO core-shell particles. e) I–V curves in the high-conductivity (purple) and low-conductivity (orange) states associated to the LS and HS forms, respectively. Inset: Thermal variation of the electrical current in the heating and cooling modes. Reproduced with permission from ref. [39].*

1.4. Coupling SCO compounds with electroactive polymers and polymer composites

Another category of promising spin crossover based electroactive hybrid systems combine SCO particles or films with electroactive polymers. The most straightforward systems are bilayer SCO/polymer devices, which have been fabricated either as bending cantilevers or on solid substrates. Alternatively, various composite materials with SCO particles embedded in different electroactive polymers were also reported. In general, the coupling between the constituents is achieved via mechanical stress and strain, though in a few cases electric field effects were also considered. In the case of cantilever devices, the mechanical stress and strain in the layers are fairly straightforward to evaluate from the experimentally observed bending of the cantilever, combined with well-known beam theories. On the other hand, when the multilayers are deposited on rigid substrates, for the lack of direct experimental observables, the assessment of mechanical effects remains in most cases rather difficult.

1.4.1.Freestanding spin crossover/polymer multilayers

To our best knowledge, the first SCO device using electrothermal actuation was reported by Gural'skiy et. al. [41] who fabricated a bilayer cantilever using two PMMA layers, one charged with [Fe(trz)(Htrz)$_2$]BF$_4$ particles and the other with silver flakes. The obvious interest of this system is that it does not require heat from an external source, but it is able to achieve self-heating by passing an electrical current through the electrically conducting Ag@PMMA layer. Upon this electrothermal actuation, the particles in the SCO@PMMA layer are switched to the HS state and the resulting strain mismatch between the two strata gives rise

to a bending motion of the cantilever. This first device was then improved by Piedrahita-Bello et al. [42], including the use of oriented, needle-shaped SCO particles, a blade casting method, precision laser cutting, different polymer matrices and SCO particles, an external position sensor, payloads and a closed-loop PID control system (Fig. 1.17a). It was shown that the appropriate choice of parameters (polymer compliance, SCO particle composition, concentration, and morphology) allows for large amplitude and even pre-programmed bending movements. The actuators displayed excellent controllability, both in open- and closed-loop configuration, positioning accuracy, fast response and long life cycle (Fig. 1.17b-1.17c).

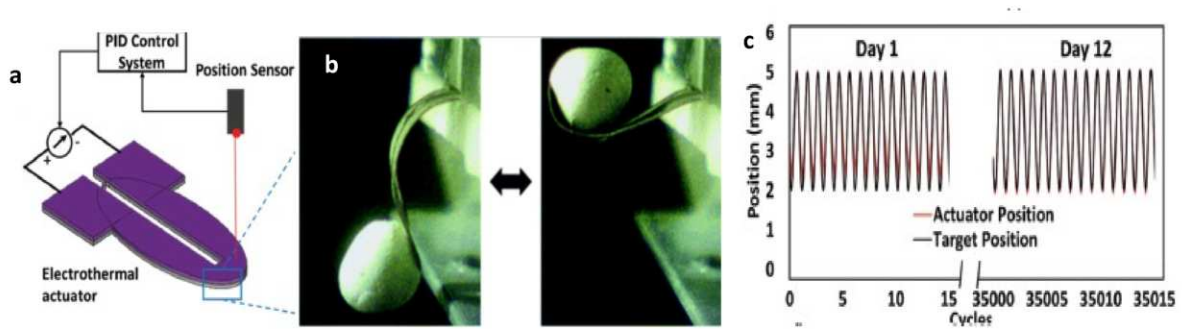

Figure 1.17. *(a) Scheme of a U-shaped bilayer SCO@polymer/Ag@polymer device actuated electrothermally and controlled in closed-loop using an external position sensor. (b) Photographs of a device lifting a payload. (c) Closed-loop test of the positioning accuracy of a device operated during two weeks over 35000 endurance cycles. Reproduced with permission from ref. [42].*

To achieve a higher degree of integration and autonomous actuator operation, without the need for numerous auxiliary devices, it is desirable to achieve also self-sensing capability, besides self-heating. This was achieved for the first time using an integrated piezoresistive polymer composite layer in ref. [43]. The authors fabricated a bilayer cantilever that contains an active layer of polycarbonate (PC) with embedded {[Fe(Htrz)$_2$(trz)](BF$_4$)} SCO particles and another layer, which is made of a constantan alloy placed in a polyimide(PI) matrix (Fig. 1.18). Due to the bending motion of the cantilever at the SCO, mechanical stress is generated in the PI layer, which gives rise to a change of the electrical resistance in constantan wire. The thermal hysteresis of the resistance perfectly matches that of the SCO.

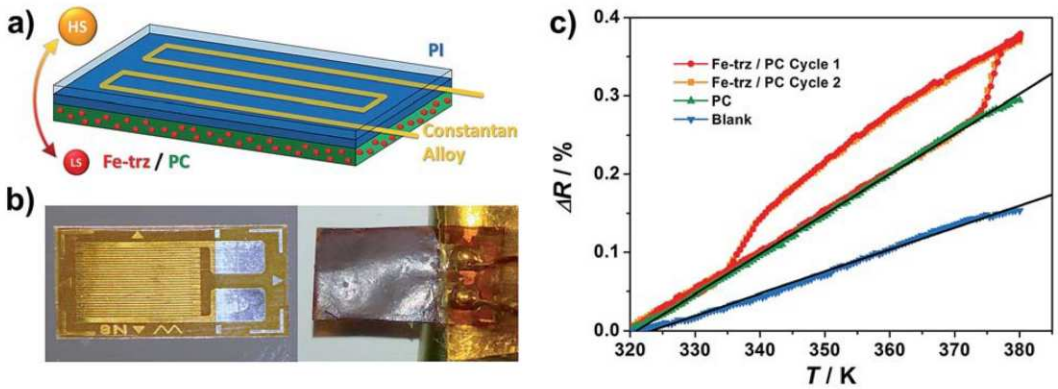

Figure 1.18. *(a) Scheme and (b) photograph of the bilayer SCO@PC/constantan@PI heterostructure and (c) the change in resistance at the SCO [43].*

Later on, a series of more sophisticated, micrometer sized devices were constructed using either polymer or silicon microcantilevers, equipped with integrated strain sensors [44-46]. Interestingly, these SCO-based microelectromechanical systems afforded for not only the detection of the static deflection of the cantilever induced by the SCO phenomenon, but also for the in-situ tracking of the cantilever dynamics (resonance frequency, damping).

1.4.2. Spin crossover/polymer multilayers on rigid substrates

Manipulation of the spin state of SCO materials by external electric fields is not considered viable due to the need for very strong fields (>> MV/m), even in compounds showing (relatively) large dielectric permittivity changes at the SCO [47]. However, opportunities might appear using directed local electric fields, for example at the interface of ferroelectric materials. In 2014, Zhang et al. [48] revealed that the stability of the HS and LS states can be modulated in thin films of the SCO compound $\{Fe(H_2B(pz)_2)_2(bipy)\}$ (bipy = 2,2'-bipyridine) by changing the polarization of the underlying ferroelectric substrate poly(vinylidene fluoride co trifluoroethylene), P(VDF-TrFE). This observation triggered a series of studies by the same group to better understand this effect and try to exploit it in electronic devices [49-54]. Notably, a multilayer configuration was studied (Fig. 1.19a), wherein an 80 nm thin Ti film was deposited on a Si wafer, covered by a 20 nm thick ferroelectric poly(vinylidene fluoride-co-hexafluoropropylene), PVDF-HFP, layer, and topped with a 65 nm film of $\{Fe(H_2B(pz)_2)_2(bipy)\}$ [52]. Polarization of the ferroelectric polymer was achieved by placing a removable copper electrode on top of the sample via a micrometer stage. The spin state of the SCO film was investigated as a function of the temperature using X-ray Absorption Spectroscopy (XAS), which indicated that the LS (resp. HS) state was significantly favored when the polarization direction was “down” (resp. “up”) (Fig. 1.19b). The authors estimated the electric field generated at the PVDF-HFP/SCO interface as high as 5 GV/m. Additionally, $\{Fe(H_2B(pz)_2)_2(bipy)\}$ films were deposited on interdigitated electrodes to investigate the dependence of charge transport on the spin state. In a parallel experiment, a similar device was fabricated wherein the SCO layer was covered with a layer of a ferroelectric polymer film (Fig. 1.19c-d). The authors found that the device was more conductive at 298 K (vs. 150 K), and that conductivity increased when the ferroelectric polarization was oriented towards the substrate (vs. away) at a fixed temperature. They argued that the higher conductivity in both cases could arise from the difference in spin states (HS more conducting vs. LS), which were induced either by temperature changes or polarization direction modifications. The latter signifies that isothermal spin state switching accompanying can accompany the polarization switching.

Controversy about these results has aroused when another group reported on a similar SCO/ferroelectric bilayer structure, where the underlying ferroelectric substrate used the material, PMNPT $\{[Pb(Mg_{1/3}Nb_{2/3})O_3]_{0.68}[PbTiO_3]_{0.32}\}$ [55]. X-ray absorption spectroscopy revealed that the ferroelectric polarization does not affect temperature induced spin-crossover behavior down to 100 K. However, at 3 K in the soft X-ray induced excited spin-state trapping (SOXIESST) regime, significant differences were observed between the two ferroelectric polarizations. Compared to the (-) poled sample (negative applied voltage at the back side of

the sample, the electric dipole moment points towards the surface), the (+) poled sample exhibited more than one order of magnitude higher efficiency in exciting LS molecules to the HS state via the SOXIESST effect, which the authors explained by electrostatic interactions between the secondary electrons generated by the incident x-ray beam and the polarized ferroelectric layer. In other words, the HS state of {Fe(H_2B(pz)$_2$)$_2$(bipy)} would be favored in these experiments by the ferroelectric material being poled "up" only indirectly, due to the influence of the ferroelectrics on the efficiency of the SOXIESST effect. In Chapter 2 of this thesis we will bring further analysis of this topic.

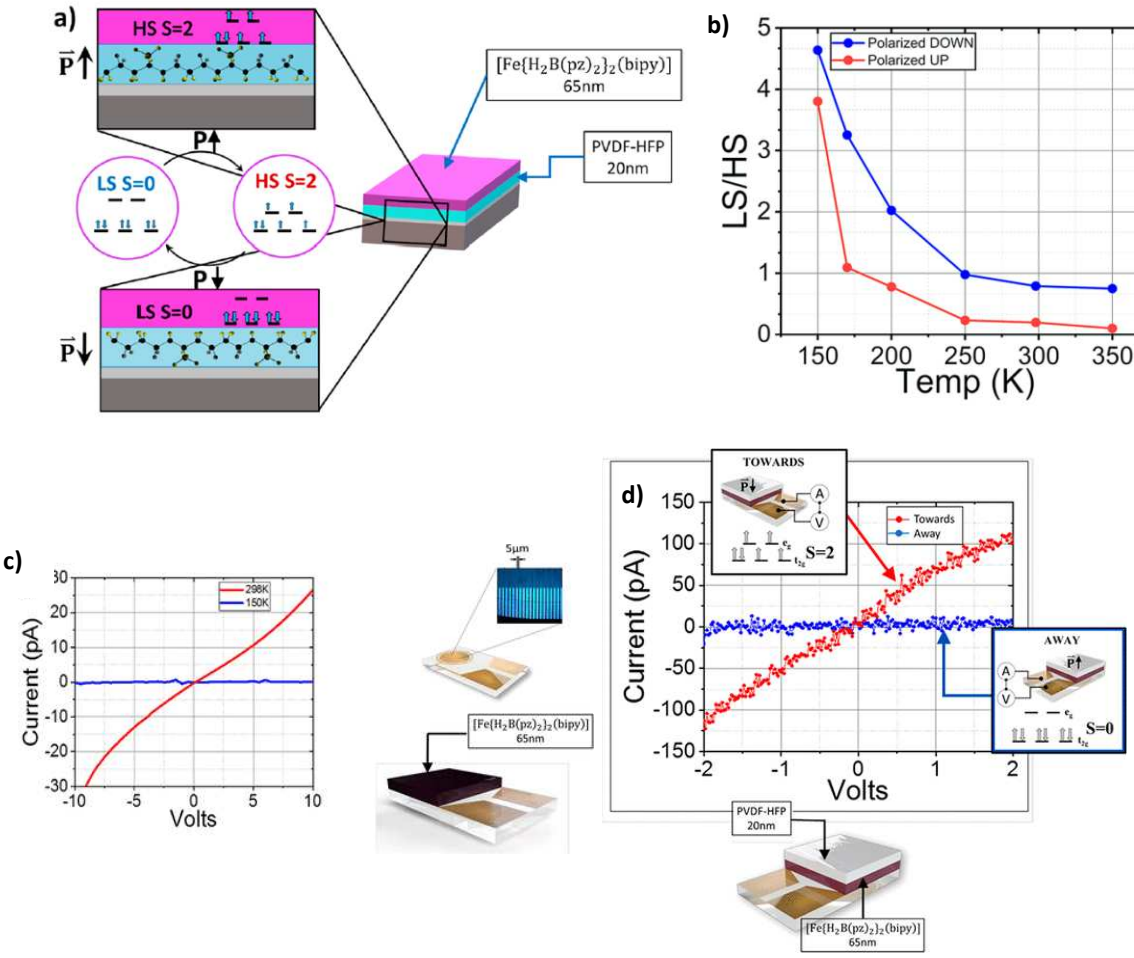

Figure 1.19. *(a) Scheme of the SCO/ferroelectric bilayer and the influence of the ferroelectric polarization direction on the molecular spin states. (b) X-ray absorption measurement of the ratio of LS and HS molecules in the film depending on the polarization direction in the underlying piezopolymer substrate. (c) Scheme of an interdigitated electrode device with an SCO film and current vs. voltage curves recorded at 150 K and 298 K. (d) Scheme of the ferroelectric/SCO bilayer on the interdigitated electrodes and current vs. voltage curves in the two polarization directions (isothermal). Reproduced with permission from ref. [52].*

In a different approach, Zhang et al. [56] recently reported a SCO composite/polymer semiconductor bilayer configuration implemented into an organic field-effect transistor (OFET) device (Fig. 1.20a). A spin coating protocol was applied to deposit the bilayer on bottom-gate-bottom-contact transistors. Thanks to the use of orthogonal solvents, the interface between the

P3HT (poly(3-hexylthiophene)) polymer layer and the {[Fe(Htrz)$_2$(trz)](BF$_4$)}@PVP (polyvinylpyrrolidone) composite layer remained well-defined after the deposition process, as shown in Figure 1.20b. The SCO phenomenon in this hybrid system was characterized by temperature dependent UV-Vis spectroscopy as well as by charge transport measurements. The latter consistently revealed in a series of devices with different geometries and measurement conditions a ca. 50-70 % increase of the drain-source current when switching the SCO particles from the LS to the HS state. This behavior was shown to be reversible for (at least) 30 heating-cooling cycles. Further analysis through capacitance measurements and finite element calculations allowed to suggest that the resistance switching observed in the organic semiconductor layer is not a result of an electrostatic effect, but should be attributed to the mechanical stress induced by the spin state switching of the SCO particles. Interestingly, the resistance switching was also observed in the transistor OFF state, suggesting that this type of coupling could be achieved also in less sophisticated two-terminal devices.

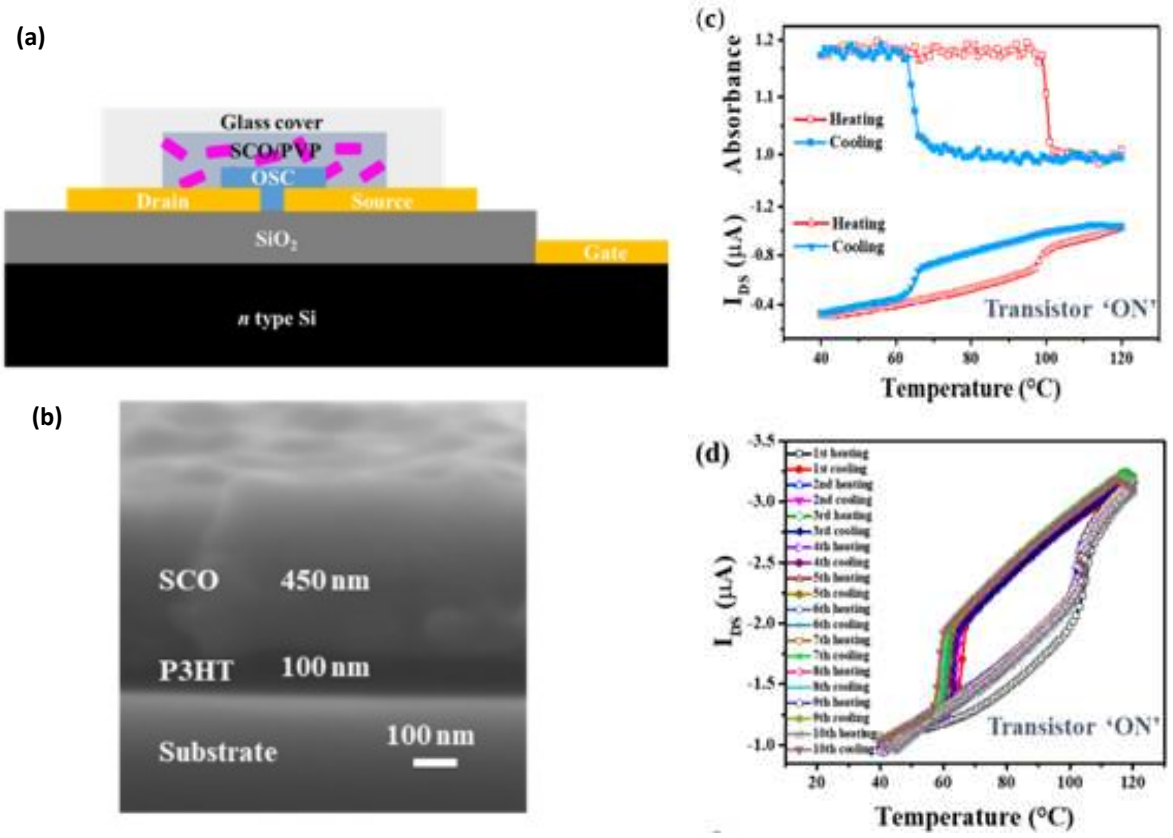

Figure 1.20. *(a) Scheme of the cross-section of the SCO-OFET device. (b) SEM image of the device cross-section. (c) Temperature dependent charge transport in the transistor ON state (gate voltage: -10 V). For comparison, the UV absorbance change at 350 nm of the SCO@PVP-P3HT bilayer film is also shown. (d) Drain-source current during ten successive thermal cycles for an SCO-OFET device. Reproduced with permission from ref. [56].*

1.4.3. Spin-crossover@polymer composites displaying electromechanical couplings

In 2014 Koo et al. [57] reported in a pioneering study the modulation of electrical conductivity in composite materials combining an SCO complex, $[Fe(trz)(Htrz)_2](BF_4)$ or $[Fe(trz\text{-}NH_2)_3](BF_4)_2$, with the conductive polymer polypyrrole (PPY). Both composites preserved the spin crossover properties, while maintaining also a relatively high level of electrical conductivity. Most remarkably, a substantial change in the conductivity of the composites was observed at the spin state transition temperatures, reaching ca. 65 % for the $\{[Fe(trz)(Htrz)_2](BF_4)\}$/PPY and 50 % for the $\{[Fe(trz\text{-}NH_2)_3](BF_4)_2\}$/PPY system (Fig. 1.21).

Based on these findings, subsequent studies [58-59] explored the interplay between the spin transition and the electrical conductivity of various SCO-based composite materials using different conducting polymers, including PPY, poly(3,4–ethylenedioxythiophene)-paratoluenesulfonate (PEDOT-PT), polyaniline-sulfate (PANI) and poly(3,4-ethylenedioxythiophene)-poly(styrenesulfonate) (PEDOT-PSS). The SCO/polymer composites were prepared by mechanically milling the mixtures of SCO powders and polymers in several weight ratios (1:1, 1:3, and 1:5). The charge transport characteristics of the composites were strongly dependent on the concentration of SCO particles within the composite. At a 1:1 concentration ratio, the conductivity was solely temperature-dependent, showing typical semiconductive behavior across the entire temperature range, except for the PEDOT-PT 1:1 composite, wherein the spin transition was also observed in the conductivity measurements. On the other hand, for composites with higher SCO load (1:3 and 1:5), the conductivity showed a strong dependence with the spin state in each case, reaching a ca. one order of magnitude difference between the LS and HS forms, the latter being always more conducting. The authors argued that the conductivity change at the SCO arises due to the volume change of the SCO particles, giving rise to a change of the percolation network in the conductive polymer matrix.

In this context, it is interesting to note that SCO-PPY composite materials could be recently obtained also by the in-situ polymerization of PPY within the pores of the metal-organic framework $\{Fe(pyrazine)[Ni(CN)_4]\}$ resulting of a six orders of magnitude enhancement of the conductivity of the latter [60]. In Chapter 5 of this thesis we will develop some complementary strategies along this line of research.

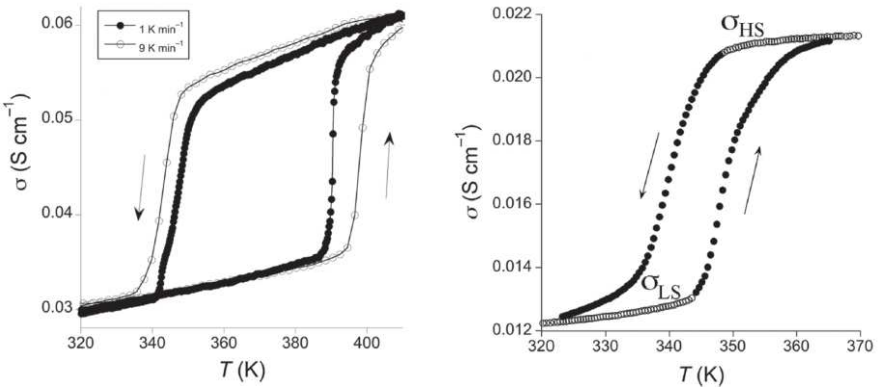

Figure 1.21. *Electrical conductivity as a function of the temperature measured in $[Fe(trz)(Htrz)_2][BF_4]$@PPY (left) and $\{[Fe(trz\text{-}NH_2)_3][BF_4]_2\}$@PPY (right) composite materials. Reproduced with permission from ref. [57].*

The volume changes associated with spin transitions in SCO materials make them also ideal for actuating piezoelectric (PE) materials, such as PVDF and P(VDF-TrFE). This approach leverages the SCO-induced mechanical stress to generate electrical charges by the direct PE effect. With this idea in mind, a series of composites were prepared in our group by mixing P(VDF–TrFE) copolymers with different SCO materials at different concentrations [61, 13]. To create the composite, particles were dispersed in a 2-butanone solution with the polymer and the solution was blade cast onto a Teflon substrate. The dried films were annealed and polarized. It is important to note that the selected copolymers with 70/30 and 75/25 VDF/TrFE ratios display Curie temperatures above the SCO temperature of the particles used, which is mandatory to maintain the ferroelectric polarization. As it could be expected, with increasing SCO particle concentration, the PE properties of the composite materials degraded, witnessed by lower piezoelectric charge coefficients, d_{33}. Remarkably, for optimized concentrations and compositions, the composites generated a peak of electrical current at the spin state transition temperature when the short-circuited sample was thermally cycled under zero applied electrical bias. This original phenomenon corresponds thus to a two-step thermal energy harvesting process with successive thermal-to-mechanical (SCO) and mechanical-to-electrical (PE), which will be the topic of Chapter 4 of this thesis. With a similar idea in mind, but using a different experimental approach, Koo et al. [62] investigated a ferroelectric $[Fe(NH_2trz)_3](NO_3)_2$@PVDF composite film. When investigating the ferroelectric hysteresis (i.e. polarization vs. electric field), the authors reported on a spin state dependent saturation polarization and coercive field, revealing thus novel facets of the coupling between the SCO particles and the ferroelectric matrix.

1.5. Conclusions and outlook

The ‘spin crossover community’ has made significant progress in fabricating and understanding hybrid SCO - electroactive materials and structures, revealing their potential for a wide range of applications requiring thermal bistability.

However, as we have discussed above, the possible effect of electric fields on the spin state of SCO materials within these hybrid systems remains rather elusive, in spite of the huge interest of electric-field control of the switching process. In this context, several experiments indicated that the spin state of SCO molecules deposited on a ferroelectric polymer depends on the polarization of the latter. These effects require further clarification both from the experimental and theoretical points of view, but the idea of benefiting from the existence of intense local electric fields at interfaces appears very attractive for the manipulation of the spin state equilibrium and dynamics. We will examine some aspects of this interesting question more in detail in Chapter 2 of the present thesis.

Remarkably, some of these hybrid materials afforded for unprecedented properties as well. For example, by incorporating SCO materials into composites with piezopolymers, new opportunities for thermal energy harvesting have emerged, whereas the combination of SCO materials with conductive polymers could facilitate the use of SCO materials in redox active systems, for example in batteries and supercapacitors. A common open challenge towards these different developments is the better understanding of the mechanisms, which provide coupling

between the SCO and electroactive components. Indeed, among the various mechanisms proposed, up to now, only the coupling via mechanical stress and strain could be firmly established in a few cases. Starting from these ideas, Chapter 3 of the present thesis will examine some novel fabrication methods and dielectric properties of the resulting composite materials, in view of possible piezoelectric and charge storage applications in SCO-based capacitors. On the other hand, in Chapter 4 we will disclose a novel strategy to construct a hybrid SCO- piezoelectric energy harvesting device.

Importantly, the integration of 2D materials such as graphene, metallic particles and electroactive polymers with SCO materials has extended the variety of detection mechanisms of spin transitions towards electrical measurements, even at reduced micro/nanometric size scales. This advancement facilitates the development of highly sensitive sensors for various applications, including temperature, pressure and chemical sensing/monitoring. On the other way around, it provides also prospects for electrical self-sensing, for example in SCO-based mechanical actuator devices. This aspect of electrical sensing will be investigated in Chapter 5 of this thesis, along two novel ideas.

References

[1] Gütlich P., Hauser A., & Spiering H., Thermal and Optical Switching of Iron(II) Complexes, Angew. Chem. Int. Ed. 33.20 (1994) 2024-2054.

[2] M. A. Halcrow (ed.), „Spin crossover materials: properties and applications", J. Wiley & Sons, 2013.

[3] Gütlich P., Goodwin H.A., „Spin Crossover in Transition Metal Compounds I-III", Top. Curr. Chem (2004), vols. 233-235.

[4] G. Molnár, S. Rat, L. Salmon, W. Nicolazzi, A. Bousseksou, Spin Crossover Nanomaterials: From Fundamental Concepts to Devices, Adv. Mater., 2018, 30, 1703862.

[5] O. Kahn, J. Kröber, C. Jay, Spin transition molecular materials for displays and data recording, Adv. Mater., 1992, 4, 718.

[6] P. Mounaix, E. Freysz, J. Degert, N. Daro, J.-F. Létard, P. Kužel, V. Vigneras, L. Oyenhart, One-dimensional tunable photonic crystals with spin crossover material for the terahertz range, Appl. Phys. Lett., 2006, 89, 174105.

[7] K. Ridier, A. C. Bas, Y. Zhang, L. Routaboul, L. Salmon, G. Molnár, C. Beragud, A. Bousseksou, Unprecedented switching endurance affords for high-resolution surface temperature mapping using a spin-crossover film, Nat. Commun., 2020, 11, 3611.

[8] M. Ohba, K. Yoneda, G. Agustí, M. C. Munoz, A. B. Gaspar, J. A. Real, J. A., José A. Real, M. Yamasaki, H. Ando, Y. Nakao, S. Sakaki, S. Kitagawa, Bidirectional chemo-switching of spin state in a microporous framework, Angew. Chem. Int. Ed., 2009, 48, 4767.

[9] D. Gentili, N. Demitri, B. Schäfer, F. Liscio, I. Bergenti, G. Ruani, M. Ruben, M. Cavallini, Multi-modal sensing in spin crossover compounds, J. Mater. Chem. C, 2015, 3, 7836.

[10] H.J. Shepherd, I.y.A. Gural'skiy, C.M. Quintero, S. Tricard, L. Salmon, G. Molnar, A. Bousseksou, Molecular actuators driven by cooperative spin-state switching, Nature Communications, 4 (2013) 2607.

[11] S. P. Vallone, A. N. Tantillo, A. M. Dos Santos, J. J. Molaison, R. Kulmaczewski, A. Chapoy, P. Ahmadi, M. A. Halcrow,K. G. Sandeman, Giant Barocaloric Effect at the Spin Crossover Transition of a Molecular Crystal, Adv. Mater., 2019, 31, 1807334.

[12] E. Resines-Urien, M. A. G. García-Tuñón, M. García-Hernández, J. A. Rodríguez-Velamazán, A. Espinosa, J. S. Costa, Concomitant Thermochromic and Phase-Change Effect in a Switchable Spin Crossover Material for Efficient Passive Control of Day and Night Temperature Fluctuations, Adv. Sci., 2022, 9, 2202253.

[13] M. Piedrahita-Bello, B. Martin, L. Salmon, G. Molnar, P. Demont, A. Bousseksou, Mechano-electric coupling in P(VDF-TrFE)/spin crossover composites, Journal of Materials Chemistry C, 8 (2020) 6042-6051.

[14] A. Rotaru, I. A. Gural'skiy, G. Molnar, L. Salmon, P. Demont, A. Bousseksou, Spin state dependence of electrical conductivity of spin crossover materials, Chem. Commun., 2012, 48, 4163.

[15] A. Bousseksou, G. Molnár, P. Demont, J. Menegotto, Observation of a thermal hysteresis loop in the dielectric constant of spin crossover complexes: towards molecular memory devices, J. Mater. Chem., 2003, 13, 2069.

[16] C. Lefter, et al. "Charge transport and electrical properties of spin crossover materials: towards nanoelectronic and spintronic devices." Magnetochemistry 2.1 (2016): 18.

[17] M. Wang, Z. Y. Li, R. Ishikawa, M. Yamashita, Spin crossover and valence tautomerism conductors, Coord. Chem. Rev., 2021, 435, 213819.

[18] M. Nihei, N. Takahashi, H. Nishikawa, H. Oshio, Spin-crossover behavior and electrical conduction property in iron(ii) complexes with tetrathiafulvalene moieties, Dalton Trans., 2011, 40, 2154.

[19] K. Takahashi, et al. "Evidence of the chemical uniaxial strain effect on electrical conductivity in the spin-crossover conducting molecular system:[FeIII (qnal) 2][Pd (dmit) 2] 5· acetone." Journal of the American Chemical Society 130.21 (2008) 6688-6689.

[20] Y.-R. Qiu, et al. "Enhanced dielectricity coupled to spin-crossover in a one-dimensional polymer iron (II) incorporating tetrathiafulvalene." Chem. Sci. 11 (2020) 6229-6235.

[21] H. Zheng, et al. "Simultaneous Modulation of Magnetic and Dielectric Transition via Spin-Crossover-Tuned Spin Arrangement and Charge Distribution." Angewandte Chemie International Edition 57.28 (2018): 8468-8472.

[22] Y. Uezu, et al. "Spin Crossover between the High-Spin and Low-Spin States and Dielectric Switching in the Ionic Crystals of a Fe (II)[2× 2] Molecular Grid." Bulletin of the Chemical Society of Japan 93.12 (2020): 1583-1587.

[23] J. Dugay, M. Aarts, M. Giménez-Marqués, T. Kozlova, H.W. Zandbergen, E. Coronado, H.S.J. van der Zant, Phase Transitions in Spin-Crossover Thin Films Probed by Graphene Transport Measurements, Nano Letters, 2017, 17, 186.

[24] J.F. Dayen, N. Konstantinov, M. Palluel, N. Daro, B. Kundys, M. Soliman, G. Chastanet, B. Doudin, Room temperature optoelectronic devices operating with spin crossover nanoparticles, Materials Horizons, 8 (2021) 2310-2315.

[25] Maity, K., Dayen, J. F., Palluel, M., Daro, N., Chastanet, G., Kundys, B., & Doudin, B. (2023). Elucidating the effect of spin crossover materials on graphene sensing devices. Appl. Phys. Lett. 123.16.

[26] E.P. van Geest, K. Shakouri, W.Y. Fu, V. Robert, V. Tudor, S. Bonnet, G.F. Schneider, Contactless Spin Switch Sensing by Chemo-Electric Gating of Graphene, Advanced Materials, 32 (2020) 1903575.

[27] C. Boix-Constant, V. García-López, E. Navarro-Moratalla, M. Clemente-León, J.L. Zafra, J. Casado, F. Guinea, S. Mañas-Valero, E. Coronado, Strain Switching in van der Waals Heterostructures Triggered by a Spin-Crossover Metal–Organic Framework, Advanced Materials, 34 (2022) 2110027.

[28] N. Konstantinov, A. Tauzin, U.N. Noumbe, D. Dragoe, B. Kundys, H. Majjad, A. Brosseau, M. Lenertz, A. Singh, S. Berciaud, M.L. Boillot, B. Doudin, T. Mallah, J.F. Dayen, Electrical read-out of light-induced spin transition in thin film spin crossover/graphene heterostructures, Journal of Materials Chemistry C, 9 (2021) 2712.

[29] Gavara-Edo, M., Córdoba, R., Valverde-Muñoz, F. J., Herrero-Martín, J., Real, J. A., & Coronado, E. (2022). Electrical sensing of the thermal and light-induced spin transition in robust contactless spin-crossover/graphene hybrid devices. Adv. Mater. 34, 2202551.

[30] Gavara-Edo, M., Valverde-Muñoz, F. J., Córdoba, R., Muñoz, M. C., Herrero-Martín, J., Real, J. A., & Coronado, E. (2023). Sublimable complexes with spin switching: chemical design, processing as thin films and integration in graphene-based devices. J. Mater. Chem. C 11, 8107–8120.

[31] Torres-Cavanillas, R., Morant-Giner, M., Escorcia-Ariza, G., Dugay, J., Canet-Ferrer, J., Tatay, S., ... & Coronado, E. (2021). Spin-crossover nanoparticles anchored on MoS2 layers for heterostructures with tunable strain driven by thermal or light-induced spin switching. Nat. Chem. 13, 1101–1109.

[32] J. Villalva, A. Develioglu, N. Montenegro-Pohlhammer, R. Sanchez-de-Armas, A. Gamonal, E. Rial, M. Garcia-Hernandez, L. Ruiz-Gonzalez, J.S. Costa, C.J. Calzado, E.M. Perez, E. Burzuri, Spin-state-dependent electrical conductivity in single-walled carbon nanotubes encapsulating spin-crossover molecules, Nature Communications, 12 (2021) 1578.

[33] Sanchis-Gual, R., Coronado-Puchau, M., Mallah, T., & Coronado, E. (2023). Hybrid nanostructures based on gold nanoparticles and functional coordination polymers: Chemistry,

physics and applications in biomedicine, catalysis and magnetism. Coord. Chem. Rev. 480, 215025.

[34] I. Suleimanov, et al. "The photo-thermal plasmonic effect in spin crossover@ silica–gold nanocomposites." Chemical Communications 50 (2014): 13015-13018.

[35] K. Abdul-Kader, et al. "Synergistic switching of plasmonic resonances and molecular spin states." Nanoscale 5 (2013): 5288-5293.

[36] van der Molen, Sense Jan, and Peter Liljeroth. "Charge transport through molecular switches." Journal of Physics: Condensed Matter 22 (2010): 133001.

[37] Devid, E. J., Martinho, P. N., Kamalakar, M. V., Salitros, I., Prendergast, U., Dayen, J. F., ... & van der Molen, S. J. (2015). Spin transition in arrays of gold nanoparticles and spin crossover molecules. ACS Nano 9, 4496–4507.

[38] Usmani, S., Mikolasek, M., Gillet, A., Costa, J. S., Rigoulet, M., Chaudret, B., ... & Tricard, S. (2020). Spin crossover in Fe(triazole)–Pt nanoparticle self-assembly structured at the sub-5 nm scale. Nanoscale 12, 8180–8187.

[39] Torres-Cavanillas, R., Sanchis-Gual, R., Dugay, J., Coronado-Puchau, M., Giménez-Marqués, M., & Coronado, E. (2019). Design of bistable Gold@spin-crossover core-shell nanoparticles showing large electrical responses for the spin switching. Adv. Mater. 31, 1900039.

[40] Soroceanu, Ion, et al. "Broad-band dielectric spectroscopy reveals peak values of conductivity and permittivity switching upon spin crossover." The Journal of Physical Chemistry Letters 10.23 (2019): 7391-7396.

[41] I.y.A. Gural'skiy, C.M. Quintero, J.S. Costa, P. Demont, G. Molnar, L. Salmon, H.J. Shepherd, A. Bousseksou, Spin crossover composite materials for electrothermomechanical actuators, Journal of Materials Chemistry C, 2 (2014) 2949-2955.

[42] M. Piedrahita-Bello, J.E. Angulo-Cervera, A. Enriquez-Cabrera, G. Molnár, B. Tondu, L. Salmon, A. Bousseksou, Colossal expansion and fast motion in spin-crossover@ polymer actuators, Materials Horizons, 8 (2021) 3055-3062.

[43] Y.-C. Chen, Y. Meng, Z.-P. Ni, M.-L. Tong, Synergistic electrical bistability in a conductive spin crossover heterostructure, Journal of Materials Chemistry C, 3 (2015) 945-949.

[44] M. D. Manrique-Juarez, S. Rat, F. Mathieu, D. Saya, I. Séguy, T. Leichle, L. Nicu, L. Salmon, G. Molnar, A. Bousseksou, Microelectromechanical systems integrating molecular spin crossover actuators, Appl. Phys. Lett. 2016, 109, 061903.

[45] Manrique-Juarez, M.D.; Mathieu, F.; Shalabaeva, V.; Cacheux, J.; Rat, S.; Nicu, L.; Leïchlé, T.; Salmon, L.; Molnár, G.; Bousseksou, A., A Bistable Microelectromechanical System Actuated by Spin Crossover Molecules. Angew. Chem. Int. Ed. 2017, 56, 8074–8078.

[46] Urdampilleta, M.; Ayela, C.; Ducrot, P.H.; Rosario-Amorin, D.; Mondal, A.; Rouzières, M.; Dechambenoit, P.; Mathonière, C.; Mathieu, F.; Dufour, I.; et al. Molecule-based microelectromechanical sensors. Sci. Rep. 2018, 8, 8016.

[47] C. Lefter, R. Tan, J. Dugay, S. Tricard, G. Molnár, L. Salmon, J. Carrey, W. Nicolazzi, A. Rotaru, A. Bousseksou, Unidirectional electric field-induced spin-state switching in spin crossover based microelectronic devices, Chemical Physics Letters, 644 (2016) 138-141.

[48] X. Zhang, T. Palamarciuc, J.-F. Letard, P. Rosa, E.V. Lozada, F. Torres, L.G. Rosa, B. Doudin, P.A. Dowben, The spin state of a molecular adsorbate driven by the ferroelectric substrate polarization, Chemical Communications, 50 (2014) 2255-2257.

[49] P. Costa, G.H. Hao, A.T. N'Diaye, L. Routaboul, P. Braunstein, X. Zhang, J. Zhang, B. Doudin, A. Enders, P.A. Dowben, Perturbing the spin crossover transition activation energies in Fe(H2B(pz)(2))(2)(bipy) with zwitterionic additions, Journal of Physics-Condensed Matter, 30 (2018) 305503.

[50] P.S. Costa, G.H. Hao, A.T. N'Diaye, L. Routaboul, P. Braunstein, X. Zhang, J. Zhang, T.K. Ekanayaka, Q.Y. Shi, V. Schlegel, B. Doudin, A. Enders, P.A. Dowben, Manipulation of the molecular spin crossover transition of Fe(H2B(pz)(2))(2)(bipy) by addition of polar molecules, Journal of Physics-Condensed Matter, 32 (2020) 034001.

[51] G. Hao, A. Mosey, X. Jiang, A.J. Yost, K.R. Sapkota, G.T. Wang, X. Zhang, J. Zhang, A.T. N'Diaye, R. Cheng, X. Xu, P.A. Dowben, Nonvolatile voltage controlled molecular spin state switching, Applied Physics Letters, 114 (2019) 032901.

[52] A. Mosey, A.S. Dale, G. Hao, A. N'Diaye, P.A. Dowben, R. Cheng, Quantitative study of the energy changes in voltage-controlled spin crossover molecular thin films, The Journal of Physical Chemistry Letters, 11 (2020) 8231-8237.

[53] X. Zhang, P.S. Costa, J. Hooper, D.P. Miller, A.T. N'Diaye, S. Beniwal, X.Y. Jiang, Y.W. Yin, P. Rosa, L. Routaboul, M. Gonidec, L. Poggini, P. Braunstein, B. Doudin, X.S. Xu, A. Enders, E. Zurek, P.A. Dowben, Locking and Unlocking the Molecular Spin Crossover Transition, Advanced Materials, 29 (2017) 1702257.

[54] Yazdani, S., Collier, K., Yang, G., Phillips, J., Dale, A., Mosey, A., Grocki, S., Zhang, J., Shanahan, A.E., Cheng, R., & Dowben, P.A, Optical characterization of isothermal spin state switching in an Fe(II) spin crossover molecular and polymer ferroelectric bilayer, J. Phys. Cond. Matter. 35 (2023) 365401.

[55] Wäckerlin, C., Donati, F., Singha, A., Baltic, R., Decurtins, S., Liu, S.X., Rusponi, S. and Dreiser, J., (2018). Excited spin-state trapping in spin crossover complexes on ferroelectric substrates. J. Phys. Chem. C. 122, 8202–8208.

[56] Y. Zhang, S. E. Alavi, I. Soroceanu, D. W. Kamau, A. Rotaru, I. Séguy, L. Salmon, G. Molnár, A. Bousseksou, Electrical Sensing of Molecular Spin State Switching in a Spin Crossover Complex Using an Organic Field-Effect Transistor. Adv. Electron. Mater. 2024, 2400590 (in press).

[57] Y.-S. Koo, J.R. Galán-Mascarós, Spin Crossover Probes Confer Multistability to Organic Conducting Polymers, Advanced Materials, 2014, 26, 6785.

[58] D. Nieto-Castro, F.A. Garces-Pineda, A. Moneo-Corcuera, I. Sanchez-Molina, J.R. Galan-Mascaros, Mechanochemical Processing of Highly Conducting Organic/Inorganic Composites Exhibiting Spin Crossover-Induced Memory Effect in Their Transport Properties, Advanced Functional Materials, 31 (2021) 2102469.

[59] D. Nieto-Castro, A.W. Graf, F. Gispert-Guirado, J.R. Galán-Mascarós, Magnetic and electrical bistability in hybrid composites of conducting organic polymers with [Fe(NH2-trz)3]n[SO4]n, Journal of Materials Chemistry C, 11 (2023) 11325-11332.

[60] F. Lai, L. Getzner, A. Rotaru, G. Molnar, S. Cobo, A. Bousseksou, Drastic Enhancement of Electrical Conductivity of Metal-Organic Frameworks Displaying Spin Crossover, submitted.

[61] S. Rat, M. Piedrahita-Bello, L. Salmon, G. Molnar, P. Demont, A. Bousseksou, Coupling Mechanical and Electrical Properties in Spin Crossover Polymer Composites, Advanced Materials, 30 (2018) 1705275.

[62] Y.-S. Koo, J.R. Galán-Mascarós, Memory effect in ferroelectric polyvinylidene fluoride (PVDF) films via spin crossover probes, Dalton Trans., 2024, 53, 7590-7595.

Chapter 2. Investigation of the effect of ferroelectric polarization on the spin state of spin crossover complexes embedded in a piezopolymer matrix

Recent experiments indicate that the spin state of molecules adjacent to ferroelectric layers depends on the magnitude and direction of the polarization. Since similar effects could arise in nanocomposites, in this Chapter we describe the synthesis and characterization of samples with spin crossover particles embedded in a ferroelectric polymer. The spin transition phenomenon in the poled and non-poled composites was investigated by hot-stage optical microscopy and calorimetry, but no sizeable effect of the poling on the spin-state equilibrium was detected. Similar conclusion was reached with bilayer, ferroelectric polymer - SCO films.

2.1. Introduction

As discussed in Chapter 1.1, the molecular spin crossover (SCO) phenomenon can be conveniently induced by temperature, pressure or light irradiation [1-6] and numerous SCO complexes respond also to chemical stimuli (e.g. adsorption of guest molecules) [7]. A very intense magnetic field can also alter the spin state of the molecules [8]. On the other hand, the possible influence of electric fields remains elusive, despite the obvious technological interest of electric field control of molecular spin states. The rationale behind a possible electric field effect is that the dielectric permittivity of the material in the LS and HS states is different (Fig. 2.1) and therefore the spin state equilibrium will be altered in the presence of an intense electrical field [9].

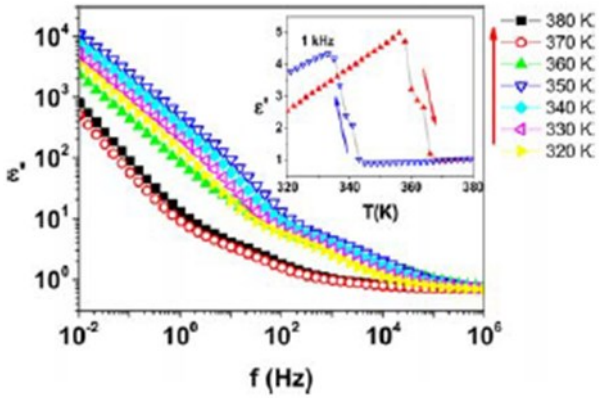

Figure 2.1. *Real part of the dielectric permittivity of 1 as a function of the frequency, measured at selected temperatures in the heating mode. The inset shows the thermal hysteresis loop of ε' recorded at 1 kHz [Fe(Htrz)$_2$(trz)](BF$_4$).*

In other words, the interaction energy between the electric field and the electric dipolar moment (permanent or induced) of the molecules depends on the spin state of the latter, leading to a shift of the transition temperature. However, one can expect a significant shift of the spin-state equilibrium and, in general, one can achieve an electrostatic contribution to the free energy comparable with typical reaction enthalpies only for very high fields [10]. Indeed, a rough estimation gives a change of energy of ~20 kJ/mol when a molecule with a dipole component

of 1 D, oriented along the field direction, is subjected to a field of 1 GV/m [11]. In practice, such extreme fields can be achieved only locally, at specifically designed interfaces. For instance, Climent et al. [12] theoretically predicted a large modification of the spin state equilibrium temperature (up to 40-50 K) of selected SCO molecules placed in plasmonic nanocavities and argued that this effect is linked to the strong coupling between the (spin state dependent) dipole moment of the molecule and the intense local electromagnetic field of the plasmonic cavity.

From an experimental point of view, at the single-molecule level, several research teams have demonstrated spin state switching by applying a voltage bias through SCO molecules by means of the tip of a scanning tunneling microscope [13-15]. On a macroscopic level, the application of high external fields (> MV/m) revealed some interesting effects (Fig 2.2) [16], but the use of such high fields remains complicated due to the potential breakdown of the material.

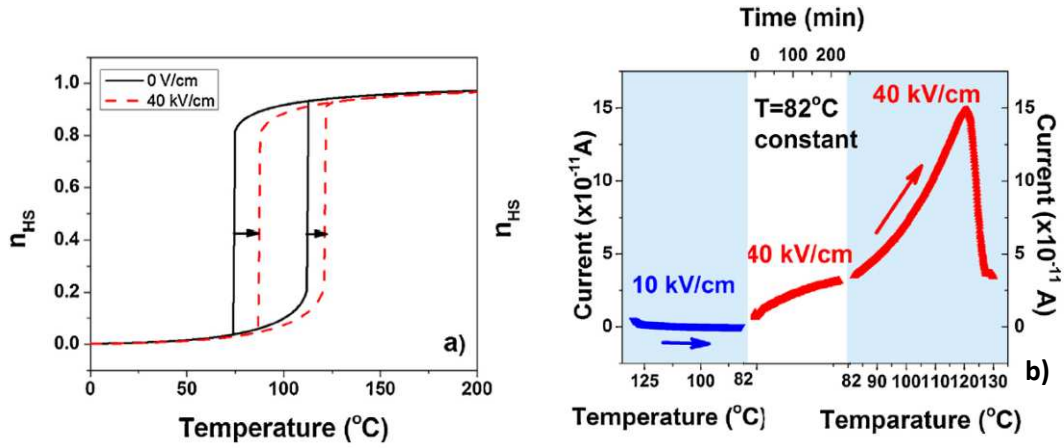

Figure 2.2. *a) Simulated temperature dependence of the HS fraction in the absence and presence of an electric field. The field-induced shift of the spin transition is indicated by the arrow. b) Electric field switch experiment performed at 82 °C. The left panel shows the current recorded when cooling the device from 130 to 82 °C under 10 kV/cm. The middle panel depicts the temporal evolution of the current at fixed temperature (82 °C) and bias (40 kV/cm) followed by a complete thermal cycle (right panel) between 82 and 130 °C [16].*

Furthermore, as discussed in Chapter 1.4.2, a considerable effect of local electrical fields on the spin state of molecules near the interface of polarized ferroelectric polymeric substrates was indicated [17-20]. Notably, Hao et al. [18] reported that both polyvinylidene fluoride hexafluoropropylene (PVDF-HFP) and croconic acid layers adjacent to the SCO complex $[Fe\{H_2B(pz)_2\}_2(bipy)]$ ($H_2B(pz)_2$ = bis(hydrido)-bis-(1H-pyrazol-1-yl)borate, bipy = 2,2'-bipyridine) appear to lock to a large extent either the HS or the LS state of the molecule, depending on the direction of the ferroelectric polarization. Further experiments by Mosey et al. [19] showed that such effects are even perceptible in relatively thick (65 nm) SCO films. Although the phenomenon remain debated [21] and the mechanisms largely uncertain, these findings suggest that intense local electric fields, generated at interfaces, could alter the spin state equilibrium.

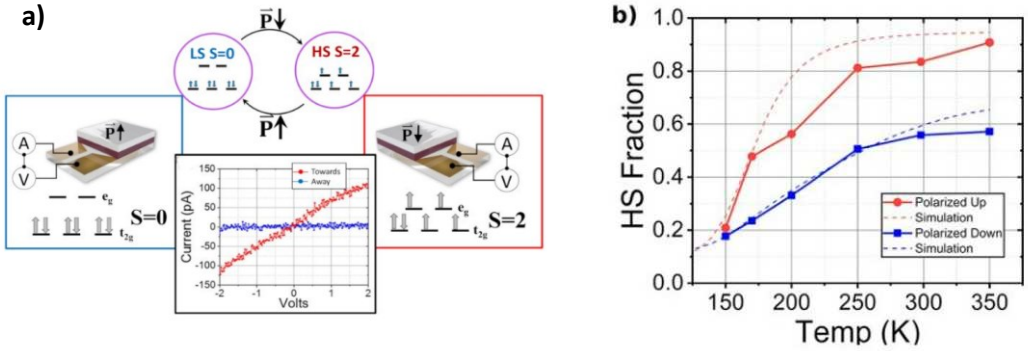

***Figure 2.3**. a) Scheme of a bilayer SCO/PVDF-HFP device with I-V curves in the two spin states. b) The effect of the polarization direction on the HS fraction of the SCO layer [18].*

In this context, a series of interesting samples were obtained recently by embedding SCO particles into piezoelectric polymers, such as P(VDF-TrFE) (poly(vinylidene fluoride-co-trifluoro-ethylene) [22-24] and PVDF (poly(vinylidene fluoride) [25]. These composites revealed remarkable electromechanical couplings, such as current discharge at the spin transition and spin-state dependent ferroelectric properties. Incidentally, Rat et al. [22] observed also a small downshift of the transition temperature in the polarized composites (vs. the nonpolarized sample). (Fig.2.4). An analogy between these SCO@piezopolymer samples and the ferroelectric/SCO multilayers appears thus, which motivated us to design dedicated experiments aiming to answer the question whether the ferroelectric polarization in the composite had an effect on the spin transition properties of the embedded particles. The results of these experiments are reported below.

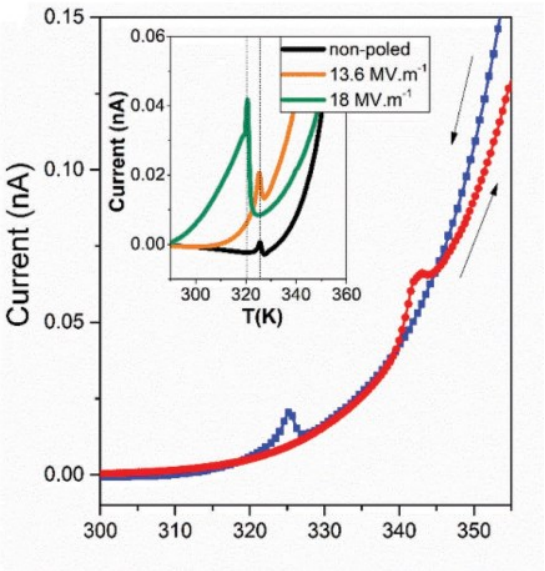

***Figure 2.4.** Electrical properties of the P(VDF-TrFE)/SCO composite. Short-circuit current under zero applied bias on heating and cooling at rates of ±2 K min^{-1}. Measurements were done after poling the sample in a 13.6 MV m^{-1} electrical field. The inset shows the modulation of the amplitude and temperature of the discharge current peak (cooling mode) controlled by the initial polarization [22].*

2.2. Sample preparation

P(VDF_{80}-$TrFE_{20}$) with a ratio of vinilydene/trifluoroethylene of 80/20 was provided by Piezotech. SCO nanoparticles of ca. 60 nm mean size and formulae $[Fe(Htrz)_2(trz)](BF_4)\cdot 0.7H_2O$ (**1**) and $[Fe(Htrz)_{2.1}(NH_2trz)_{0.1}(trz)_{0.8}](BF_4)\cdot 0.8H_2O$ (**2**) were synthesized and characterized as described by Piedrahita et al. [26]. For the synthesis of SCO@ P(VDF-TrFE) composite films, we prepared two suspensions of 80 mg of each SCO compound in 1.6 ml of butanone, in which we dissolved 240 mg of P(VDF_{80}-$TrFE_{20}$). This mixture was then blade casted on a heated (35 °C) glass substrate at 1.50 mm blade height. After drying, the resulting membranes had a thickness around 100 µm and a particle concentration of ca. 25 wt.%. The membranes were then hot pressed at 145°C at a pressure of 0.2 bar for 30 seconds.

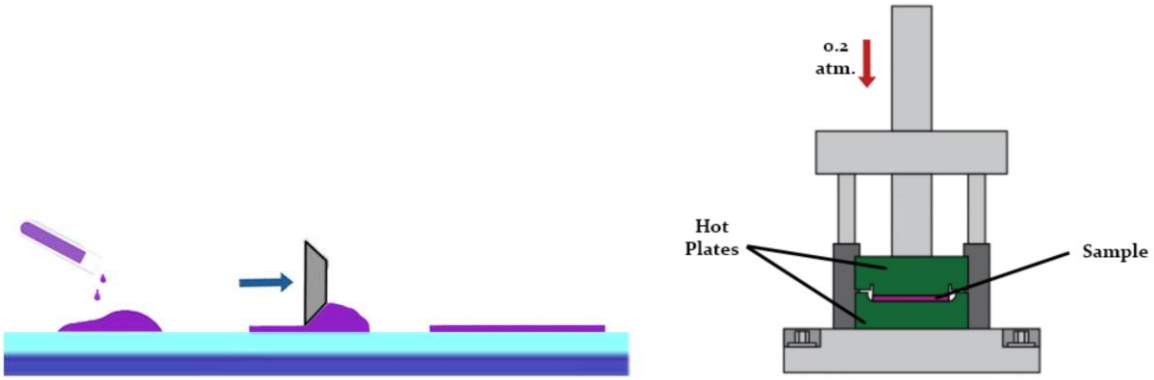

***Figure 2.5**. The schematic representation of blade casting (left) and hot pressing (right) techniques.*

The samples were finally polarized using a low frequency (200 mHz) AC voltage of 3.6 kV in amplitude, corresponding typically (depending on the sample thickness) to an electrical field of 1 MV/cm. During the poling process, the composite films were placed between two disk-shaped copper electrodes in an aluminium crucible, filled with Castor oil. The piezoelectric charge coefficient d_{33} of the poled samples was measured by means of a Piezotest PM200 instrument using the Berlincourt method at 110 Hz and 0.25 N applied force.

2.3. Analysis of poling effect on the SCO behavior in composites

In contrast to our previous works, wherein the SCO@P(VDF-TrFE) composites were made using polymers with 70-30 or 75-25 mol% monomer ratio [22-24], in the present work we opted for the copolymer with 80-20 mol%. This choice was motivated by the relatively high Curie temperature of this copolymer (T_{Curie} = 135 °C) in comparison with the previous ones. The Curie point denotes the temperature at which the ferroelectric phase is transformed into a paraelectric one, destroying thus the ferroelectric polarization. Since the SCO samples we used must be heated to relatively high temperatures (ca. 100 °C) to ensure a complete spin transition, it is important to use a copolymer with a high T_{Curie}. However, reducing the TrFE content of the copolymer involves an adverse effect, which is the reduced piezoelectric performance. To mitigate this issue, in the present work we employed a hot press (following blade casting of the composite film), which affords for an improved recrystallization of the sample, ensuring a high

concentration of the polar β phase, which displays the highest piezoelectric performance [27-28].

Figure 2.6 presents the visual differences observed in pure P(VDF_{80}-$TrFE_{20}$) samples subjected to different treatments, highlighting the relationship between opacity and β phase concentration. The casted sample appears transparent, indicating a minimal presence of the β phase and suggesting that the polymer chains are in a less ordered state. In contrast, the sample annealed at 120 °C is translucent, reflecting a partial increase of the concentration of the β phase in the polymer. The hot-pressed sample is opaque, signifying the highest concentration of the β phase in the polymer chain structure. This increase in opacity correlates with an enhanced piezoelectric response, which permits the achievement of the higher polarization yield.



Figure 2.6. *Photographs of the neat P(VDF_{80}-$TrFE_{20}$) film (from left to right): blade-casted, annealed at 120 °C and hot pressed.*

For a more quantitative analysis, the hot pressed composite samples were analyzed using differential scanning calorimetry (DSC) to observe the peaks associated with the Curie and the melting transitions. More importantly, the area under these peaks, which is proportional to the amount of the crystalline β-phase, was measured. The DSC measurements in the heating mode revealed the expected peaks related to the Curie transition in the P(VDF_{80}-$TrFE_{20}$) copolymer at 135 °C and another peak at 155 °C that represents the melting point of the polymer. In cooling, the solidification occurs around 126 °C and the Curie transition near 80 °C. In the first heating cycle the integrated area of the Curie and melting peaks was 50 J/g, from which a crystallinity of ca. 48 % can be inferred, using the approach reported in ref. [27]. Note that the temperature we chosen for the hot pressing (145 °C) falls just in between the Curie and melting temperatures, which was shown in previous works as the optimum temperature to ensure the highest possible β phase content (see for example ref. [28]).

In the next step, the composites **1**@P(VDF_{80}-$TrFE_{20}$) and **2**@P(VDF_{80}-$TrFE_{20}$) (both 25 wt. %) were poled in an AC field resulting in d_{33} piezoelectric coefficients of -6 pC/N and -9 pC/N, respectively. Not surprisingly, these values are inferior to what we could obtain for the pure P(VDF_{80}-$TrFE_{20}$) copolymer processed in the same conditions (ca. -20 pC/N), but remain

very substantial for such high particle loads [22-24], confirming thus the efficiency of our sample processing protocol. The poled films were attached via a thermally conductive tape to a thin silicon substrate to ensure a homogeneous temperature distribution and were submitted to a heating-cooling cycle around the spin transition region at a rate of 1 °C/min. Importantly, sample heating was limited to 120 °C to reach completeness of the spin transition, while avoiding the depolarization of the polymer that occurs around 136 °C. During the thermal cycle color photographs of the films were acquired covering both polarized and non-polarized regions of the samples (see Figures 2.7a-2.7b). These variable temperature (white light) optical reflectance measurements on the films were conducted using a Motic SMZ168 stereomicroscope equipped with a color camera (Moticam 2) and a heating stage (Linkam Scientific THMS600).

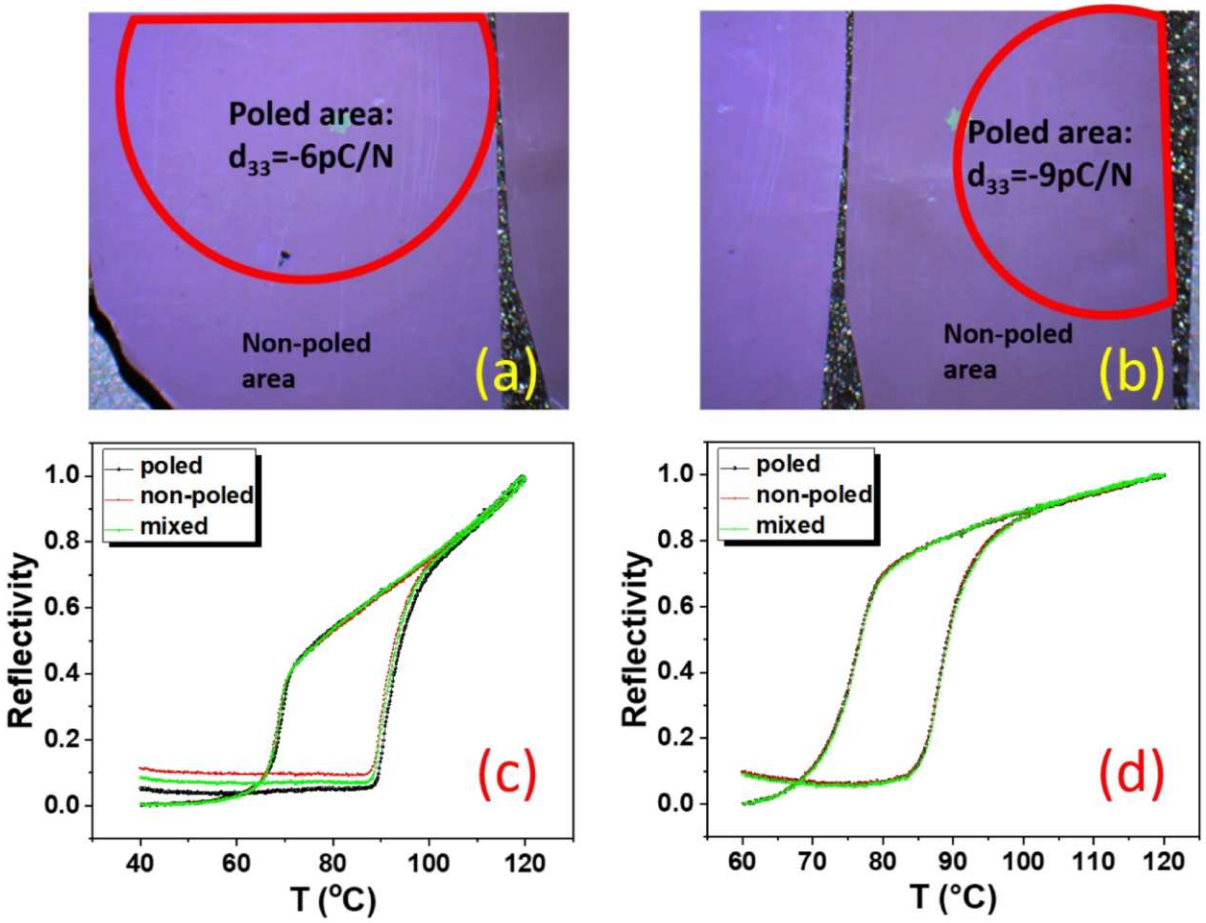

Figure 2.7. *(a-b) Selected room temperature optical images of the composites (a)* ***1****@P(VDF$_{80}$-TrFE$_{20}$) and (b)* ***2****@P(VDF$_{80}$-TrFE$_{20}$) showing the polarized regions by a red line. Note that the color recorded by the camera differs from that perceptible by the naked eye due to the color balance settings. (c-d) Variable temperature optical reflectivity (normalized to the highest temperature) of the composites (c)* ***1****@P(VDF$_{80}$-TrFE$_{20}$) and (d)* ***2****@P(VDF$_{80}$-TrFE$_{20}$) integrated for the poled (black) and non-poled (red) regions, as well as for the entire image (green).*

The key experimental observation is the fact that in none of the images (before, after and during the spin transition) we could observe a color contrast between the poled and non-

poled regions, indicating comparable SCO behaviors. This finding is visualized in Figures 2.7c-2.7d showing that the thermal SCO curves recorded simultaneously for the polarized and non-polarized areas are virtually identical for both samples. In other words, the ferroelectric polarization does not lead to any appreciable change of the spin state equilibrium in these composite samples.

At this stage, we shall discuss the link between the directions of the ferroelectric polarization (perpendicular to the sample plane) and that of the dipole moments of the SCO complexes in our samples. Indeed, we have purposefully used in these experiments small (ca. 60 nm) isomorphic SCO particles, which afford for isotropic composites with a random particle distribution – contrary to high aspect ratio particles, which tend to give rise to specific particle orientations [29]. Obviously, using randomly oriented particles does not allow us to maximize the interaction with the ferroelectric polarization, but most importantly it ensures that a significant proportion of the particles is oriented such a way that the local dipole moments are aligned with the polarization direction in any case.

To further analyze the potential effects of the ferroelectric polarization on the spin-state equilibrium, we performed a series of DSC analysis on the composite **1**@P(VDF_{80}-$TrFE_{20}$). DSC thermograms were acquired using a Netzsch DSC 3500 Syrius instrument with a heating/cooling ramp of ±10 °C/min and a nitrogen gas purge of 20 mL/min. Temperature and enthalpy were calibrated using the melting transition of indium. For DSC experiments we used two samples, one from the previous optical reflectivity experiment (denoted **1A**) and another one, which could be poled to reach a d_{33} value of -9 pC/N (denoted **1B**). In comparison with the optical reflectivity measurements, the disadvantage of calorimetry is that the poled and non-poled sample regions cannot be analyzed simultaneously. For this reason, altogether four samples were investigated: **1A** and **1B**, both poled and non-poled. On the other hand, the DSC technique provides also several advantages, notably, it allows us to control in-situ if the Curie transition is reached (partially or totally) during the thermal cycles. To better explore this aspect, we measured in our DSC multiple temperature cycles, each starting at 20 °C and ending at different temperatures (see Figure 2.8 for an example). In the first cycle, the final temperature was set to 100 °C and then it was increased by steps of 10°C to reach 160 °C (i.e. above the melting point of the matrix). Each cycle was repeated twice and the data reported below corresponds to the second run.

Figure 2.9 summarizes the DSC data obtained for the different composite samples. Surprisingly, we observed that the spin transition temperature of each sample decreases when heated to higher temperatures. This phenomenon is, however, an intrinsic property of the neat SCO particles, which display a similar behavior when analyzed in the same experimental conditions (see Figure 2.10). This decrease of the spin transition temperature is reversible: when the sample is left in ambient air for a month and re-analyzed subsequently by DSC, a very similar curve is obtained, which signifies that the sample recovered to a large extent its initial SCO properties upon storage.

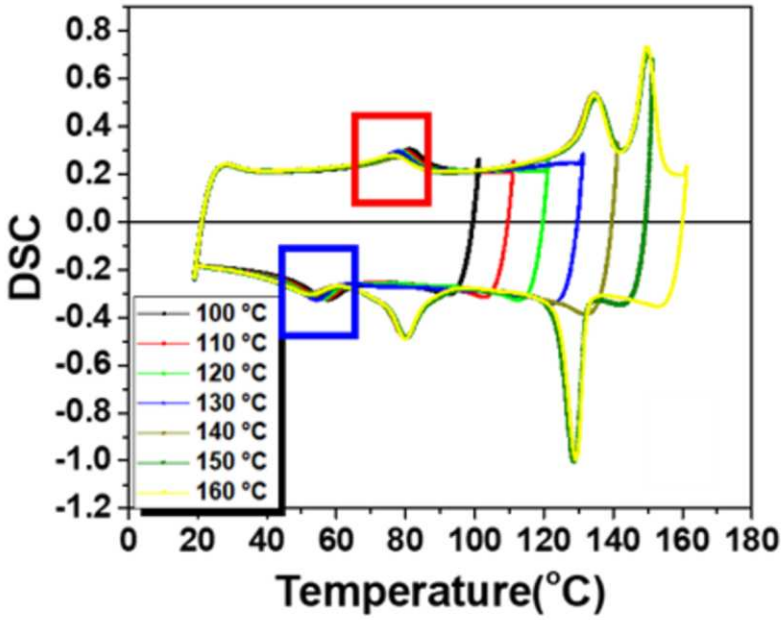

Figure 2.8. *DSC measurements on sample* ***1A****^{poled}* *through multiple thermal cycles, with identical starting temperatures (20 °C) and increasing end temperatures (from 100 to 160 °C).*

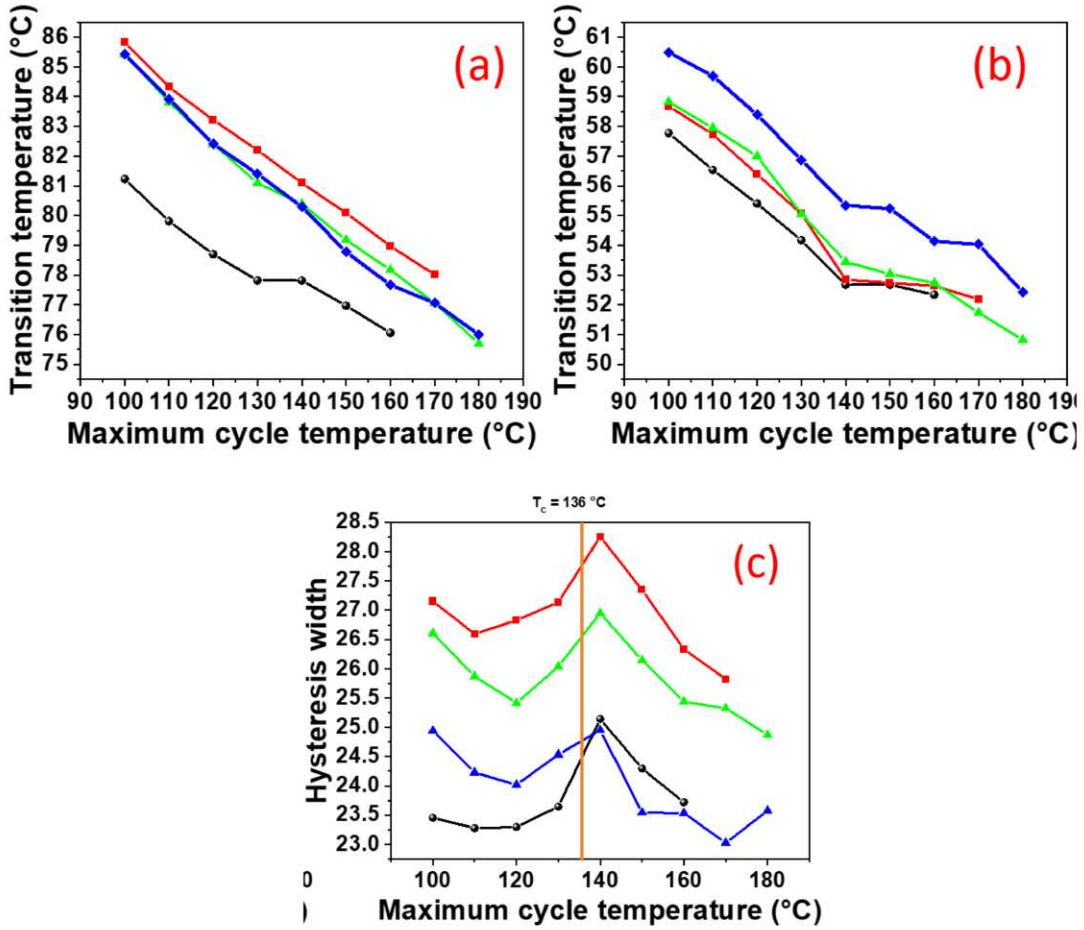

Figure 2.9. *Spin transition temperatures in the heating (a) and cooling (b) modes as well as the associated width of the hysteresis (c) as a function of the 'highest heating temperature' for samples* ***1A****^{poled}* *(black),* ***1A****$^{non\text{-}poled}$* *(red),* ***1B****^{poled}* *(green) and* ***1B****$^{non\text{-}poled}$* *(blue).*

Based on this observation we can suggest that heating of the particles leads to a progressive loss of their water content and, as a result, to a progressive change of their SCO behavior. Then, in ambient conditions the sample reabsorbs water molecules and regains (roughly) its initial SCO properties. Although this phenomenon complicates the analysis of the DSC data obtained for the composite samples, we can extract several interesting information. The poled and non-poled samples display slightly different transitions temperatures, although the differences remain small (< 5 °C), in particular for sample **1B**, which displays higher polarization. However, if the differences were the result of the polarization of the polymer, we expect they disappear after heating above 140 °C, because the Curie temperature will be surpassed and the polarization of the polymer will be destroyed. This is clearly not the case in our experiments, wherein the transition temperatures change in a similar (parallel) manner both below and above the Curie temperature. In agreement with the optical microscopy observations, we can conclude therefore that the ferroelectric polarization has no considerable impact on the spin transition behavior of the samples.

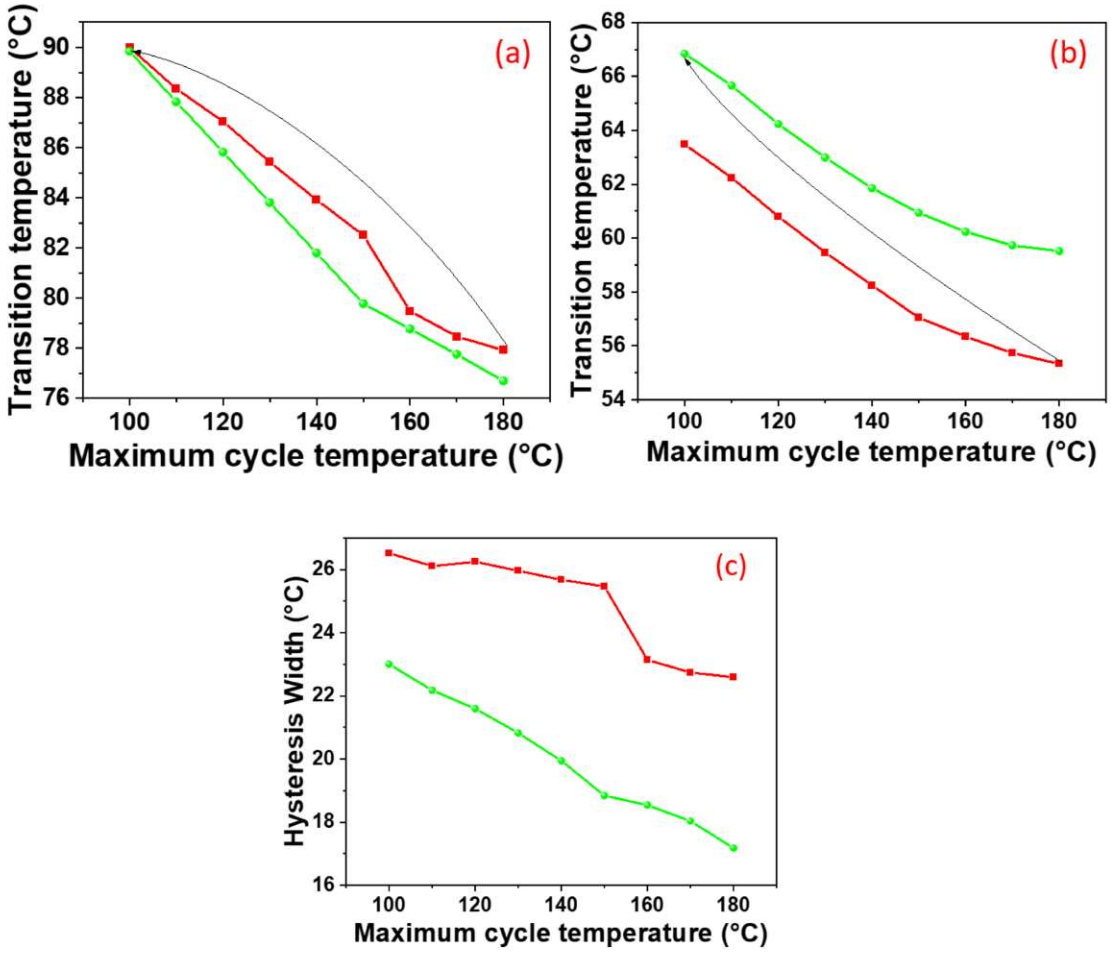

Figure 2.10. *Spin transition temperatures in the heating (a) and cooling (b) modes as well as the associated width of the hysteresis (c) as a function of the 'highest heating temperature' for the neat powder sample **1**. Two series of experiments are shown: a first experiment (in red) and a second experiment (in green) conducted on the same DSC sample pan following one month storage in ambient air.*

Another interesting observation is the occurrence of a maximum of the hysteresis width when the samples are annealed at 140 °C (Figure 2.9 c). This finding is not related to the polarization of the polymer matrix, since we observe it also in the non-polarized samples, neither to the intrinsic properties of the bulk material, since we do not observe it in the neat powder sample (Figure 2.10 c). We can thus suggest that this phenomenon is related to a partial recrystallization of the P(VDF_{80}-$TrFE_{20}$) polymer into its β phase, which is the most efficient at this temperature. This subtle influence of the degree of crystallinity on the SCO phenomenon might be linked to different mechanical and/or interfacial properties.

2.4. Analysis of poling effect on the SCO behavior in films deposited on a ferroelectric substrate

The above discussed configuration of the SCO material in the form of nanoparticles embedded in a ferroelectric matrix in a 3-3 connectivity mode showed negligible effect of the ferroelectric polarization on the spin transition. However, one should keep in mind that in those composites the SCO particles display a more or less random orientation, which potentially reduces the effect of the field. For this reason, we have also conducted a series of experiments with a bilayer structure (i.e. a 2-2 connectivity composite), consisting of a ferroelectric P(VDF_{80}-$TrFE_{20}$) substrate covered with a nanometric thickness, crystallographically oriented SCO film. This approach is different from the previous one because of the possibility of controlling the direction of polarization with respect the crystallographic direction of the spin crossover layer.

In order to fabricate a polymer film for polarization, 240 mg of P(VDF_{80}-$TrFE_{20}$) was diluted in 1.6 ml of MEK and casted at 1.50 mm blade height. The film was then annealed at 140 °C for 10 minutes to achieve the highest possible crystallinity. In the next step, the film was polarized for 5 minutes in AC mode at a frequency of 200 mHz and an amplitude of 3000 V. Taking into account of the thickness of the piezopolymer layer (ca. 80 μm) it gives an applied electrical field of 37.5 kV/m. The poled area was marked and the values of piezoelectric coefficient was checked inside the polarized region (Fig. 2.11) using a piezometer. The measured value of d_{33} coefficient was -20 pC/N, which is a high value for the P(VDF_{80}-$TrFE_{20}$) copolymer.

The polymer film was divided in four pieces, so each of them had poled and non-poled areas. The samples were grouped in two equivalent pairs with one film with polarization upwards (Up) and downwards (Down). Both layers were positioned on fused silica supports as presented in Figure 2.11. The SCO complex $Fe(HB(tz)_3)_2$ (tz = 1,2,4-triazol-1-yl) was deposited on top of the samples using a vacuum thermal evaporation technique. For this specific experiment we deposited films with two thicknesses (50 and 100 nm). As described in previous publications of the team [30-31], the as-deposited films of these compounds are amorphous, but can be very efficiently recrystallized using a water vapor annealing technique. Importantly, the recrystallization is done at room temperature and therefore the ferroelectric polarization of the substrate is maintained. After recrystallization the films become fully crystalline and oriented with the orthorhombic c-axis normal to the substrate plane. Importantly, the

recrystallized films display an extremely well reproducible spin transition near 62°C during several millions of thermal cycles [31]. These two features make them ideal for the aim of our investigation.

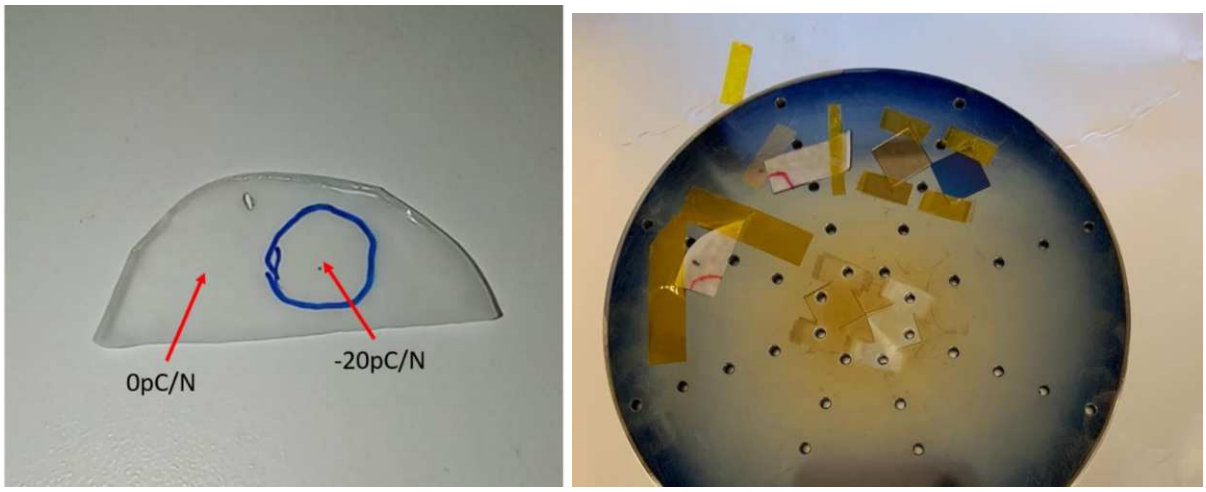

***Figure 2.11**. Left panel: Photograph of the P(VDF$_{80}$-TrFE$_{20}$) substrate with the poled area in the middle marked by the blue circle. The piezoelectric coefficient is d_{33}=-20 pC/N within this region. Right panel: Deposition of Fe(HB(tz)$_3$)$_2$ on P(VDF$_{80}$-TrFE$_{20}$) polymer substrates. The edges of the polymer are marked with red marker to distinguish the poled areas for further measurements.*

Following the deposition of the SCO films on the polymer surface, we conducted UV light transmission measurements during two temperature cycles, ranging from 25 to 100 °C with a heating/cooling rate of ±2 °C/min. The sample was illuminated using a LED light source (310 nm) through a 5x magnification microscope objective. This wavelength was chosen because the sample is known to exhibit an intense absorption band at this wavelength in the LS state, which is completely bleached in the HS state [30]. The transmitted light image sequence of the interest region was recorded by a CCD camera (Andor Technology, Clara). The sample temperature was controlled by a Linkam Scientific T95 controller, associated with a Peltier Module for high heating/cooling rate precision. After the measurements the analysis of the images was done using the ImageJ software to obtain the values of transmitted light intensity as a function of time for each pixel of the camera. Synchronization of the light intensity and the temperature over time permits to analyze the direct temperature dependence. To enhance precision in characterizing the spin transitions, we plotted the temperature derivative of the transmitted light intensity as a function of the temperature. These results are displayed in Figure 2.12 for both the 50 nm (top panel) and 100 nm (bottom panel) films. In each figure we compare four different situations: UP and DOWN polarizations, as well as the non-poled regions for both orientations of the films. Despite the strong polarization of the polymer and the high measured piezoelectric coefficient (-20 pC/N), the spin transition temperatures of the SCO film exhibited minimal variation across measurements, without any discernible trend related to the polarization effect. One should note, however, that the accuracy of this method is limited by the fact that the measurements were not conducted simultaneously on the different samples,

which gives a possibility that the measured transition temperatures are potentially influenced by subtle differences in the thermalization conditions of the different samples.

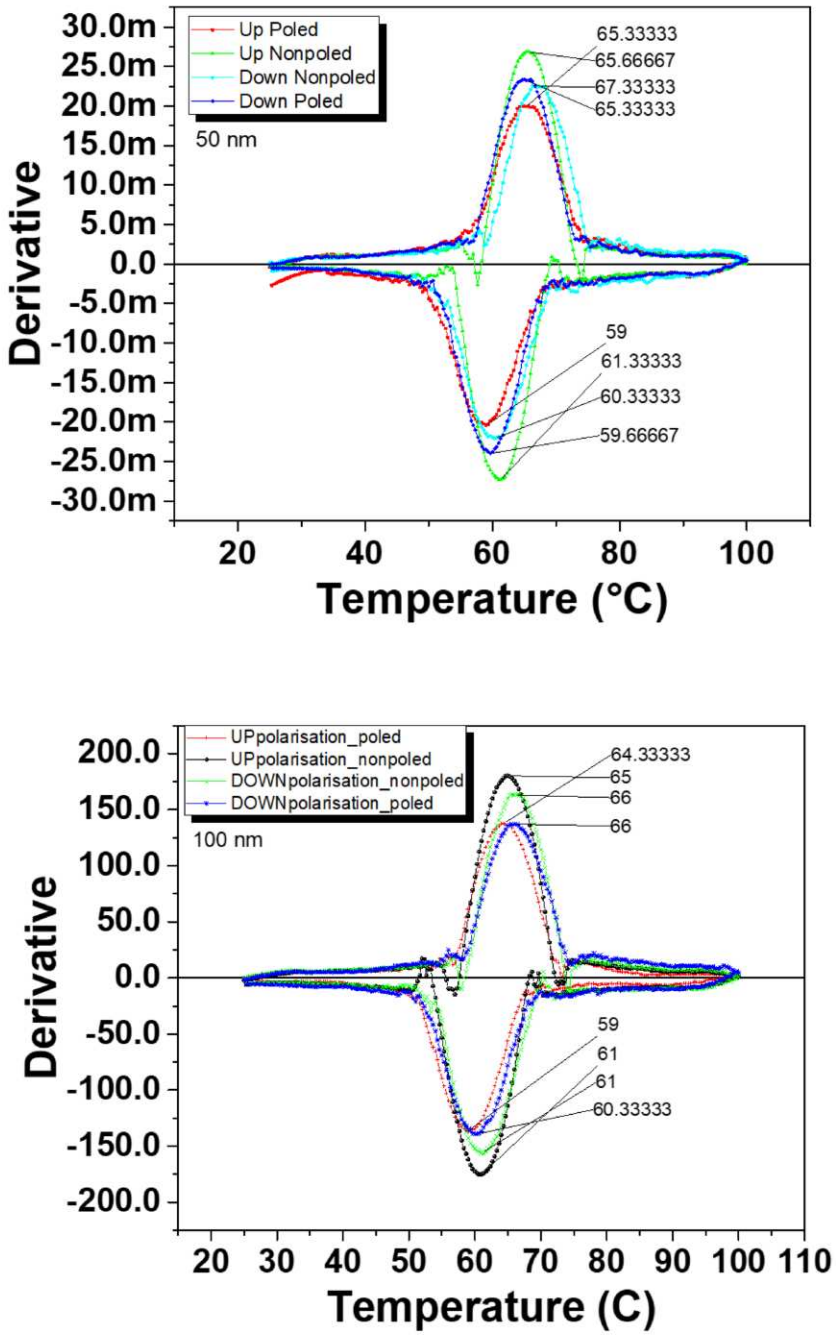

***Figure 2.12**. Temperature derivatives of the transmitted UV light intensity as a function of the temperature for $Fe(HB(tz)_3)_2$ films deposited on UP-polarized, DOWN-polarized and NON-polarized areas of a P(VDF-TrFE) ferroelectric substrate. The poled areas displayed a d_{33} piezoelectric charge coefficient of -20 pC/N. Top panel: 50 nm SCO film, bottom panel: 100 nm SCO film. The peak values, corresponding to the spin transition temperatures, are marked for each sample. Positive and negative peaks correspond to heating and cooling, respectively.*

2.5. Conclusions

No sizeable effect of the ferroelectric polarization of the P(VDF_{80}-$TrFE_{20}$) matrix on the spin crossover properties of embedded Fe(II)-triazole particles could be observed, despite a relatively high degree of polarization, attested by a piezoelectric charge coefficient of -9 pC/N. Similar conclusion can be drawn for the bilayer 2-2 connectivity samples made with [$Fe((HB(tz)_3)_2$] films deposited on top of poled and non-poled P(VDF_{80}-$TrFE_{20}$) substrates. We would like to underline that these results do not contradict the observations made by the Dowben team for SCO/ferroelectric bilayer systems (see Chapter 1.4.2), which were obtained for different compounds and for different sample geometries. However the present results show that their findings may not be completely general and depend on the exact experimental parameters used, whose role remains to be better elucidated. Further work is thus necessary to address the effect of strong local electric fields on the spin-state equilibrium using on-purpose designed nanostructures, such as plasmonic nanocavities.

Although it was not the central aim of the work, the experiments discussed in this Chapter 2 revealed a small, but distinct influence of the degree of crystallinity of the polymer on the width of the hysteresis associated with the thermal spin transition. Incidentally, a considerable sensitivity of the spin transition on the thermal annealing conditions was also uncovered and, tentatively, linked to the dehydration of the samples.

References

[1] Gütlich P., Hauser A., & Spiering H., Angew. Chem. Int. Ed. 33.20 (1994) 2024-2054

[2] M. A. Halcrow (ed.), „Spin crossover materials: properties and applications", J. Wiley & Sons, (2013).

[3] Gütlich P., Goodwin H.A., „Spin Crossover in Transition Metal Compounds III", Top. Curr. Chem (2004), vols 233-235.

[4] Nicolazzi, W., & Bousseksou, A., C.R. Chimie 21 (2018) 1060-1074.

[5] Gaspar, A. B., Molnár, G., Rotaru, A., & Shepherd, H. J., C.R. Chimie 21 (2018) 1095-1120.

[6] Chastanet, G., Lorenc, M., Bertoni, R., & Desplanches, C.R. Chimie 21 (2018) 1075-1094.

[7] Resines-Urien, E., Fernandez-Bartolome, E., Martinez-Martinez, A., Gamonal, A., Piñeiro-López, L., & Costa, J. S. Chem. Soc. Rev. 52 (2023) 705-727.

[8] Bousseksou, A., Boukheddaden, K., Goiran, M., Consejo, C., Boillot, M.-L., & Tuchagues, J.-P. , Phys Rev. B 65 (2002) 172412.

[9] Bousseksou, A., Molnár, G., Demont, P., & Menegotto, J., J. Mater. Chem. 13 (2003) 2069-2071.

[10] Kreuzer, H. J., Surf. Interface Anal. 36 (2004) 372-379.

[11] Shaik, S., Danovich, D., Joy, J., Wang, Z., Stuyver, T., J. Am. Chem. Soc. 142 (2020) 12551–12562.

[12] Climent, C., Galego, J., Garcia-Vidal, F. J., & Feist, J., Angew. Chem. Int. Ed. 58 (2019) 8698-8702.

[13] Miyamachi, T., Gruber, M., Davesne, V., Bowen, M., Boukari, S., Joly, L., Scheurer, F., Rogez, G., Yamada, T.K., Ohresser, P., & Beaurepaire, E., Nat. Commun. 3 (2012) 938.

[14] Jasper-Toennies, T., Gruber, M., Karan, S., Jacob, H., Tuczek, F., & Berndt, R., Nano Lett. 17 (2017) 6613-6619.

[15] Tong, Y., Kelaï, M., Bairagi, K., Repain, V., Lagoute, J., Girard, Y., Rousset, S., Boillot, M.L., Mallah, T., Enachescu, C., & Bellec, A., J. Phys. Chem. Lett. 12 (2021) 11029-11034.

[16] Lefter, C., Tan, R., Dugay, J., Tricard, S., Molnár, G., Salmon, L., Carrey, J., Nicolazzi, W., Rotaru, A., & Bousseksou, A., Chem. Phys. Lett. 644 (2016) 138-141.

[17] Zhang, X., Palamarciuc, T., Létard, J.F., Rosa, P., Lozada, E.V., Torres, F., Rosa, L.G., Doudin, B., & Dowben, P.A., Chem Commun. 50 (2014) 2255-2257.

[18] Hao, G., Mosey, A., Jiang, X., Yost, A.J., Sapkota, K.R., Wang, G.T., Zhang, X., Zhang, J., N'Diaye, A.T., Cheng, R., & Xu, X., Appl. Phys. Lett. 114 (2019) 032901.

[19] Mosey, A., Dale, A.S., Hao, G., N'Diaye, A., Dowben, P.A., & Cheng, R., J. Phys Chem. Lett. 11 (2020) 8231-8237.

[20] Yazdani, S., Collier, K., Yang, G., Phillips, J., Dale, A., Mosey, A., Grocki, S., Zhang, J., Shanahan, A.E., Cheng, R., & Dowben, P.A, J. Phys. Cond. Matter. 35 (2023) 365401.

[21] Wäckerlin, C., Donati, F., Singha, A., Baltic, R., Decurtins, S., Liu, S.X., Rusponi, S., & Dreiser, J., J. Phys. Chem. C 122 (2018) 8202-8208.

[22] Rat, S., Piedrahita-Bello, M., Salmon, L., Molnár, G., Demont, P., & Bousseksou, A., Adv. Mater. 30 (2018) 1705275.

[23] Piedrahita-Bello, M., Martin, B., Salmon, L., Molnár, G., Demont, P., & Bousseksou, A, J. Mater. Chem. C 8 (2020) 6042-6051.

[24] Angulo-Cervera, J.E., Piedrahita-Bello, M., Martin, B., Dantras, E., Nicu, L., Leichle, T., Dalla Francesca, K., Da Costa, A., Ferri, A., Desfeux, R., & Salmon, L., J. Mater. Chem. C 10 (2022) 8466-8476.

[25] Koo, Y.S., & Galan-Mascaros, J.R.,Dalton Trans. 53 (2024) 7590-7595.

[26] Piedrahita-Bello, M., Ridier, K., Mikolasek, M., Molnár, G., Nicolazzi, W., Salmon, L., & Bousseksou, A., Chem. Commun. 55 (2019) 4769-4772.

[27] Teyssèdre, G., & Lacabanne, C., Ferroelectrics 171 (1995) 125-144.

[28] Martins, P., Lopes, A.C., & Lanceros-Mendez, S., Prog. Polym. Sci. 39 (2014) 683-706.

[29] Alavi, S. E., Martin, B., Zan, Y., Yang, X., Piedrahita-Bello, M., Nicolazzi, W., ... & Bousseksou, A. (2023). Dynamical Mechanical Analysis and Micromechanics Simulations of Spin-Crossover@ Polymer Particulate Composites: Toward Soft Actuator Devices. Chemistry of Materials, 35(8), 3276-3289.

[30] Shalabaeva, V., Rat, S., Manrique-Juarez, M. D., Bas, A. C., Vendier, L., Salmon, L., ... & Bousseksou, A. (2017). Vacuum deposition of high-quality thin films displaying spin transition near room temperature. Journal of Materials Chemistry C, 5(18), 4419-4425.

[31] Ridier, K., Bas, A. C., Zhang, Y., Routaboul, L., Salmon, L., Molnár, G., ... & Bousseksou, A. (2020). Unprecedented switching endurance affords for high-resolution surface temperature mapping using a spin-crossover film. Nature communications, 11(1), 3611.

Chapter 3. Electrospinning of spin crossover polymer nanofibers

In this chapter we explore electrospinning of spin crossover (SCO) composite nanofibers. In particular, we focus on electrospun poly(vinylidene fluoride-co-trifluoroethylene), P(VDF-TrFE), fibers, which are known to exhibit appealing piezoelectric properties [1]. We describe first the fabrication and properties of nanofibers made from polyvinylpyrrolidone (PVP) combined with $[Fe(NH_2\text{-}trz)_3]SO_4$ or $[Fe(Htrz)_2(trz)]BF_4$ SCO particles, followed by that of P(VDF-TrFE) and $[Fe(Htrz)(Atrz)(trz)]BF_4$ composite nanofibers, each characterized by scanning electron microscopy (SEM) and magnetic measurements. The dielectric properties of the P(VDF-TrFE) composites, which are crucial for their targeted applications, were further investigated by impedance spectroscopy measurements. The complex permittivity data was analyzed using the Havriliak-Negami model [2], which provided a detailed insight into the dielectric and charge transport properties of the composites.

3.1. Introduction

Electrospinning is a versatile technique that allows for the fabrication of polymer fibers, but also for the production of fibrous nanocomposites via the combination of polymers with nanoparticles. This simple technique uses the electric force to draw electrically charged threads of polymer solutions or polymer melts into long and continuous fibers with diameters ranging from a few nanometers up to a few micrometers. The process is fast, versatile, cheap, and allows for various useful properties, such as high surface-to-volume ratio, controlled porosity and enhanced elastic properties [3-7].

In the case of electrospun P(VDF-TrFE) nanofibers, an additional advantage is that the electrospinning process yields fibers with highly aligned dipoles and thus good piezoelectric properties, without the need for further electrical poling [1]. This contrasts with the case of blade-casted P(VDF-TrFE) and SCO@P(VDF-TrFE) films, discussed in Chapter 2, which must be poled after casting the film. Blade casting piezopolymers thus allow for a polarization in the direction perpendicular to the film surface only. Conversely, the electrospinning approach makes it possible to obtain films poled in the plane of the film, provided the electrospun fibers can be aligned by some means. This asset opens up interesting engineering possibilities. For example, in the blade-casted SCO@P(VDF-TrFE) composites, rod-shaped SCO particles will be always aligned perpendicular to the poling direction, but in the electrospun composites co-alignment between the particle long axis and the ferroelectric polarization becomes possible.

The literature on electrospun P(VDF-TrFE) nanofibers, their electromechanical properties and related applications is fairly extensive (see for example refs. [1, 7-9]). On the other hand, to our best knowledge, only three studies have been reported about the incorporation of SCO complexes into electrospun polymer fibers [10-12]. This contrasts with the broad literature on various processing methods of SCO compounds within polymer matrices [13-14].

The first study was published by Echeverria et al. [10], who electrospun composite fibers with diameters between 2 - 4 μm, using a solution of polystyrene (PS) and the SCO complex $[Fe(4\text{-octadecyl-}1,2,4\text{-triazole})_3(ClO_4)_2]$. They could charge the composite fibers up to 13.5 wt.% SCO concentration, but the fibers with the highest load displayed many

irregularities (Fig. 3.1), which was attributed to the reduced viscosity of the solutions with increasing SCO concentration. Interestingly, the authors have even attempted electrospinning the pure SCO material (without any polymer), but to no avail.

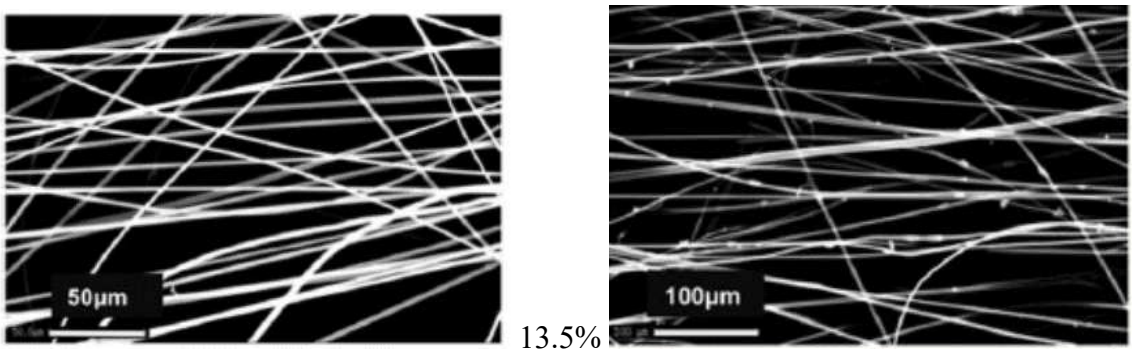

Figure 3.1. *SEM images of SCO@PS composite nanofibers with 5 and 13.5 % load [10].*

A considerable drawback of using a solution of the SCO complex in the electrospinning process is that the resulting composite material displays a modified, rather gradual SCO behavior when compared to the bulk SCO material. This can be avoided by using a suspension of SCO particles, which was first done by Dreyer et al. [11], who incorporated $[Fe(Htrz)_2(trz)]BF_4$ nanoparticles into polylactic acid (PLA) fibers via an electrospinning procedure. The authors used Mössbauer spectroscopy to show that the spin crossover behavior of the SCO compound was maintained in the polymer fibers. Later, the same group of authors incorporated two different Fe(II)-aminotriazole complexes into two different polymethylmethacrylate (PMMA) fiber structures, using either uniaxial or coaxial electrospinning (see Fig. 3.2) [12]. In both cases, the magnetic measurements showed only minor differences between the SCO properties of the composites and the bulk SCO materials, showing the effectiveness of the method. On the other hand, they found an important difference in terms of the morphology of the composites: the SCO particles were segregated in the uniaxial fibers, whereas they were relatively well dispersed within the co-axial ones. It was suggested that the coaxial fibers could be used as optical fiber waveguides, wherein the SCO compound would serve to modulate the light intensity output from the waveguide.

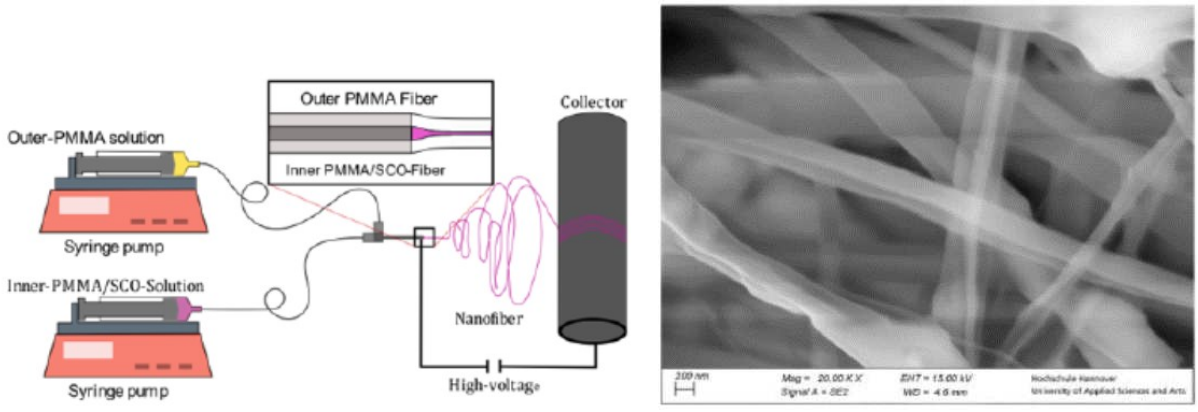

Figure 3.2. *Schematic representation of the coaxial electrospinning process and SEM image of the coaxial spun SCO@PMMA (25 wt.%) composite nanofibers [12].*

3.2. Electrospinning fabrication method

Several electrospinning methods can be used to produce the nanocomposite fibers: single-nozzle electrospinning, coaxial electrospinning and multi-jet electrospinning, which allow fabricating nanofibers with different morphologies. For our study, the single-nozzle electrospinning method was used. Nanocomposite fibers were fabricated using a Spinbox instrument supplied by the company Bioinicia. The instrument consisted of a syringe needle connected to a high-voltage power supply, a syringe filled with the solution, a syringe pump, and a grounded collector (Fig. 3.3). By applying a high voltage to the syringe needle, an electrostatic field is generated between the needle and the collector. The electrostatic forces cause the charged solution jet to be expelled and accelerated toward the collector. During this process, the solvent evaporates as the charged jet passes through the electrostatic field, resulting in the deposition of dried fibers on the collector. Electrospinning is a complex process wherein different parameters must be optimized in order to obtain fibers with the desired diameter, length and quality. The latter can be qualified by the smoothness of the surface and the apparition of defects, in particular the presence of globules. Among the key parameters one can distinguish solution parameters (solvent type, molecular weight and concentration of the polymer), processing parameters (needle tip diameter, applied voltage, tip – collector distance, flow rate, collector geometry) and environmental parameters (temperature and humidity). One of the most important parameter is the viscosity of the solution, which is adjusted in most cases by changing the polymer concentration. A higher viscosity results in general in higher fiber diameter, whereas a higher voltage leads to the opposite effect [3].

In our case, all solutions were electrospun at room temperature (ca. 22 °C) in ambient humidity (ca. 45 %), using the following spinning parameters: an applied voltage of 15 kV, a distance of 10 cm between the collector and needle, and a solution feed rate of 0.5 µl/min. The dried electrospun composites were collected on thin support sheets as randomly oriented fiber mats and later cut into small pieces, according to the requirements of specific analytical techniques. For SEM analysis, the samples were coated with a 5 nm layer of silver to enhance conductivity and image quality.

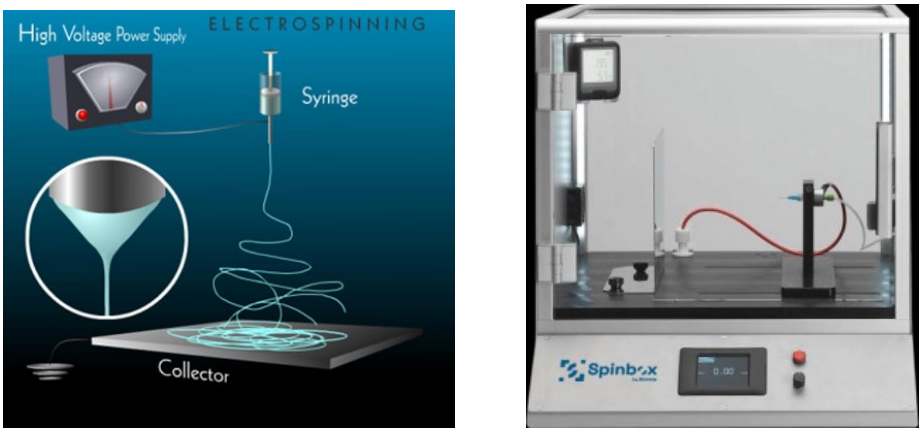

Figure 3.3. *Schematic representation of the electrospinning process and photograph of the Spinbox instrument.*

3.3. Fabrication and characterization of SCO@PVP nanofibers

For the first electrospinning tests, we used PVP, which is a very well characterized material for electrospinning [15] and, most importantly, for which we had already optimized recipes with our instrument. This allowed us to avoid fastidious optimization of electrospinning parameters.

Polyvinylpyrrolidone (PVP, M 500,000) and ethanol were purchased from Sigma-Aldrich and used without further purification. Spin-crossover nanoparticle powders of $[Fe(NH_2\text{-}trz)_3SO_4]$ (**1**) and $[Fe(Htrz)_2(trz)]BF_4$ (**2**) were synthesized by Alejandro Enriquez at LCC-CNRS using the methods described in refs. [16-17]. The SCO solutions were prepared using the following procedure: Initially, 40 mg of pre-formed spin-crossover powder was dispersed in 2 ml of ethanol using an ultrasound bath for approximately 30 minutes. Then, PVP and ethanol were added to achieve SCO ratios of 1:10, 1:20, and 1:50, and a PVP concentration of 25% by weight in ethanol for all prepared solutions. The component mixture was then homogenized using a magnetic stirrer for 2 hours at room temperature, ensuring a well-dispersed and homogeneous solution before the electrospinning procedure. The SEM images in Figure 3.4 illustrate the morphology of electrospun SCO@PVP fibers for the two compositions at two different particle concentrations.

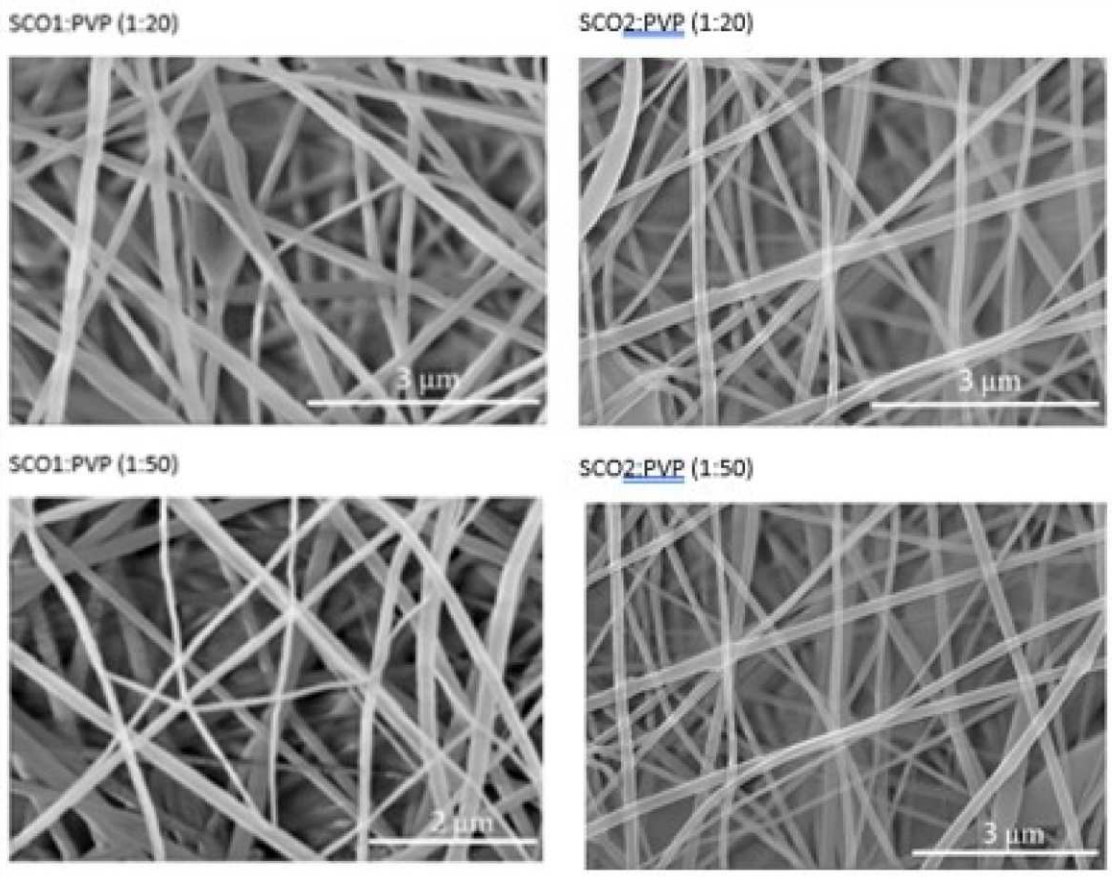

Figure 3.4. *Representative SEM images for the composite nanofibers **1**@PVP (left panel) and **2**@PVP (right panel) with different concentrations of SCO particles (5 wt.% and 2 wt.%).*

The fibers appear to have a smooth surface and are randomly distributed across all the investigated fiber mats. It should be noted that SCO nanoparticles were not observed on the surface of the fibers or in the interstitial spaces between them. Using the SEM images, the fiber diameter distribution was analyzed using an image analysis software (Image J; National Institutes of Health, USA) and the obtained data were further analyzed statistically using OriginLab software. This analysis of the data showed that the mean diameter of the **1**@PVP nanocomposite fibers was 145 nm with a standard deviation of 50 nm, while the **2**@PVP fibers displayed slightly smaller values, with a mean size of 130 nm and a standard deviation of 50 nm. No obvious correlation could be established between fiber size and composition. The thinnest fibers were observed in the **1**@PVP mat with a 1:20 ratio, with an average diameter of 120 nm. The presence of irregularities, in the form of globules, occurred during the fabrication process of SCO nanocomposites and can be observed in the SEM images. This phenomenon has also been frequently reported in the fabrication of other electrospun fibers [3-12], and research has focused on developing strategies to minimize or eliminate their formation, which would improve the properties and performance of nanocomposites in various applications. The SCO properties of the composites were analyzed by means of magnetic measurements using a Quantum Design MPMS instrument operated in a DC magnetic field of 0.1 T at a temperature sweep rate of 2 K/min. Since the exact concentration of the SCO particles in the fibers was not verified, we plot the normalized magnetization data allowing us to compare the spin transition temperatures in a straightforward manner. It can be seen in Figure 3.5 that the SCO temperatures for both materials are significantly altered in the nanofibers when compared to the bulk powder. In particular, for the amino-triazole complex **1**, an impressive broadening of the hysteresis loop is observed in the composite with a hysteresis width of ca. 50 K (vs. 10 K in the bulk). In addition, the rectangular shape of the hysteresis loop is lost, indicating a rather broad distribution of transition temperatures in the composites. On the other hand, the spin state equilibrium temperature, which we can roughly assimilate with the barycenter of the hysteresis, remains similar in each sample.

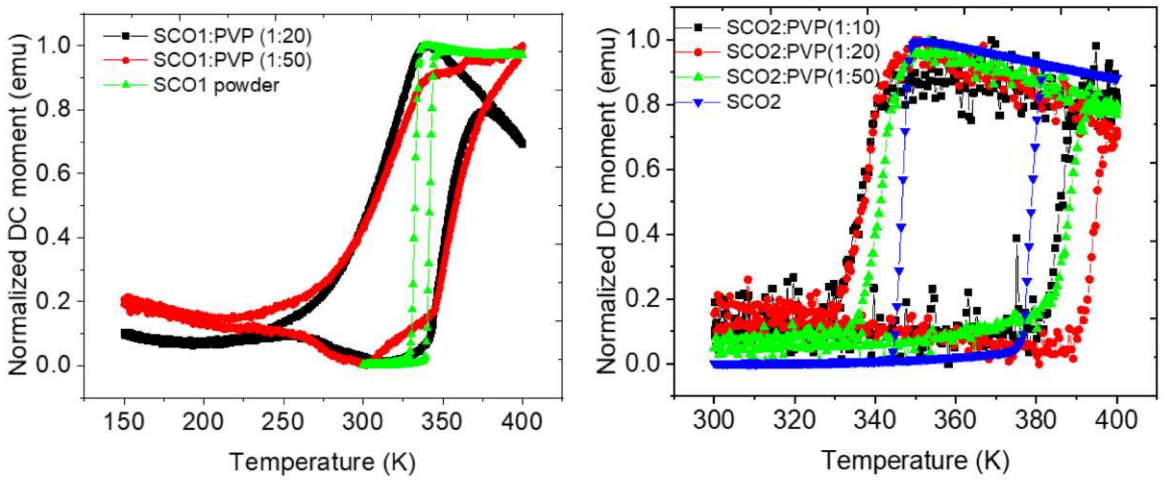

Figure 3.5. *Temperature dependence of the normalized magnetic moment, recorded for the SCO complex **1** (left panel) and **2** (right panel), compared with the magnetic properties of the composite fibers **1**@PVP and **2**@PVP with different filler concentrations.*

As shown in Fig. 3.5 (in the right panel), the composites **2**@PVP exhibit exactly the same tendencies (i.e. the hysteresis broadens and flattens, while remains centered on the same temperature), but the effects in this case are less spectacular when compared to the composites **1**@PVP. Notably, the initial hysteresis width of ca. 30 K seen in complex **2** has broadened to reach values between 45 - 55 K in the composites **2**@PVP. At present, the origin of this broadening of the hysteresis in the electrospun fibers remains non-elucidated. Hysteresis broadening has been also observed in previous studies [18] for spin coated composite films of **2**@PVP, but the possible origin of the matrix effect was not discussed. In the present case, one may speculate that the electrospun PVP nanofibers may exhibit an enhanced elastic modulus, which might lead to an increase of the cooperativity of the SCO phenomenon [19].

3.4.*Fabrication and characterization of SCO@P(VDF-TrFE) nanofibers*

Having established the feasibility of electrospinning of good quality, functional SCO@polymer composite nanofibers, we have turned to our attention to the electrospinning of SCO@piezopolymer fibers.

The piezopolymer P(VDF_{80}-$TrFE_{20}$) was purchased from Arkema Piezotech and used without further purification. The spin-crossover compound $[Fe\{(Htrz)_{1.8}(trz)\}_1(NH_2\text{-}trz)_{0.2}](BF_4)_1\cdot 0.7H_2O$ (**3**) was synthesized by Mario Piedrahita Bello at LCC-CNRS using the method described in ref. [20]. A first solution with 1:9 SCO-P(VDF-TrFE) ratio was prepared by mixing 53.4 mg of complex **3** with 480.6 mg of the polymer and dispersed in 8 ml of acetone using an ultrasound bath for approximately 30 minutes. The mixture was then further homogenized by magnetic stirring for 2 hours at room temperature. A second, more concentrated solution with 1:3 SCO/polymer ratio was also prepared by mixing 67.5 mg SCO powder with 202.5 mg polymer in 8 ml of acetone, following the same procedure of dispersion and homogenization.

Representative SEM images of the composite nanofibers **3**@P(VDF-TrFE) are shown for the two particle concentrations in Figure 3.6.

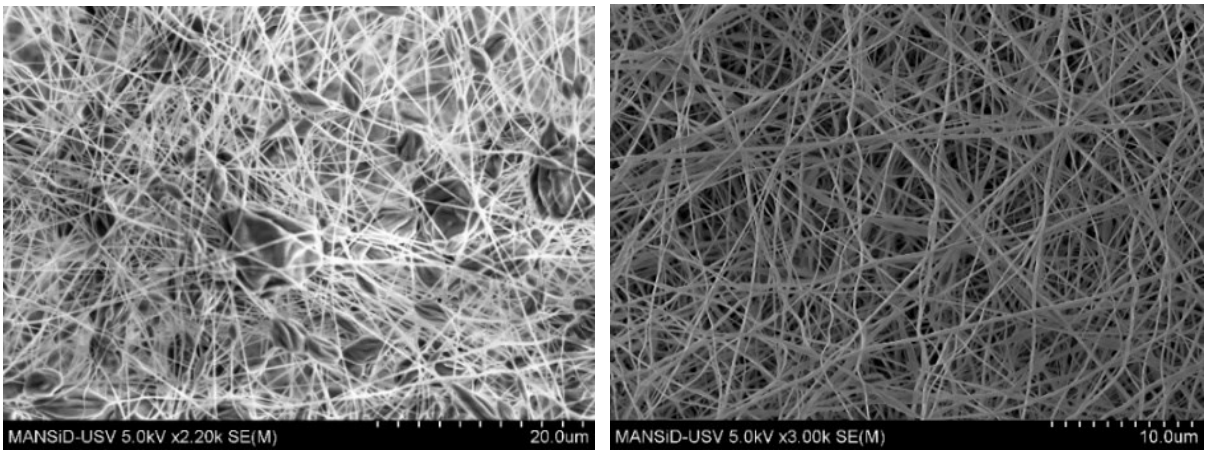

Figure 3.6. *Representative SEM images for the composite nanofibers **3**@P(VDF-TrFE) with 10 wt.% (left panel) and 25 wt.% (right panel) particle concentration.*

Similar to the PVP composites, the SEM images reveal randomly oriented, smooth and narrow, ca. 150 nm average diameter, fibers with a relatively low amount of globules. Interestingly, the fibers with lower particle concentration tend to have a larger diameter, presumably due to the different viscosity of the two solutions. Interestingly, magnetic measurements conducted on the **3**@P(VDF-TrFE) show a significantly smaller impact of the polymer matrix on the spin transition for both studied concentrations (Fig. 3.7). Nevertheless, the general tendency is the same: a shift of the transition temperatures away from the center of the hysteresis loop is observed during both heating and cooling together with a slight flattening of the ascending and descending branches.

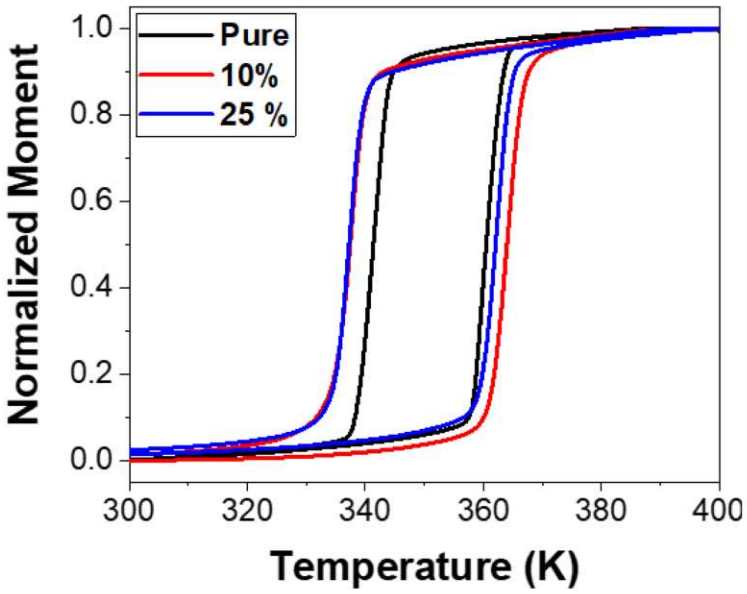

Figure 3.7. *Temperature dependence of the normalized magnetic moment, recorded for the pure SCO complex* ***3*** *and for the composite fibers* ***3****@P(VDF-TrFE) with two different filler concentrations.*

In order to examine the dielectric and charge transport properties of the nanofiber composites we conducted impedance spectroscopy measurements, which have been performed with a CONCEPT 40 Broadband Dielectric Spectrometer coupled to an Alpha-A impedance analyser and a Quatro Cryosystem (Novocontrol GmbH). The sample was disposed in a Teflon sample holder between two parallel plate electrodes made of stainless steel. The amplitude (V_0) of the applied sin waveform AC voltage, $V(t) = V_0 sin(\omega t)$, was 1 V and its frequency was varied between 10^{-1} and 10^6 Hz (Fig. 3.8). Frequency sweeps were carried out isothermally at fixed temperatures between 20 and 120 °C both in heating and cooling modes. The induced current, $I(t) = I_0 sin(\omega t + \delta)$, displays a phase shift, δ, due to the dielectric losses. The complex impedance of the measurement cell is defined as the ratio of the applied AC voltage and the generated current:

$$Z^*(\omega) = Z'(\omega) + iZ''(\omega) = \frac{V}{I} = \frac{1}{i\omega C} \qquad (3.1)$$

where C is the capacitance of the measurement cell. The capacitance is related to the relative permittivity of the material, ε, by:

$$C = \varepsilon\varepsilon_0 \frac{A}{d} \tag{3.2}$$

where ε_0 is the permittivity of vacuum, A is the electrode area and d is the thickness of the studied material. The real and imaginary parts of the frequency dependent complex permittivity, $\varepsilon^*(\omega) = \varepsilon'(\omega) - i\varepsilon''(\omega)$, can be obtained from the measured impedance using the following relationships:

$$\varepsilon'(\omega) = \frac{d \sin\delta}{\omega\varepsilon_0 A Z^*(\omega)} \tag{3.3}$$

$$\varepsilon''(\omega) = \frac{d \cos\delta}{\omega\varepsilon_0 A Z^*(\omega)} \tag{3.4}$$

The real part, ε', is a measure of the stored charge, whereas the imaginary part, ε'', represents the dielectric loss. Besides the complex permittivity, it is sometimes useful to represent the data in terms of the complex electric modulus, $M^*(\omega) = \varepsilon^*(\omega)^{-1}$, or the complex AC conductivity, $\sigma^*(\omega) = i\omega\varepsilon_0\varepsilon^*(\omega)$, which are obtained from the experimental data using the following equations (in combination with equations 3.3 and 3.4):

$$M^*(\omega) = M'(\omega) + iM''(\omega) = \frac{\varepsilon'(\omega)}{\varepsilon'(\omega)^2+\varepsilon''(\omega)^2} + i\frac{\varepsilon''(\omega)}{\varepsilon'(\omega)^2+\varepsilon''(\omega)^2} \tag{3.5}$$

$$\sigma^*(\omega) = \sigma'(\omega) + i\sigma''(\omega) = \omega\varepsilon_0\varepsilon''(\omega) + i\omega\varepsilon_0\varepsilon'(\omega) \tag{3.6}$$

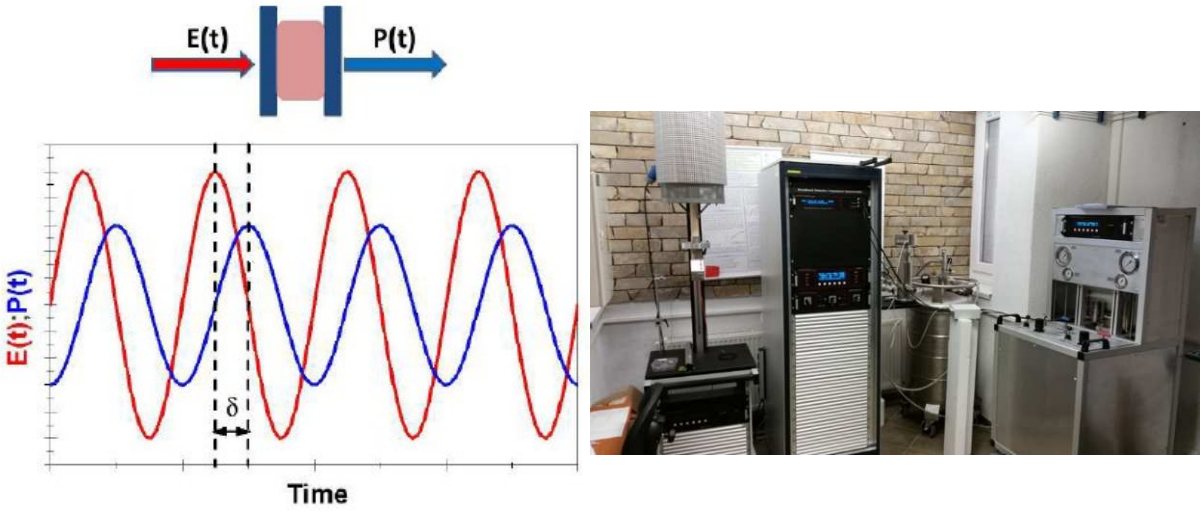

Figure 3.8. *Left panel: Scheme of the impedance spectroscopy measurement principle showing also the variation of the applied electrical field and the induced polarization of the sample. Right panel: Photograph of the broadband dielectric spectrometer.*

Impedance spectroscopy measurements were conducted on the pure SCO complex **3**, on its composites formed into fibers containing 10 wt.% and 25 wt.% SCO content, on nanofibers of the pure P(VDF-TrFE) polymer and on blade casted **3**@ P(VDF-TrFE) films with 25 wt.% particle load (see photographs in Fig. 3.9). As shown in Figure 3.10, the conductivity values for the pure P(VDF-TrFE) copolymer (~pS/cm at 20 °C) are lower than those of the SCO material or its composites (~nS/cm at 20 °C), but the latter remain largely insulating. The

conductivity is thermally activated in each sample as it can be expected for a hopping charge transport [21].



Figure 3.9. *Photographs of the blade-casted (left) and electrospun (right) samples of* ***3****@P(VDF-TrFE).*

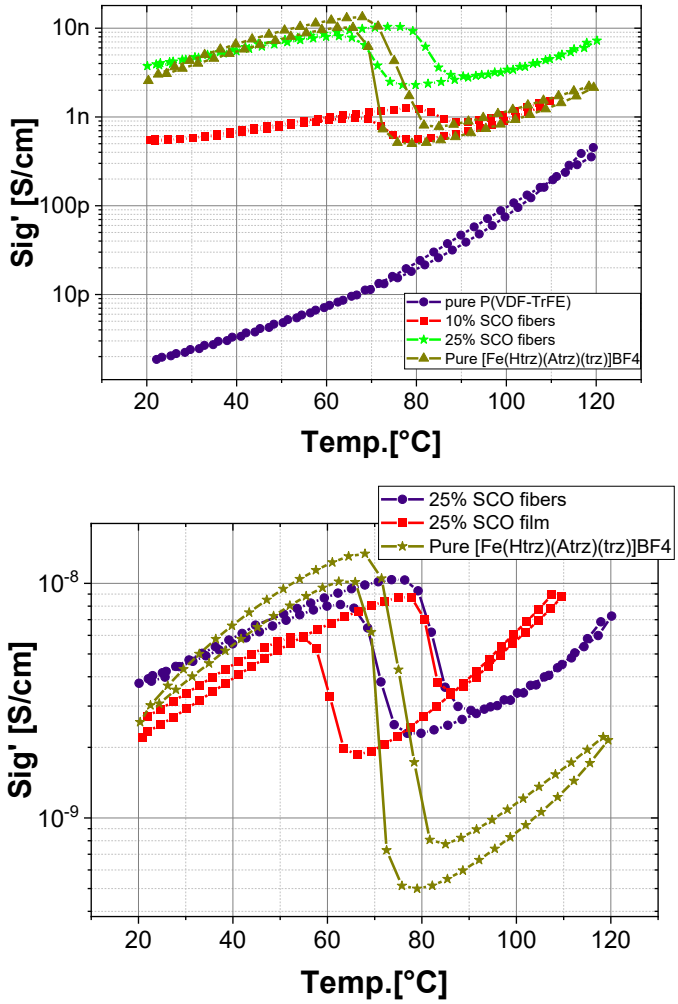

Figure 3.10. *Top panel: Real part of the complex conductivity (at 10 kHz) as a function of the temperature for nanofibers of the pure complex* ***3****, the pure P(VDF-TrFE) fibers and* ***3****@P(VDF-TrFE) composite fibers with 10 and 25 wt.% particle load. Bottom panel: The same data for the pure complex* ***3****, the nanocomposite fibers (25% SCO) and the blade-casted composite film (25 % SCO).*

In agreement with the magnetic measurements, the spin transition temperatures for the composite materials show a larger hysteresis width when compared to the pure powder. The LS to HS spin transition in the latter sample gives rise to a (reversible) drop of the conductivity by more than an order of magnitude. This finding is similar to what has been observed for this family of complexes previously [22-25]. As it can be expected, the amplitude of the conductivity switching between the two spin states gets reduced in the diluted composite samples, but remains still observable at 10 % SCO particle concentration. It is worth to note also that the Curie temperature of the 80:20 copolymer we used in this study (ca. 135 °C, see Chapter 2) is not reached in our dielectric measurements. Figure 3.10 (bottom panel) displays also a comparison of the conductivity of the nanofiber composite and blade-casted film samples (both with 25% SCO load in the same matrix). Although the spin transition temperatures are somewhat different, the temperature dependent behavior of the conductivity in the two samples appear remarkably similar, indicating that the different processing of the samples does not impart significant changes in their electrical properties.

As we have seen above, the temperature dependence of the conductivity at a fixed frequency provides useful information about the charge carrier transport in our composites, a deeper understanding of the electrical properties can be inferred from the analysis of the frequency dependent dielectric relaxation behavior. In most cases, dielectric relaxation phenomena are analyzed using either the theoretically well founded Debye function, or using different phenomenological functions [26]. The relaxation processes are characterized by a peak in the imaginary part of the permittivity, ε'', and a step-like decrease in the real part, ε', of the complex dielectric function $\varepsilon^*(\omega)$ (Fig. 3.11, left panel). Alternatively, the so-called Cole-Cole plot (i.e. the ε'' vs. ε' diagram) can be also advantageously used to depict the relaxation processes (Fig. 3.11, right panel). The Debye function for the frequency dependence of ε^* is given by:

$$\varepsilon^*(\omega) = \varepsilon_\infty + \frac{\Delta\varepsilon}{1+i\omega\tau_D} \tag{3.7}$$

where the model parameters are the Debye relaxation time, τ_D, and the dielectric relaxation strength, $\Delta\varepsilon = \varepsilon_S - \varepsilon_\infty$, where ε_∞ and ε_S stand for the permittivity in the high and low frequency limits, respectively. The relaxation time is related to the loss peak maximum by $\tau_D = {\omega_{max}}^{-1}$. The analysis of the temperature dependence of the relaxation times, using for example the Arrhenius law, provides the energy barriers associated with the relaxation process. The Debye relaxation leads to a semicircle in the Cole-Cole plot, but in most materials a broadening and asymmetry of both the Cole-Cole diagram and of the loss peak can be evidenced experimentally. These phenomena are usually analyzed by means of the phenomenological Havriliak-Negami (HN) model is given by:

$$\varepsilon^*_{HN}(\omega) = \varepsilon_\infty + \frac{\Delta\varepsilon}{(1+(i\omega\tau_{HN})^\beta)^\gamma} \tag{3.8}$$

where β and γ are fractional shape parameters ($0 < \beta, \gamma \leq 1$) that describe the symmetric and asymmetric broadening of the complex dielectric function, respectively. They can be interpreted as parameters related to the relaxation time distribution. Their effect on the Cole-

Cole plot can be depicted in Figure 3.11. In the frame of the HN model, the real and imaginary parts of the dielectric permittivity are given by:

$$\varepsilon'(\omega) = \varepsilon_{\infty} + \Delta\varepsilon \cos(\gamma\theta)[1 + 2(\omega\tau)^{\beta} \cos\left(\frac{\beta\pi}{2}\right) + (\omega\tau)^{2\beta}]^{-\frac{\gamma}{2}} \quad (3.9)$$

$$\varepsilon''(\omega) = \Delta\varepsilon \sin(\gamma\theta)[1 + 2(\omega\tau)^{\beta} \cos\left(\frac{\beta\pi}{2}\right) + (\omega\tau)^{2\beta}]^{-\frac{\gamma}{2}} \quad (3.10)$$

where

$$\theta = arctan\left[\frac{\sin\left(\frac{\beta\pi}{2}\right)}{(\omega\tau)^{-\beta} + \cos\left(\frac{\beta\pi}{2}\right)}\right] \quad (3.11)$$

The HN analysis helps identify the origins and behavior of dielectric relaxation processes observed in the frequency measurements. In general, the imaginary part of the permittivity is better suited for fitting because it has a peak-like shape.

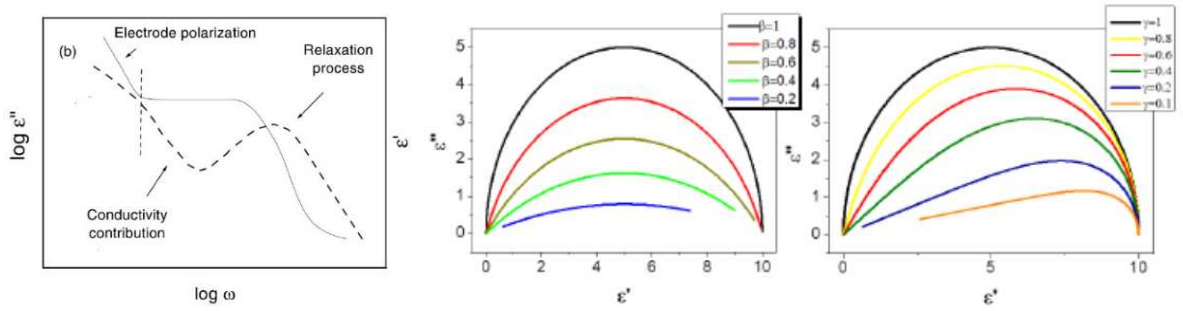

Figure 3.11. *Left panel: Schematic representation of the real part (solid line) and imaginary part (dashed line) of the dielectric permittivity over the frequency spectrum. Middle and right panels: Cole-Cole plots simulated for various values of the shape parameters β and γ, respectively.*

The HN approach has been already used for the analysis of dielectric spectra of the pure complexes **2** [25] and **3** [23]. These studies revealed three distinct dielectric relaxation processes in the frequency range between 1 Hz and 1 MHz, which were ascribed to interface polarization, dipole orientation and charge transport phenomena. At low frequencies, electrode polarization at the electrode-material interface and interface polarization in heterogeneous materials (Maxwell-Wagner polarization) occurs ubiquitously due to the accumulation of charge carriers at interfaces. The charges can be separated at large distances and, as a result, this contribution to the dielectric loss can be very important. Strictly speaking, this contribution is not a material property and it could be different depending on how the material is processed and how the measurement cell is prepared. In particular, electrode polarization is considered as a parasitic effect in dielectric measurements. Its origin can be verified by changing the electrode material and/or the sample thickness and the modulus formalism (Eq. 3.5) offers an effective means to eliminate the associated low frequency tail from the dielectric spectra, revealing more clearly the dipole and conductivity relaxation processes [27]. Another contribution comes from the mobility of charge carriers. In low mobility systems, such as most of molecular solids and polymers, the charge transport occurs via site-to-site hopping of localized charge carriers. The

motion of charges requires a rearrangement of the surrounding charges, associated with a characteristic relaxation time. Charge transport will occur only if the frequency of the applied field is lower than the inverse relaxation time, in which case the polarization cloud can follow the movement of the charge. Interestingly, the frequency and temperature dependence of the conductivity of low mobility solids shows a remarkable similitude for a large variety of rather different materials (glasses, molecular crystals, organic polymers, disordered semiconductors, composites) which is often described by the phenomenological Jonscher equation [28]:

$$\sigma'(\omega) = \sigma_0 + A\omega^n = \sigma_{DC}\left[1 + \left(\frac{\omega}{\omega_c}\right)^n\right] \tag{3.12}$$

where σ_{DC} is the DC conductivity, A and n are phenomenological constants, and ω_c is a cut-off frequency, which separates the low-frequency region, which is essentially the frequency independent DC conductivity, from the high-frequency AC conductivity region, which exhibits a power law frequency dependence, characterized by n. Finally, dielectric relaxation occurs also via a third important mechanism, the rotation of mobile dipoles (bound charges) in response to the applied field. These rotational fluctuations of dipoles are related to characteristic parts of the material (functional groups) and their investigation by dielectric spectroscopy provides useful information about the dynamics of the system.

In the following, we focus on the HN analysis of the dielectric spectra of the powder sample of complex 3, the P(VDF-TrFE) nanofibers and the composite nanofibers with 10 % SCO load. The variable temperature dielectric spectra of the SCO powder and the polymer are presented in Figure 3.12. For the polymer fibers, the imaginary part of the permittivity at low frequencies changes considerably with temperature. In contrast, the SCO material displays permittivity values that remain within the same order of magnitude across the temperature range studied. This suggests that, in contrast to the polymer fibers, the dielectric spectrum of the SCO material is dominated by electrode (or interfacial) polarization, which masks to a large extent the other relaxation processes. We can suggest that this difference is linked, at least partly, to the higher conductivity of the SCO material, which is known to favor a strong electrode polarization [27]

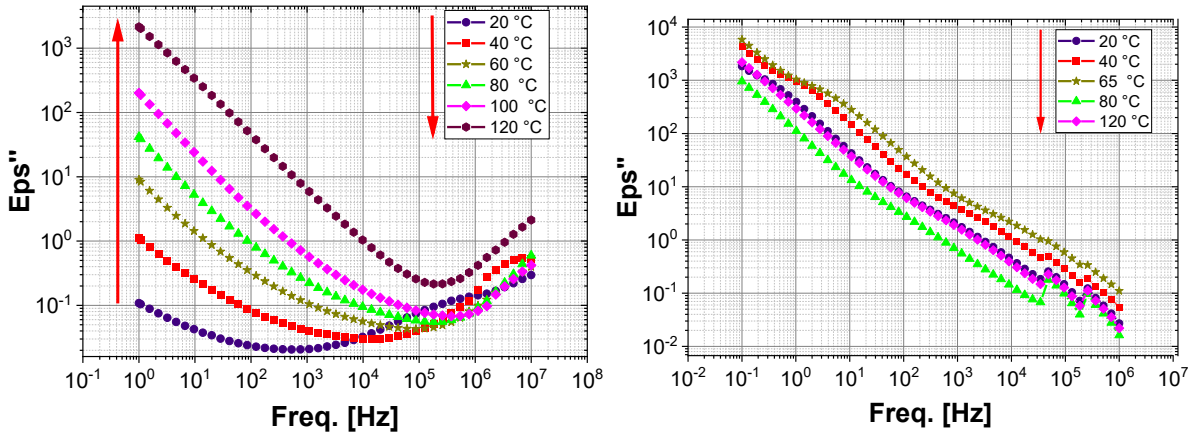

Figure 3.12. *Imaginary part of the permittivity as a function of the frequency of the applied electrical field at different temperatures for the neat P(VDF-TrFE) fibers (left) and the pure SCO complex* ***3*** *(right).*

Remarkably, in the SCO composite nanofiber we observe a significant change in the shape of the dielectric spectra (Fig. 3.13, left) when compared either to the neat SCO material or to the neat polymer. Due to the lower permittivity values of P(VDF-TrFE) at medium frequencies, a distinct independent peak appears near 500 Hz, which is related to the spin crossover phenomenon (refer to "Fit peak 2" of the HN analysis in Figure 3.13, left).

Knowing that the high-frequency peak is associated with the polymer, we can attribute this contribution to "Fit peak 3" in the pure SCO compound (Figure 3.13, right). Previous publications have clarified that this feature is linked to charge transfer phenomena within the SCO material, which shows a maximum spin-state dependence at this frequency [25].

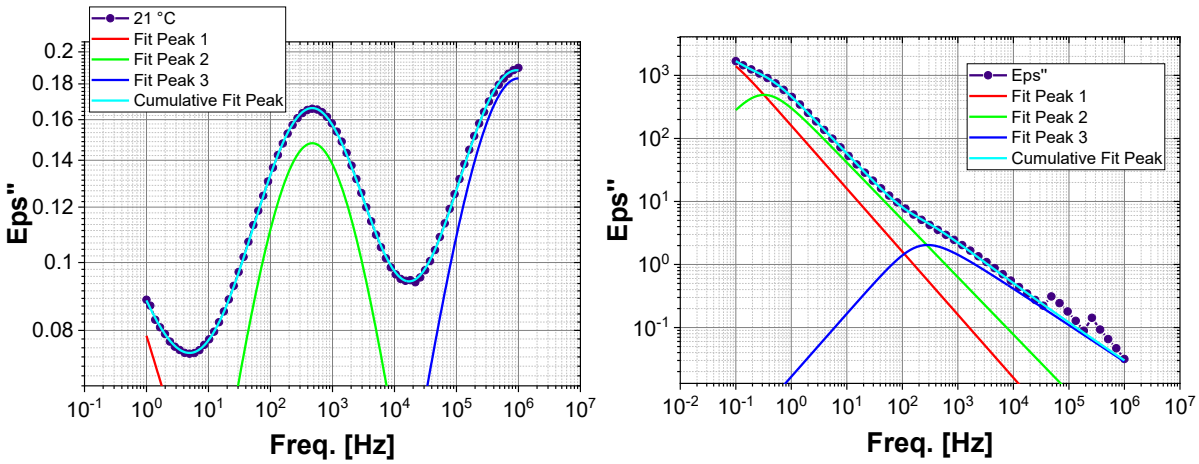

Figure 3.13. *Havriliak-Negami fit of the imaginary part of permitivity of the 10% SCO@P(VDF-TrFE) nanofiber composite (left) and of the pure SCO material (right) recorded at 20 °C. A good global fit of the experimental data could be obtained in both cases using 3 HN components.*

Based on the HN fit obtained at room temperature (Fig. 3.13), a detailed HN analysis was performed on the ensemble of the spectra obtained during both heating and cooling for both materials. As it can be expected, we observed that the different relaxation peaks shift to higher frequencies as the temperature increases. Specifically, in the temperature range of the SCO phenomenon (ca. 60-90 °C) the high-frequency relaxation associated with the polymer is observed only as a "tail" in the spectra, which has therefore been discarded from the fitting process. In this novel fit, the conductivity relaxation corresponds thus to "Fit Peak 3" (Fig. 3.14). This figure displays two graphs illustrating the dielectric spectra corresponding to the low spin and high spin states at 77 °C, which lies within the hysteresis loop of the spin transition. Thanks to this hysteresis property one can thus compare the dielectric properties of the material at the SAME temperature, which means that any ordinary temperature dependence of the dielectric properties can be safely discarded from the analysis. The low-frequency "Fit peak 1" corresponds, as usual, to electrode/interface polarization effects. An interesting observation is the presence of "Fit Peak 2", which emerges at higher temperatures. The origin of this peak is not clear, but most likely it should be associated to a dipole relaxation process, presumably linked to the presence of water molecules in the structure. Indeed, previous works on the SCO powder sample have already evidenced the presence of these three contributions. The analysis

revealed a remarkable correlation between the frequency dependence of the conductivity switching, $\sigma'_{LS}/\sigma'_{HS}$, amplitude (resp. permittivity switching, $\varepsilon'_{LS}/\varepsilon'_{HS}$, amplitude) and the frequency maximum of "Fit Peak 3" (resp. "Fit Peak 2"). This deconvolution of the different dielectric relaxation processes offers a powerful means for their independent analysis. In particular, the decoupled contribution of the peak related to charge transport of the SCO material ('Fit Peak 3') reveals several interesting observations. For the pure spin crossover material, the dielectric strength of this relaxation contribution changes by nearly two orders of magnitude, from 10 to 0.2, upon the LS to HS spin transition (Fig. 3.15, left). In contrast, the dielectric strength for the 10 % composite nanofibers changes only from 1 to 0.4 between the two spin states. This finding parallels the magnitude of conductivity switching seen in these two samples (Fig. 3.10) and offers thus an explanation for its origin.

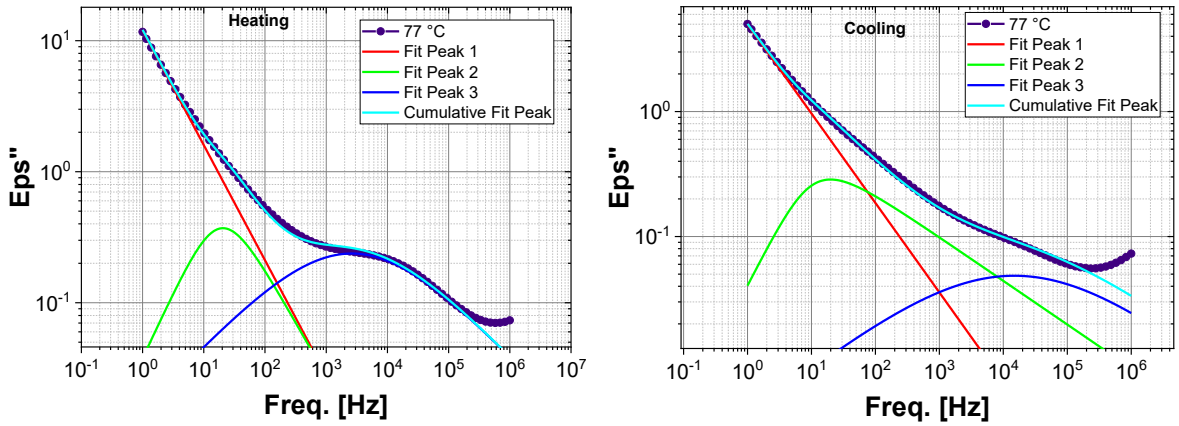

Figure 3.14. *Havriliak-Negami fit of the imaginary part of permittivity of the 10% SCO@P(VDF-TrFE) nanofiber composite acquired at 77 °C in the heating mode, LS state, (left) and in the cooling mode, HS state, (right).*

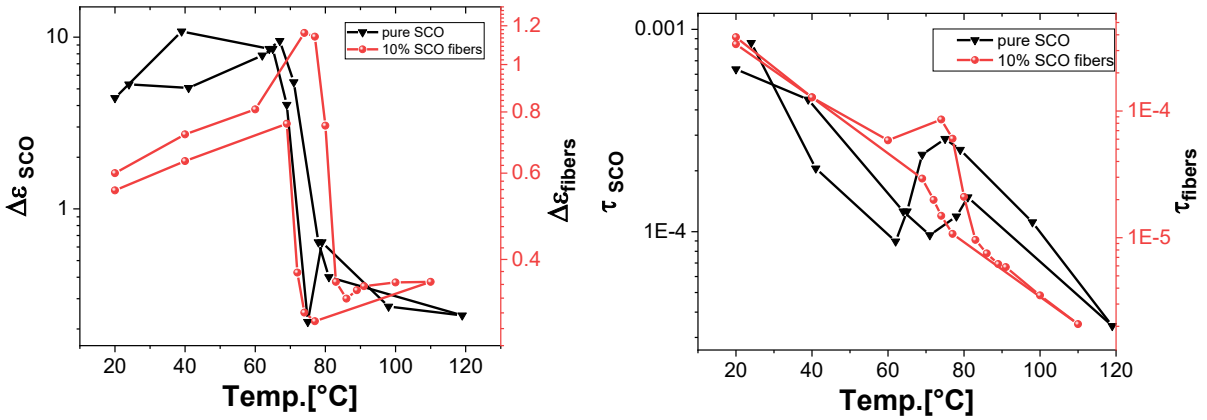

Figure 3.15. *Temperature dependence of the dielectric strength (left) and the relaxation time (right) associated with the conductivity relaxation phenomenon acquired for the pure SCO powder and for the 10 % SCO@P(VDF-TrFE) nanofiber composite during a complete heating-cooling cycle. The left-hand y-axis in black (resp. right-hand in red) refers to the pure SCO material (resp. the composite fibers).*

A first remark we can make concerns the relatively large magnitude of the conductivity relaxation contribution to the effective dielectric permittivity of the material in the LS state. Since the transition to the HS state results in a very significant drop of the dielectric relaxation strength, we can suggest that the spin transition can offer an interesting means to modulate the quantity of charges stored by the material. To our best knowledge, this aspect of the spin transition phenomenon has not yet been considered in the literature and offers and interesting perspective for future work. The origin of this reduction in dielectric relaxation strength (related to the charge transport) in the HS state, and also in the composite, remains unknown, but one can suggest it might be linked to the reduced dipole density of the material. Another interesting observation concerns the conductivity relaxation times, which are one order of magnitude lower for the nanofibers than for the SCO powder. This result is somewhat unexpected and suggests that the presence of the polymer matrix impacts the charge carrier hopping frequencies. As for the temperature dependence of the conductivity relaxation times, far from the SCO region we observe a monotonous decrease with similar slopes in the HS and LS phases, indicating that the activation energies are not substantially different. The observed increase of the relaxation time when going from the LS to the HS state can be then linked to the pre-exponential factor, i.e. to the change of phonon frequencies, which drive the hop of the charge carrier [27]. Indeed, it is well known that the phonon frequencies increase significantly in the LS phase, which explains thus the spin-state dependent behavior of the conductivity relaxation time.

3.5. Conclusions

The successful fabrication of SCO@polymer composite nanofibers through electrospinning has been achieved for various spin crossover materials and polymers. In each case, the polymer matrix shows to have a sizeable impact on the spin transition behavior, manifested by an increase of the hysteresis width and a less abrupt transition, whereas the barycenter of the hysteresis did not change considerably. This means that the matrix (and/or the electrospinning process) does not impact the spin state equilibrium, but it alters the cooperativity and givers rise also to a broader distribution of transition temperatures. The latter phenomenon can be associated with the heterogeneous nature of the composites, whereas the hysteresis broadening might be linked to the increased stiffness of the polymer in the formed nanofibers. However, this hypothesis remains to be verified by further experiments. In any case, this finding indicates the electrospun nanofiber composites of SCO materials can be produced with different hysteresis widths, which is a potentially useful asset. We have also conducted a detailed analysis of the electrical properties of the composite nanofibers using variable temperature broadband dielectric spectroscopy. We employed the Havriliak-Negami approach to separately investigate the different contributions to the global dielectric response. We have shown that the composite nanofibers exhibit distinct dielectric properties compared to pure SCO material and the polymer fibers. Through this analysis we made correlations between the reduced conductivity in the composite nanofibers (vs. the neat SCO powder) and the dielectric relaxation parameters. We have also established the links between the spin state of the composite and its dielectric properties. In particular, we have evidenced a strongly reduced dielectric relaxation strength in the HS state, suggesting possible applications in charge storage

and manipulation through the SCO phenomenon. Unfortunately, we could not yet characterize the piezoelectric properties of the electrospun SCO@P(VDF-TrFE) composite nanofibers, which will necessitate the use of dedicated techniques, such as piezo-force microscopy (PFM).

References

[1] Persano, L., Dagdeviren, C., Su, Y., Zhang, Y., Girardo, S., Pisignano, D., ... & Rogers, J. A. (2013). High performance piezoelectric devices based on aligned arrays of nanofibers of poly (vinylidenefluoride-co-trifluoroethylene). Nature communications, 4(1), 1633, 10.1038/ncomms2639.

[2] Havriliak, S., & Negami, S. (1967). A complex plane representation of dielectric and mechanical relaxation processes in some polymers. Polymer, 8, 161-210, 10.1016/0032-3861(67)90021-3.

[3] K. Ramakrishna et al. An Introduction to Electrospinning and Nanofibers, World Scientific Publishing, Singapure, 2005.

[4] Venmathi Maran, B. A., Jeyachandran, S., & Kimura, M. (2024). A Review on the Electrospinning of Polymer Nanofibers and Its Biomedical Applications. Journal of Composites Science, 8(1), 32, 10.3390/jcs8010032.

[5] Sahay, R., Kumar, P. S., Sridhar, R., Sundaramurthy, J., Venugopal, J., Mhaisalkar, S. G., & Ramakrishna, S. (2012). Electrospun composite nanofibers and their multifaceted applications. Journal of Materials Chemistry, 22(26), 12953-12971, 10.1039/C2JM30966A.

[6] Zhang, C. L., & Yu, S. H. (2014). Nanoparticles meet electrospinning: recent advances and future prospects. Chemical Society Reviews, 43(13), 4423-4448., 10.1039/C3CS60426H.

[7] Ico, G., Showalter, A., Bosze, W., Gott, S. C., Kim, B. S., Rao, M. P., ... & Nam, J. (2016). Size-dependent piezoelectric and mechanical properties of electrospun P (VDF-TrFE) nanofibers for enhanced energy harvesting. Journal of Materials Chemistry A, 4(6), 2293-2304, 10.1039/C5TA10423H.

[8] Kim, S. R., Yoo, J. H., Cho, Y. S., & Park, J. W. (2019). Flexible piezoelectric energy generators based on P (VDF-TrFE) nanofibers. Materials Research Express, 6(8), 086311, 10.1088/2053-1591/ab1ee8.

[9] You, S., Zhang, L., Gui, J., Cui, H., & Guo, S. (2019). A flexible piezoelectric nanogenerator based on aligned P (VDF-TrFE) nanofibers. Micromachines, 10(5), 302, 10.3390/mi10050302.

[10] Echeverria, C., Rubio, M., Mitchell, G. R., Roig, A., & López, D. (2015). Hybrid polystyrene based electrospun fibers with spin-crossover properties. Journal of Polymer Science Part B: Polymer Physics, 53(11), 814-821, 10.1002/polb.23702.

[11] Dreyer, B., Natke, D., Klimke, S., Baskas, S., Sindelar, R., Klingelhöfer, G., & Renz, F. (2018). Implementation of spin crossover compounds into electrospun nanofibers. Hyperfine Interactions, 239, 1-8. 10.1007/s10751-017-1483-x.

[12] Kilic, M. S., Brehme, J., Pawlak, J., Tran, K., Bauer, F. W., Shiga, T., ... & Renz, F. (2023). Incorporation and deposition of spin crossover materials into and onto electrospun nanofibers. Polymers, 15(10), 2365. 10.3390/polym15102365.

[13] Salmon, L., & Catala, L. (2018). Spin-crossover nanoparticles and nanocomposite materials. Comptes Rendus Chimie, 21(12), 1230-1269, 10.1016/j.crci.2018.07.009.

[14] Enriquez-Cabrera, A., Rapakousiou, A., Bello, M. P., Molnár, G., Salmon, L., & Bousseksou, A. (2020). Spin crossover polymer composites, polymers and related soft materials. Coordination Chemistry Reviews, 419, 213396, 10.1016/j.ccr.2020.213396.

[15] Utkarsh, Hegab, H., Tariq, M., Syed, N. A., Rizvi, G., & Pop-Iliev, R. (2020). Towards analysis and optimization of electrospun PVP (polyvinylpyrrolidone) nanofibers. Advances in Polymer Technology, 2020(1), 4090747, 10.1155/2020/4090747.

[16] Piedrahita-Bello, M., Angulo-Cervera, J. E., Courson, R., Molnár, G., Malaquin, L., Thibault, C., ... & Bousseksou, A. (2020). 4D printing with spin-crossover polymer composites. Journal of Materials Chemistry C, 8(18), 6001-6005, 10.1039/D0TC01532F.

[17] Suleimanov, I., Costa, J. S., Molnár, G., Salmon, L., Fritsky, I., & Bousseksou, A. (2015). Effect of ligand substitution in [Fe (H-trz) 2 (trz)] BF4 spin crossover nanoparticles. French-Ukrainian Journal of Chemistry, 3(1), 66-72, 10.17721/fujcV3I1P66-72.

[18] Zhang, Y., Alavi, S. E., Soroceanu, I., Kamau, D. W., Rotaru, A., Séguy, I., ... & Bousseksou, A. (2024). Electrical Sensing of Molecular Spin State Switching in a Spin Crossover Complex Using an Organic Field-Effect Transistor. Advanced Electronic Materials, 2400590, 10.1002/aelm.202400590.

[19] Félix, G., Nicolazzi, W., Salmon, L., Molnár, G., Perrier, M., Maurin, G., ... & Bousseksou, A. (2013). Enhanced Cooperative Interactions at the Nanoscale in Spin-Crossover Materials with a First-Order Phase Transition. Physical review letters, 110(23), 235701, 10.1103/PhysRevLett.110.235701.

[20] Piedrahita-Bello, M., Angulo-Cervera, J. E., Enriquez-Cabrera, A., Molnár, G., Tondu, B., Salmon, L., & Bousseksou, A. (2021). Colossal expansion and fast motion in spin-crossover@ polymer actuators. Materials Horizons, 8(11), 3055-3062, 10.1039/d1mh00966d.

[21] Lefter, C., Gural'skiy, I. Y. A., Peng, H., Molnár, G., Salmon, L., Rotaru, A., ... & Demont, P. (2014). Dielectric and charge transport properties of the spin crossover complex [Fe(Htrz)2(trz)](BF4). physica status solidi (RRL)–Rapid Research Letters, 8(2), 191-193, 10.1002/pssr.201308256.

[22] Rotaru, A., Guralskiy. I.Y.A., Molnar, G., Salmon, L., Demont, P., & Bousseksou, A. (2012). Spin state dependence of electrical conductivity of spin crossover materials. Chemical Communications, 48(35), 4163-4165, 10.1039/c2cc30528c.

[23] Soroceanu, I., Lupu, S. L., Rusu, I., Piedrahita-Bello, M., Salmon, L., Molnár, G., ... & Rotaru, A. (2020). Ligand substitution effects on the charge transport properties of the spin crossover complex [Fe (Htrz)1+ y− x(trz)2−y(NH2trz)x](BF4)y·nH2O. Journal of Physics: Condensed Matter, 32(26), 264002, 10.1088/1361-648X/ab7ba2.

[24] Lefter, C., Tricard, S., Peng, H., Molnar, G., Salmon, L., Demont, P., ... & Bousseksou, A. (2015). Metal Substitution Effects on the Charge Transport and Spin Crossover Properties of [Fe1–xZnx(Htrz)2(trz)](BF4)(trz=Triazole). The Journal of Physical Chemistry C, 119(16), 8522-8529, 10.1021/acs.jpcc.5b01117.

[25] Soroceanu, I., Graur, A., Coca, E., Salmon, L., Molnar, G., Demont, P., ... & Rotaru, A. (2019). Broad-band dielectric spectroscopy reveals peak values of conductivity and permittivity switching upon spin crossover. The Journal of Physical Chemistry Letters, 10(23), 7391-7396, 10.1021/acs.jpclett.9b02678.

[26] Kremer, F., Schönhals A. (Eds.), Broadband dielectric spectroscopy, Springer-Verlag, Berlin Heidelberg, Germany, 2003.

[27] Molnár, G., Cobo, S., Mahfoud, T., Vertelman, E. J., Van Koningsbruggen, P. J., Demont, P., & Bousseksou, A. (2009). Interplay between the charge transport phenomena and the charge-transfer phase transition in Rb x Mn [Fe (CN) 6] y· z H2O. The Journal of Physical Chemistry C, 113(6), 2586-2593, 10.1021/jp8090478.
[28] Jonscher A.K. (1983) Dielectric relaxation in solids. Chelsea Dielectrics Press, London

Chapter 4. Thermal Energy Harvesting Using a Hybrid Pyroelectric - Spin Crossover System

In this chapter, we describe the fabrication and properties of a thermal energy harvesting system based on multilayer cantilevers comprising of a piezopolymer, a spin crossover and two electrode layers. The piezopolymer is used as a pyroelectric generator. In addition, complementary piezoelectric harvesting is achieved through the actuation of the cantilever bending by the thermally-induced SCO phenomenon. Thus, by combining a SCO material with a piezoelectric layer in a cantilever configuration, we harness the 'giant' thermal expansion of the SCO particles that results from the spin transition to generate piezoelectric currents. We fabricated the cantilevers using needle-shaped $[Fe(Htrz)(Atrz)(trz)]BF_4$ SCO nanoparticles, embedded in a $P(VDF_{80}\text{-}TrFE_{20})$ matrix, in combination with a neat $P(VDF_{80}\text{-}TrFE_{20})$ layer and two Ag particle-doped $P(VDF_{80}\text{-}TrFE_{20})$ electrodes. The four layers were blade-casted and hot-pressed, followed by poling and analysis of the electrical output under controlled thermal cycling.

4.1. Introduction

The piezoelectric effect refers to the generation of electrical charges due to mechanical stress (and vice versa). Piezoelectric materials have proved to have a vast number of implementations in our daily life. The studies regarding different types of piezoelectric materials are outstanding - from the implementation of the piezoelectric materials in electronics, such as frequency generators, sensors, interactive smart screens to the mechano-electrical actuators and electrical energy generators. The links between ferroelectric, pyroelectric, piezoelectric and dielectric materials are highlighted in Fig. 4.1 showing that ferroelectric materials are a subgroup of pyroelectrics, which themselves are a subgroup of piezoelectrics and all of them are dielectrics [1].

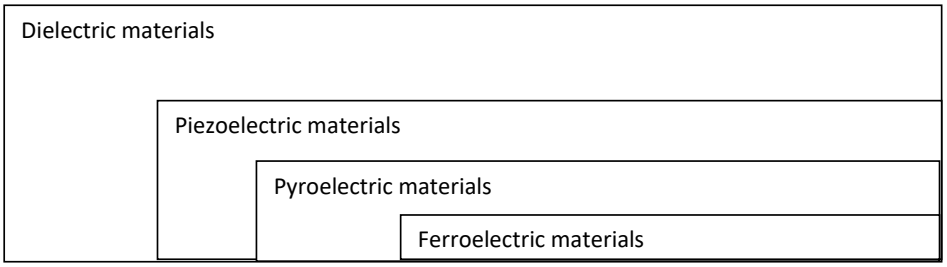

Figure 4.1. *Interrelationship between piezoelectric, pyroelectric, ferroelectric, and dielectric materials.*

Here we are interested in pyroelectric materials, which can transform temporal temperature changes into electric charges. This effect arises in certain piezoelectric materials, which develop spontaneous electrical polarization (i.e. without the application of mechanical stress). If the temperature increases or decreases, a pyroelectric current (or voltage) is generated in these materials, which is given by:

$$I = dQ/dt = Ap(dT/dt) \quad (4.1)$$

where Q is the generated charge, A is the electrode surface area and p is the pyroelectric charge coefficient. From Eq. 4.1 it appears that the sign of the current will change if the sign of dT/dt (heating or cooling) changes. The pyroelectric coefficient (at constant stress) is a sum of the following two terms:

$$p = p1 + p2 = p1 + dC\alpha \tag{4.2}$$

with d, C and α being, respectively, the piezoelectric charge coefficient, the elastic stiffness tensor and the coefficient of thermal expansion (CTE). In Eq. 4.2, $p1$ refers to the pyroelectric effect at constant strain, also called the 'primary pyroelectric coefficient', whereas $p2$ is the 'secondary pyroelectric coefficient', which results from the thermally induced deformation of the material [2]. It is important to specify that in some pyroelectric materials the spontaneous polarization can be reversed by the application of an external electric field. These ferroelectric materials display a polarization vs. electric field hysteresis loop in their low-temperature ferroelectric phase, which vanishes in the high-temperature paraelectric phase above the so-called Curie temperature.

As shown by Eq. 4.1, pyroelectric materials provide a potential for thermal energy harvesting. Indeed, recently, considerable efforts have been devoted to the optimization of pyroelectric harvesters, but the limited performance has not yet allowed for their widespread deployment [3]. In this context, our team has recently proposed a composite approach, wherein an SCO particle filler, displaying large thermal strain at the spin transition, is used to enhance the value of CTE in equation 4.2. In other words, the input thermal energy is transformed into the output electrical energy in two steps, using a coupling parameter, which is the mechanical strain. In the first step, the SCO filler efficiently transforms the thermal energy into a large strain, which will then be the input parameter for the second step, in which the piezoelectric matrix transforms the mechanical energy into electrical charges. Obviously, a good mechanical coupling between the two constituents is necessary and, for a maximum current output, one should use a pyroelectric material, which combines the piezoelectric harvesting (p2) with conventional pyroelectric harvesting (p1). This idea has been first explored during the doctoral studies of Sylvan Rat where composite films with 25 % nanoparticle load of the SCO complex $[Fe\{(Htrz)_2(trz)\}_{0.9}(NH_2\text{-}trz)_{0.3}](BF_4)_{1.1}$ (trz = 1,2,4-triazolato) embedded in a $P(VDF_{70}\text{-}TrFE_{30})$ matrix, were drop-casted [4]. The films were poled in a 18 MV m^{-1} electric field, resulting in a piezoelectric charge coefficient d_{33} of -3.3 pC/N. Remarkably, these films showed a current discharge peak at the spin transition (Fig. 4.2a), associated with the 'giant' thermal expansion of ca. 1300 ppm/°C of the composite (Fig. 4.2b). These results opened thus an interesting scope for the development of thermal energy harvesting devices.

Further optimization of these SCO@P(VDF-TrFE) composites was researched during the PhD thesis of Mario Piedrahita-Bello. The co-polymer composition was changed to $P(VDF_{75}\text{-}TrFE_{25})$, which displays higher Curie temperature, in order to better separate the SCO and Curie transitions. In addition, the influence of the morphology, concentration and chemical composition of the SCO particles was optimized and a blade casting method was implemented instead of simple solvent casting [5]. As a result, composites with higher crystallinity of the

piezo-polymer matrix and thus higher piezoelectric coefficients (up to -13 pC/N) could be obtained. Let us also note that complementary work was also conducted and presented in the PhD thesis of José Elias Angulo Cevrera, wherein a spray-coating method was implemented to fabricate SCO@P(VDF-TrFE) composites with reduced thicknesses (down to the sub-micrometre range), which is particularly advantageous for micro-device integration, providing also enhanced thermalization rates and reduced poling voltages [6].

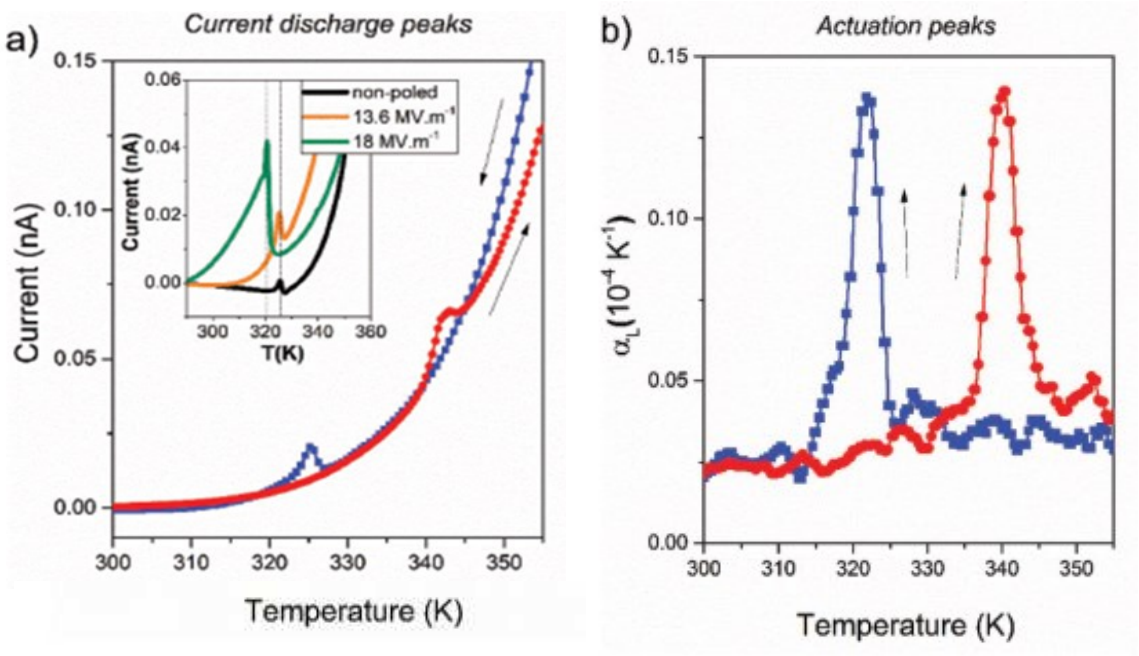

Figure 4.2. *a) Short-circuit current (at 0 V) upon thermal cycling of a SCO@P(VDF$_{70}$-TrFE$_{30}$) composite showing discharge peaks at the spin transition. b) CTE of the same composite as a function of the temperature showing thermal expansion peaks at the spin transition [4].*

However, by using such 33-mode connectivity (Figure 4.11) of particulate composites by mixing the SCO particles with the piezo-polymer, revealed a major obstacle, which meant a necessary compromise between the particle load and piezoelectric properties. Indeed, when the particle load is increases the piezoelectric coefficient is not only decreased by the reduced volume fraction of the piezo-polymer, but also by the fact that poling of such inhomogeneous samples becomes increasingly difficult. In other words, one cannot simultaneously maximize the pyro/piezoelectric and the SCO outputs, because they are antagonistic. For this reason, in the present work, we consider a 31-mode connectivity composite, which is basically a piezoelectric-SCO bilayer film. This approach provides us the opportunity to optimize the two materials independently. In particular, it becomes possible to employ high SCO particle concentrations to achieve large strains and, simultaneously, the poling of the piezo-polymer becomes straightforward. Using a common polymer matrix, the mechanical coupling of the layers can be readily achieved. As a matter of fact, such bilayer energy harvesting devices have been already reported in the literature, using shape memory alloy (SMA) materials (instead of SCO materials) to generate large thermal strains [7-9]. In most cases, the bilayer was used as a cantilever device, clamped on one or both ends. As an example, the Figure 4.3 shows an

SMA/P(VDF-TrFE) cantilever device displaying electrical output upon both mechanical (finger tapping) and thermal excitations [7].

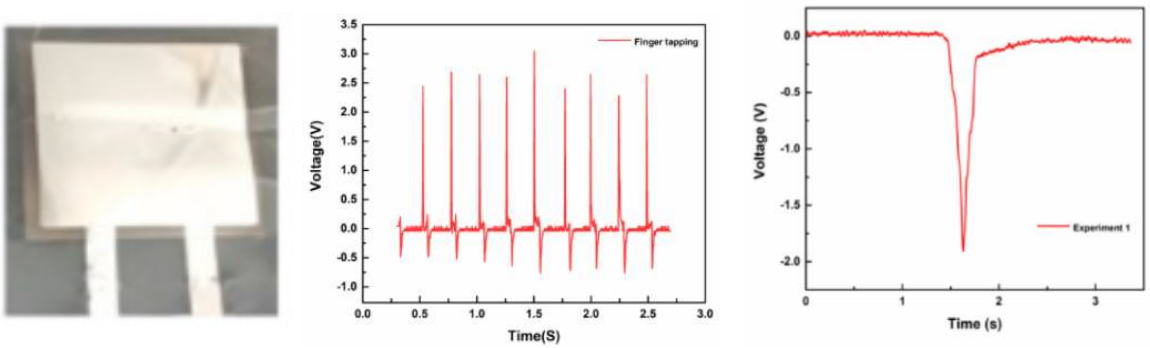

Figure 4.3. *From left to right: Photograph of an SMA/P(VDF-TrFE) multilayer cantilever device and its output voltage under finger tapping as well as thermal loading [7].*

As demonstrated in ref. [8], such devices can provide significant gain over conventional pyroelectric harvesters, provided care is taken to design a device in which the pyro- and piezoelectric effects sum up. In addition, bending cantilever devices provide the measns to not only harvest temporal, but also spatial differences of temperature,e.g. when they are oscillated between a hot and a cold surface [9]. It is worth noting that by downsizing the devices to the micro-scale, the thermalization rate can be significantly increased, resulting in better performance.

4.2. Device fabrication and characterization

Inspired by the above meantioned ideas, and using the fabrication protocols discussed in Chapter 2, we explore below the fabrication of a multilayer cantilever device based on SCO and piezo-polymer materials, aimed for thermal energy harvesting. In the fabrication of the multilayer cantilever structure, we need to prepare three different films by blade casting: an SCO film to transform the thermal energy into mechanical strain, a piezoelectric P(VDF-TrFE) film to transform the mechanical stress into electrical charges and an electrically conducting film, which is then used to harvest the generated charges. The SCO film consists of SCO particles loaded into a P(VDF-TrFE) matrix, whereas the conducting film is made of silver particles embedded in P(VDF-TrFE). We use the same polymer matrix because it is a very efficient way to ensure the good mechanical adhesion between the different films and thus avoid their delamination. In the last step of the fabrication, the different films are hot pressed to form the multilayer cantilever. We fabricated two different cantilever designs (Fig. 4.4), including an asymmetrical variant with 4 layers [Ag@P(VDF-TrFE) / P(VDF-TrFE) / Ag@P(VDF-TrFE) / SCO@P(VDF-TrFE)], where the materials were arranged to enable cantilever bending at the spin transition, and a symmetrical version with 5 layers [SCO@P(VDF-TrFE) / Ag@P(VDF-TrFE) / P(VDF-TrFE) / Ag@P(VDF-TrFE) / SCO@P(VDF-TrFE)], in which the SCO expansion occurs on both sides of the cantilever.

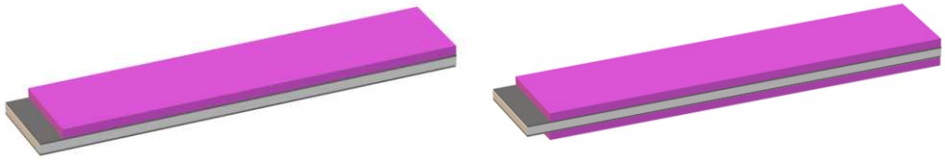

Figure 4.4. *Conceptual representation of the asymmetrical (left) and symmetrical (right) cantilever designs. Colour code: SCO composite (pink), Ag composite (dark grey) and pure P(VDF-TrFE) (light grey).*

For the fabrication of the SCO composite layer, we have chosen the SCO complex $[Fe\{(Htrz)_{1.8}(trz)\}_1(NH_2\text{-}trz)_{0.2}](BF_4)_1\cdot 0.7H_2O$, which was proven to be highly effective for mechanical applications due to its unique properties [10]. First of all, by adjusting the stoichiometry of the compound one can finely tune the spin transition temperature. Secondly, these particles exhibit a needle shape with high aspect ratio (see Fig. 4.5), allowing one to align them in the casting direction during the film making process and thus providing directional-dependent mechanical behavior. Thirdly, they display a significant volume strain, typically around 12 %, which is attained to a large extent along the long axis of the particles (ca. 6 %). This anisotropy makes them particularly advantageous in systems that require large deformation in a specific direction, such as the cantilever structures used in this study. The ability of this material to produce large, directional thermal strain at controllable temperatures makes this material a promising candidate for advanced energy harvesting and actuation technologies.

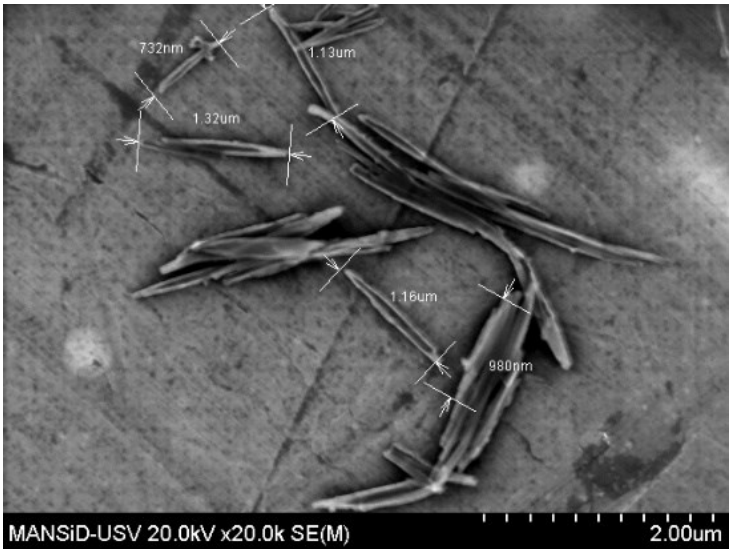

Figure 4.5. *Representative SEM image of the SCO particles $[Fe\{(Htrz)_{1.8}(trz)\}_1(NH_2\text{-}trz)_{0.2}](BF_4)_1\cdot 0.7H_2O$, characterized by ca. 1 μm length and an aspect ratio of ca. 30.*

The piezoelectric material (and common matrix) selected for this study is the $P(VDF_{80}\text{-}TrFE_{20})$ copolymer, which is highly soluble in polar solvents such as acetone and butanone. As already mentioned in Chapter 2, this specific copolymer ratio was chosen because its Curie temperature is significantly higher than the spin transition temperature of the SCO material

used. Indeed, as shown in the DSC thermogram in Figure 4.6, the 80/20 proportion of vinylidene fluoride (VDF) and trifluoroethylene (TrFE) ensures a stable ferroelectric phase up to ca. 136 °C. This is to be compared with the low-spin to high-spin transition temperature of the SCO material, which is ca. 85 °C. This large difference in transition temperatures provides a comfortable thermal window for experiments, allowing us to fully bring the SCO complex into the HS form, without risking depolarization of the piezoelectric material. Achieving the highest actuation effect requires the highest possible SCO load. In our preliminary tests, we established an optimal concentration of 25 % of the SCO material. (N.B. This refers to a concentration both by mass and by volume, since the densities of the polymer matrix and the SCO filler are comparable, ca. 1.9 ± 0.1 g/cm^3.) Indeed, we observed that exceeding a particle concentration of 30 % adversely affected the mechanical properties of the composite, rendering it brittle, and incapable of withstanding the bending forces experienced by the cantilever. This brittleness made it unsuitable for practical applications in the context of the present work. Conversely, reducing the amount of SCO material below 25 % diminished the actuation effect, which was undesirable for the intended functionality.

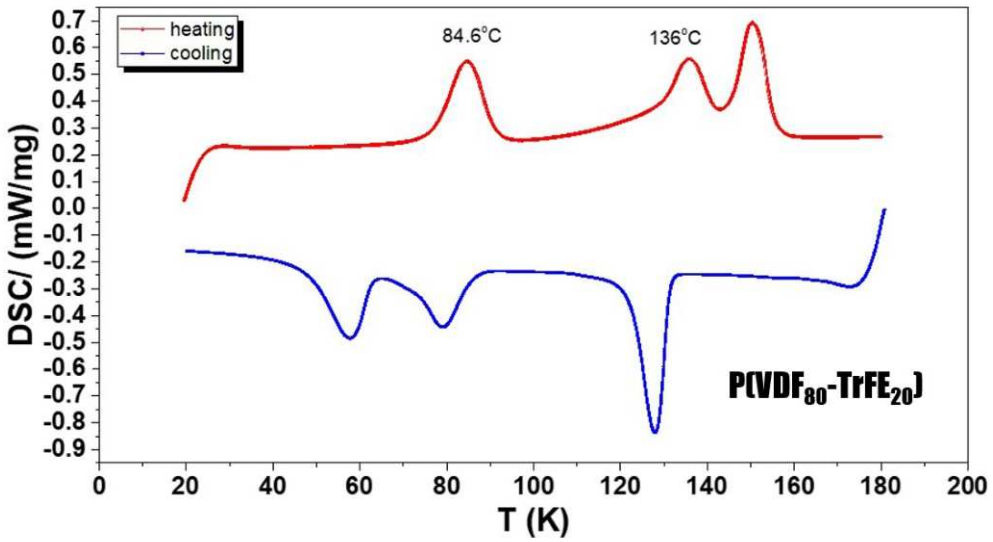

Figure 4.6. *Calorimetric measurement on the [Fe{(Htrz)$_{1.8}$(trz)}$_1$(NH$_2$-trz)$_{0.2}$](BF$_4$)$_1$·0.7H$_2$O@P(VDF$_{80}$-TrFE$_{20}$) composite (25 vol%). The SCO and Curie transitions occur on heating at ca. 85 °C and 136 °C, respectively. The third peak is associated with the melting of the polymer near 150 °C.*

To fabricate the SCO composite film, a solution was prepared using butanone as the solvent, chosen for its ability to dissolve the copolymer effectively, and for slow evaporation that prevents the formation of bubbles, which would compromise the quality of the casted layer. Specifically, 80 mg of SCO particles were combined with 240 mg of P(VDF$_{80}$-TrFE$_{20}$) copolymer, and 1.6 ml of butanone was added to achieve an optimal viscosity suitable for the blade casting technique. To ensure a homogeneous distribution of particles within the solution, the SCO particles were first dispersed in the solvent and sonicated for approximately 5 minutes to break up any potential agglomerates. After sonication, the P(VDF$_{80}$-TrFE$_{20}$) powder was added to the mixture. The solution was then stirred using a magnetic stirrer for at least 30 minutes.

Initially, a high stirring speed of around 1000 rpm was employed to accelerate the dissolution of the polymer. In the final 10 minutes, the stirring speed was reduced to less than 150 rpm to minimize the formation of air bubbles. The decreased agitation allowed bubbles to accumulate and rise to the surface of the solution, facilitating their removal prior to the casting process. This careful preparation ensured that the composite material possessed the necessary mechanical integrity and uniformity for effective mechanical actuation.

In order to effectively polarize the piezoelectric polymer within the cantilever device and efficiently harvest the generated charges, it is essential to select electrode materials that are compatible with the piezo-polymer. This compatibility ensures that the layers within the bending cantilever do not delaminate. Moreover, to prevent losses in currents, the chosen material should exhibit high conductivity. An ideal candidate that satisfies these requirements is a composite of silver particles and P(VDF-TrFE), which combines the desired electrical and mechanical properties. Determining the optimal concentration of silver particles in the polymer is an important task. The concentration needs to strike a balance between achieving good conductivity and maintaining satisfactory mechanical properties. To address this issue, a study was conducted involving the fabrication of 12 samples, divided into two categories characterized by concentration and thickness. Based on previous knowledge from a similar project involving the composite as an electrical heater for an artificial muscle [10], it is known that the percolation threshold, where the material exhibits significant electrical conductivity, occurs at around 50 wt.% silver concentration. However, to achieve a very high conductivity, two higher concentrations were also tested 66 wt.% and 80 wt.%. For each concentration, four films with varying thicknesses were fabricated. The electrical resistance of each sample was measured and, by considering their respective shape parameters, the resistivity was calculated. Figure 4.7 displays the relationship between resistivity, layer thickness, and silver concentration in the composite.

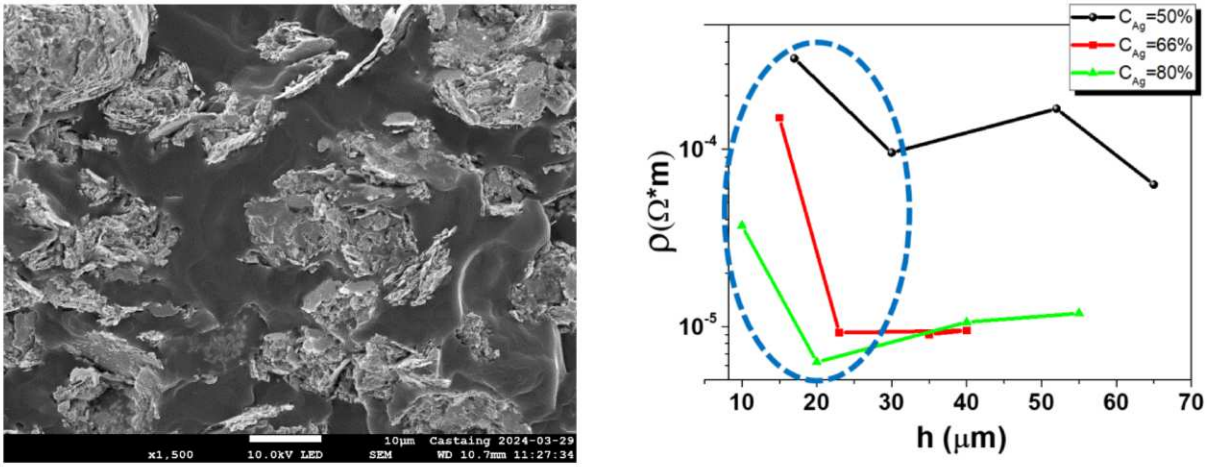

Figure 4.7. *Left: SEM image of the silver particles used. Right: Electrical resistivity as a function of the thicknesses of the Ag@P(VDF-TrFE) film for three different concentration of silver particles (per weight). The resistivity should be independent of the film thickness, but below a critical thickness it shows a strong dependence (blue ellipse region).*

One of the requirements for the electrodes in the cantilever device is to have minimal impact on the movement of the device. This entails making the electrodes as thin as possible. However, it is also crucial to maintain a suitable thickness that does not compromise conductivity. Analyzing the graph, it is evident that the resistivity remains relatively constant with incresing thickness. Notably, both the 66% and 80% silver concentrations exhibit comparable resistivity values that are lower than the resistivity at 50% concentration. However, at thicknesses below 20 μm, the resistivity values sharply increase. This can be attributed to approaching the size of the silver flakes within the composite. As the layers become thinner, inhomogeneities arise within the composite, and there is less contact between the particles.

Overall, the findings indicate that a balance between thickness and conductivity is essential. It is preferable to choose a thinner layer thickness to minimize the impact on device movement, while ensuring that the thickness is sufficient to maintain good conductivity. Additionally, careful consideration should be given to the silver concentration, as both the 66 % and 80 % concentrations offer comparable and lower resistivity values compared to the 50 % concentration.

Each film was fabricated using the blade casting technique described in Chapter 2. In order to control the thickness of the dry layer there are two main parameters to consider, which are the viscosity of the suspension and the height of the blade. The viscosity is given by the amount of solvent used for the preparation of each suspension. The blade height was 1.500 mm for both the pure P(VDF-TrFE) and for the SCO@P(VDF-TrFE) films, whereas it was reduced to 0.300 mm in the case of the Ag@P(VDF-TrFE) film. The casting was performed on a glass substrate with its surface heated to ca. 35 °C. The resulting films are pictured in Figure 4.8. In order to adhere the layers in the required multilayer cantilever configuration, the films were then hot pressed together and poled using the methods described in Chapter 2 and, finally, the silver layers were connected to copper wires using a conductive glue. A representative SEM image of an asymmetric device is shown in Figure 4.9, revealing well defined and densely packed layers.

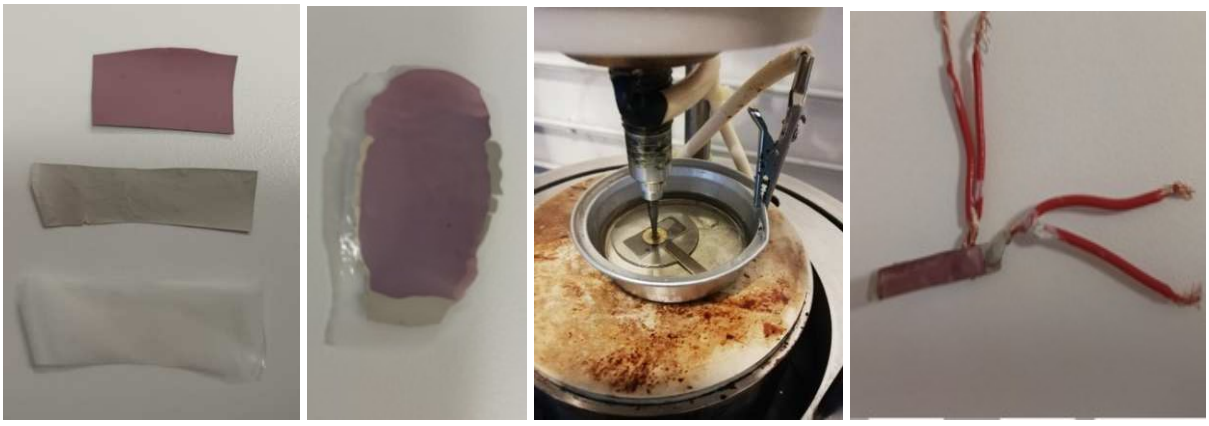

Figure 4.8. *Photographs of the last stages of the device fabrication. Left: The three casted layers after drying. Middle-left: Multilayer stack after hot pressing. Middle-right: Film polarization. Right: The cantilever device with the connected electrodes for harvesting measurement.*

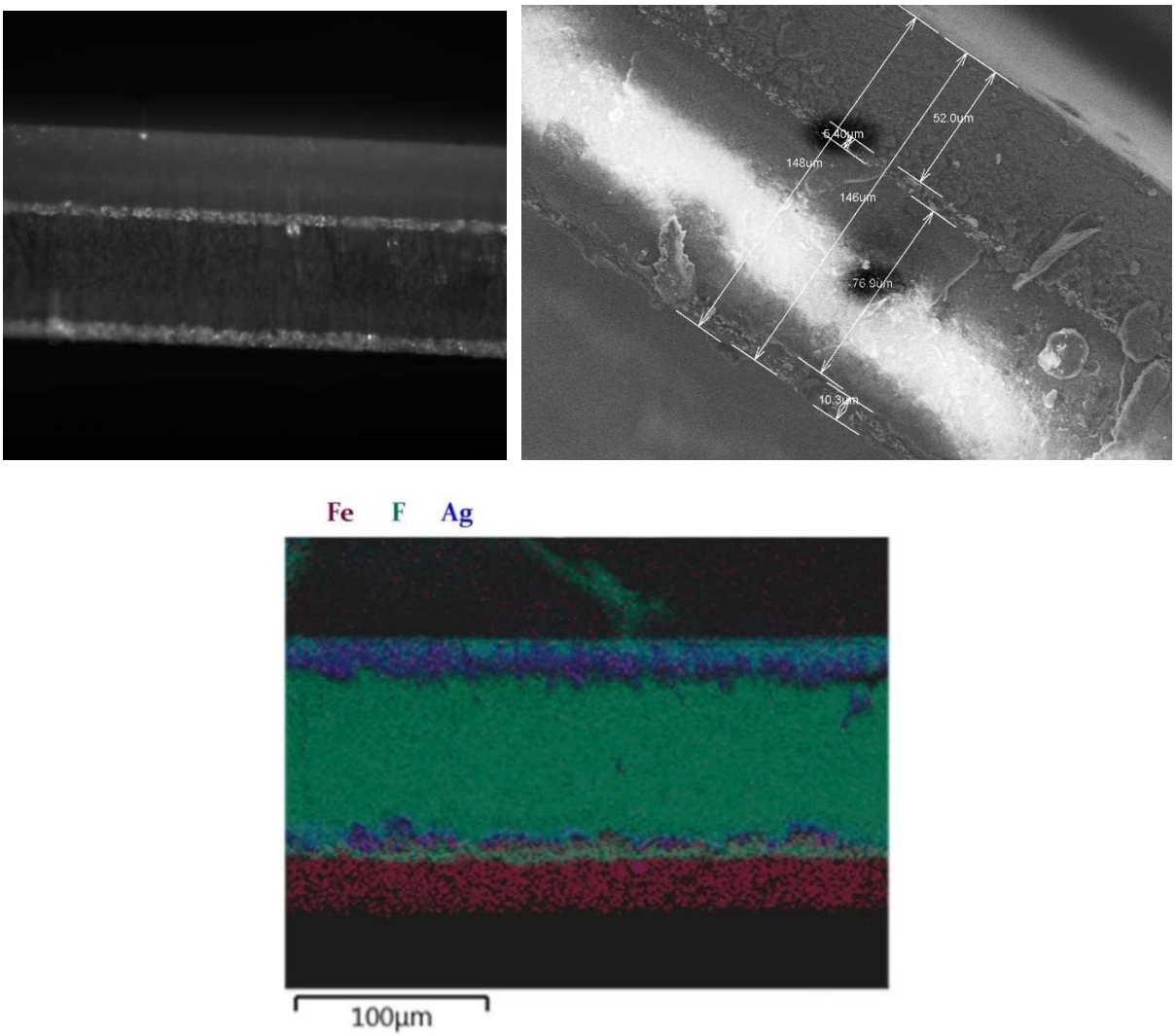

Figure 4.9. *SEM images of a 4-layer (asymmetric) cantilever device cross-section clearly revealing a ca. 52 µm thick SCO@P(VDF-TrFE) layer and a ca. 77 µm thick P(VDF-TrFE) layer, the latter being sandwiched between two, ca. 6-10 µm thick, Ag@P(VDF-TrFE) layers(top). The EDX image of an asymmetrical cantilever that shows the distribution of the materials in the layers (bottom).*

To investigate the thermomechanical properties of each layer we conducted a Dynamical Mechanical Analysis (DMA) in tension mode as a function of the temperature. The storage moduli of the films, which can be roughly assimilated with their Young's moduli, as a function of temperature, are illustrated in Figure 4.10 (top panel). The neat polymer shows a room temperature storage modulus of ca. 600 MPa, which monotonously decreases upon heating to a value of ca. 80 MPa at 100 °C. As it can be expected, the silver doped P(VDF-TrFE) composite is significantly reinforced with a room temperature modulus of ca. 3.2 GPa, which softens to ca. 1.1 GPa at 100 °C. The reinforcement of the SCO doped P(VDF-TrFE) is similar: the modulus reaches 3.1 GPa at room temperature and 1.4 GPa at 100 °C. Interestingly, the temperature dependent behavior of the storage modulus of this sample shows clear signatures of the spin transition at about 90 °C in heating and at 55 °C in cooling. These anomalies correspond to the elastic softening of the sample due to the sensitivity of the spin

state equilibrium to the applied mechanical stress [11]. These anomalies of the elastic modulus at the SCO are concomitant with pronounced damping peaks seen in the loss tangent behavior (Fig. 4.10). Importantly, we observe excellent mechanical actuation in the SCO composite with a strain of ca. 3% at the spin transition, which translates into thermal expansion peaks of the order of 2000 ppm/°C (Fig. 4.10).

The piezoelectric coefficient of the poled samples was measured using the piezometer (Piezotest PM200) described in Chapter 2, which directly measures the piezoelectric coefficient in the 33 mode (d_{33}). For each sample, we obtained reasonably high values of d_{33}, between ca. -15-20 pC/N, which is comparable with values reported in the literature [12]. It is, however, important to notice that for the cantilever device the relevant piezoelectric property is the 31 mode (see Figure 4.11). Since we had no means to measure this coefficient, we can just say, based on the literature data [13], that the value of d_{31} should be the same order of magnitude as d_{33}, but with opposite sign, i.e. on the order of +10 pC/N.

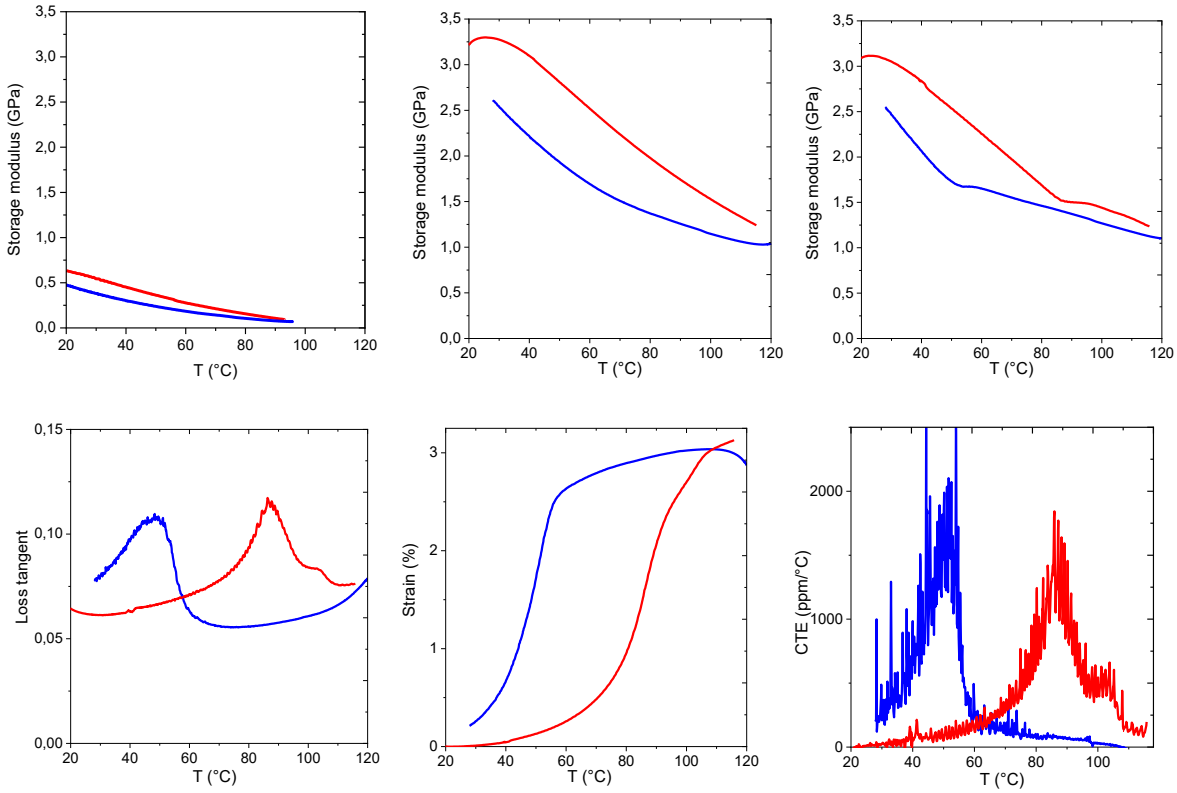

Figure 4.10. *Storage modulus measured in heating and cooling modes (3 K/min, 1 Hz, amplitude 20 μm, constant 1.5:1 ratio of static force and dynamical force amplitude) for a hot pressed layer of the pure P(VDF-TrFE) film (top, left), a 66 wt.% Ag@P(VDF-TrFE) composite film (top, middle) and a 25 wt% SCO@P(VDF-TrFE) composite film (top right). For the SCO composite the loss tangent, strain and coefficient of thermal expansion (CTE) are also shown as a function of the temperature.*

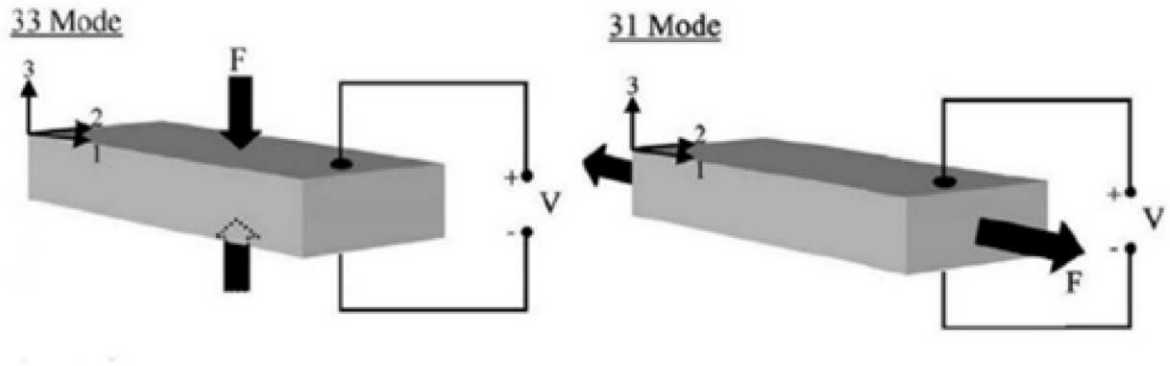

Figure 4.11. *Schematic images showing the piezoelectric modes 33 (both electric voltage and mechanical force are normal to the film surface) and 31 (V is out-of-plane, but F is in-plane, along the beam axis). In this two-subscript notation, we identify length (1), width (2) and thickness (3). The first number indicates the electrical poling axis, which is usually the thickness (3) direction, whereas the second number denotes the axis of mechanical stress.*

4.3. Harvesting experiments

For an initial assessment of the piezoelectric response of the fabricated devices we conducted simple finger pressing experiments, wherein a Keithley 6430 electrometer was used to measure the current generated from the device. A typical result is displayed in Figure 4.12, showing that during finger pressing a few nA current is generated form the device. Under mechanical stress a potential difference develops between the top and bottom electrodes due to the change of polarization in the P(VDF-TrFE) layer. (N.B. It is possible that the SCO@P(VDF-TrFE) layer contributes also to the overall polarization, but this contribution must be relatively minor.) In short-circuit configuration, this leads to electrons flowing between the electrodes, which is manifested by the (negative) current peak. When the stress is released a current peak of opposite sign is observed due to the decrease of the potential and associated discharging. This phenomenon could be repeatedly observed.

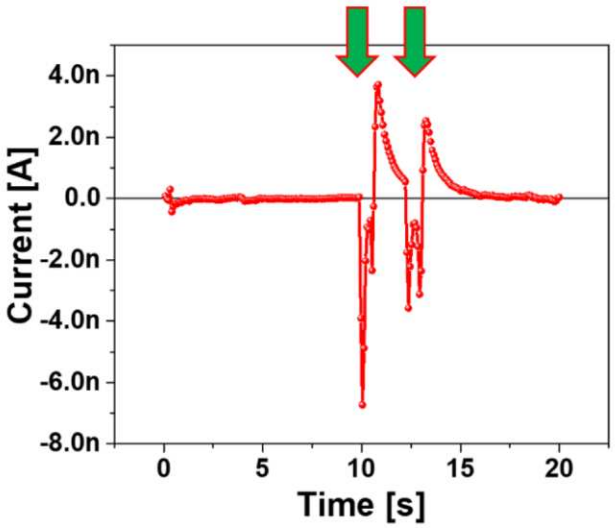

Figure 4.12. *Piezo current generated by finger pressing the cantilever. The green arrows indicate the two finger pressing events.*

In the next step, we placed the harvester device into an oil bath, whose temperature was varied between ca. 30 and 110 °C using a Linkam THMS600 heating-cooling stage (see Fig. 4.13). The current generated from the device upon heating-cooling was measured using a Keithley 6430 electrometer (under zero external bias). The bending movement of the free end of the single-clamped, asymmetric cantilever was recorded without electrical leads in order to minimize the impact of external loads. Figure 4.13 (bottom panel) displays photographs acquired during the heating of a device. One can notice an initial downward bending, caused by the mismatch of thermal expansion of the different layers, followed by a spectacular upward bending on further heating, which can be associated with the SCO phenomenon. This movement was reversible through several thermal cycles.

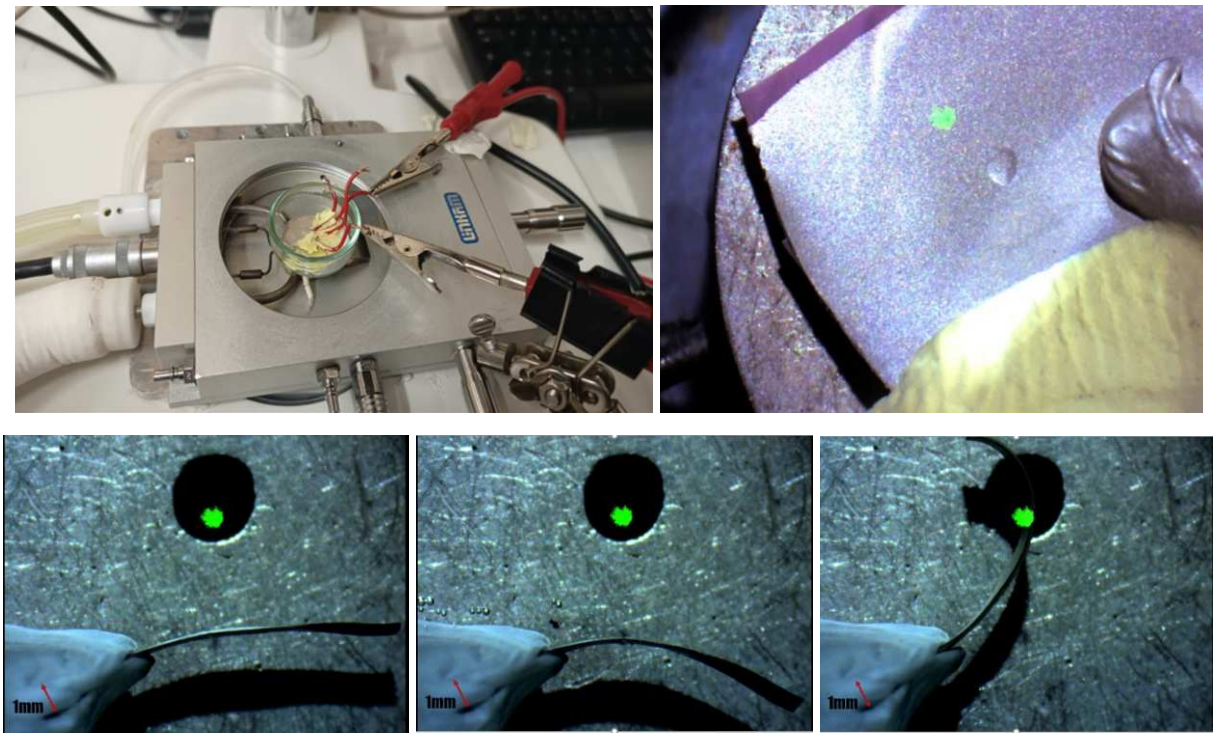

Figure 4.13. *Top left: Measurement setup with the heated oil bath. Top right: Microscope image of the symmetrical cantilever in the oil bath. Bottom panel: Microscope images of the asymmetrical cantilever at different temperatures (in the heating mode). From left to right: 30 °C, 70 °C and 110 °C.*

The first measurements were conducted using the symmetrical device, which is easier to handle, as it does not move considerably during the thermal cycles. Figure 4.14 shows a pyrocurrent measurement results on a five layer device heated and cooled in the oil bath at rates of 5 °/min and 3 °C/min respectively. The first thermal cycles being always somewhat anomalous, the figure shows the data acquired during the second thermal cycles. Before the measurements the sample was poled and a piezoelectric charge coefficient, d_{33}, of -15 pC/N was reached. Parallel to the electrical measurement, we have also recorded the temperature dependence of the optical reflectivity of the device, which provides a straightforward means to detect the spin transition through the colour change of the uppermost SCO layer. First of all, the device exhibits a clear pyroelectric response upon thermal cycling, which is manifested by

the change of sign of the pyro-current between heating and cooling, as well as by the increase of the pyro-current when increasing the temperature scan rate. Indeed, both observations are in line with Eq. 4.1. Remarkably, in the cooling mode one can depict an obvious anomaly in the current vs. temperature curve near 70-73 °C (indicated by a vertical red line in Fig. 4.14), which coincides with the high spin to low spin transition, detected through the colour change of the sample. In the heating mode, no obvious correlation between the SCO phenomenon and the pyro-current curves can be drawn, which is probably linked to the fact that the spin transition occurs at the very end of the thermal cycle. On the whole, we can conclude that the device exhibits pyro-electric behaviour as well as a thermal to electrical energy conversion linked to the SCO phenomenon. Unfortunately, the two phenomena do not sum up, but instead they oppose each other.

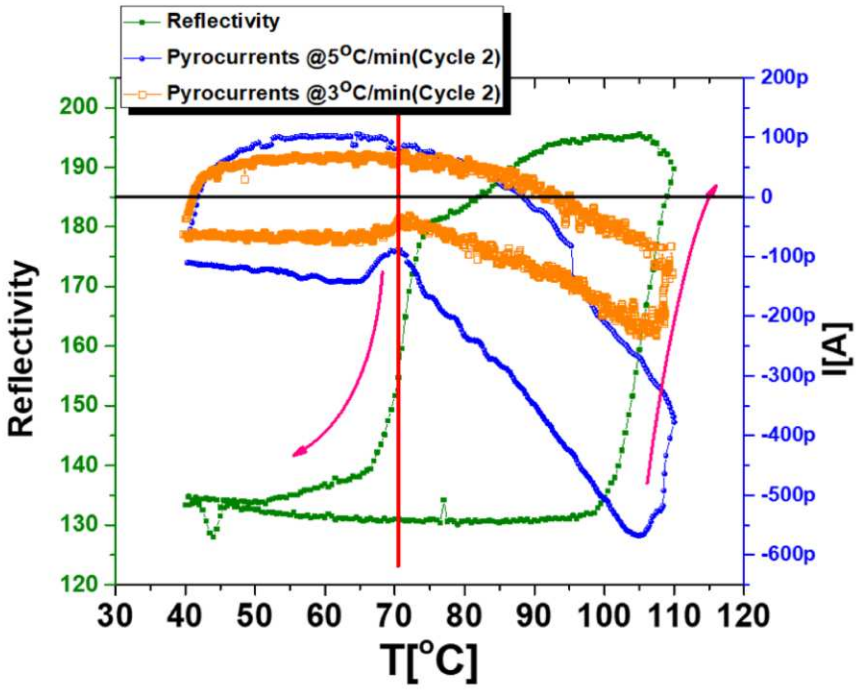

Figure 4.14. *Short-circuit current (U = 0 V) acquired upon thermal cycling a 5 layers symmetrical (SCO/Ag/PE/Ag/SCO) device at rates of 5 °C/min (blue) and 3 °C/min (orange). Prior to the measurements the piezoelectric (PE) layer was poled to reach a d_{33} of -15 pC/N. The green curve shows the simultaneously recorded optical reflectivity of the device.*

At this point, one must note that the spin transition temperature measured in different experiments, such as calorimetry (Fig. 4.6), DMA (Fig. 4.8), and pyro-current measurements (Fig. 4.14) are not the same. We believe this is related to the rather different sample thermalization conditions involved in these different measurement setups, leading to significant thermal lags. Nevertheless, the identification of the SCO event in each experiment is unequivocal. We have repeated the experiment shown in Fig. 4.14 on a similar symmetrical device, fabricated using similar protocols. The characterization of this device, shown in Figure 4.15, fully confirmed the results obtained with the first device. Besides an obvious and well reproducible pyro-current, one can depict again a discharge peak at the spin transition. For this

second device, not only the cooling (near 75 °C), but the heating curve (near 105 °C) shows also this effect.

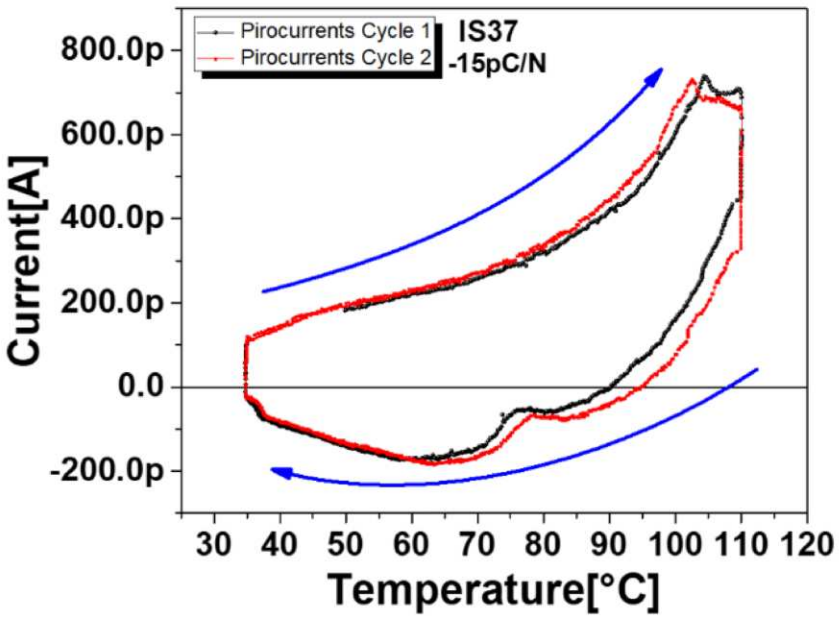

Figure 4.15. *Short-circuit current (U = 0 V) acquired upon two successive thermal cycles for a 5 layers symmetrical (SCO/Ag/PE/Ag/SCO) device. Prior to the measurements the piezoelectric (PE) layer was poled to reach a d_{33} of -15 pC/N.*

In the next step, we have thus turned our attention to the asymmetrical, bending cantilever device, whose properties are displayed in Figure 4.16. This device also displays clear-cut and well reversible pyro-electric properties, in line with the high piezoelectric charge coefficient (-20 pC/N) we could achieve. Remarkably, in this case, we observed two current discharge peaks in the cooling mode near 100 °C and 60 °C, which have the same sign as the pyro-current. In addition, we observed a reproducible, although very noisy, current anomaly in the heating mode near 85 °C. Due to the significant movement of this device it was unfortunately not possible to record the colour change in situ and the assignment of the current peaks/anomalies remains in this case uncertain. Nevertheless, we can suggest that those near 60 °C in cooling and 85 °C in heating correspond to the HS→LS and LS→HS spin transitions, respectively.

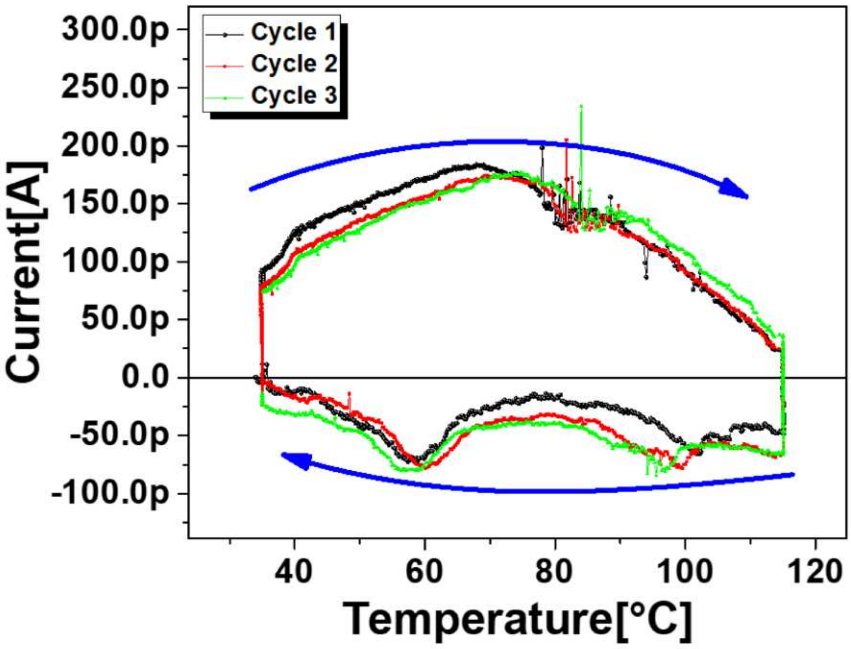

Figure 4.16. *Short-circuit current (U = 0 V) acquired upon three successive thermal cycles for a 4 layers asymmetrical (SCO/Ag/PE/Ag) device. Prior to the measurements the piezoelectric (PE) layer was poled to reach a d_{33} of -20 pC/N.*

4.4. Discussion

These different experimental observations can be discussed by taking into account the sign of the output current (or voltage) for both the piezoelectric and pyroelectric effects, which must be obviously the same in order to maximize the output. P(VDF-TrFE) copolymers, depending on the exact ratio of monomers as well as on the sample preparation conditions (annealing temperature, etc.), display a pyroelectric coefficient (p) of ca. +40 $\mu Cm^{-2}K^{-1}$ [14], whereas the relevant piezoelectric charge coefficient (d_{31}) reaches typically values of +10 pC/N [13], i.e. both coefficients have a positive sign. This means that upon heating (resp. cooling) a pyrocurrent of positive (resp. negative) sign is generated. On the other hand, the sign of the current generated by the piezoelectric effect will depend on the nature of the stress (i.e. compressive or tensile), which arises in the piezoelectric layer upon therml cycling. For the sign convention, the polarity of the applied poling voltage serves as the reference for the electrical voltage/current polarity. The numbering system for the electrical and mechanical field directions is shown in Fig. 4.11. From this convention, and taking into account the positive sign of the piezoelectric coefficient d_{31} of our piezo-polymer, it appears that a positive (resp. negative) stretching (resp. compressive) stress in the axial (1) direction will give rsie to an electrical response of opposed (resp. same) polarity, with respect to the polarity of the poling voltage, in the out-of-plane (3) direction. In the case of the symmetric device, upon heating, the expansion of the external SCO layers gives rise to a tensile stress within the piezoelectic middle layer in the axial direction. This explains why we observed in our experiments pyroelectric and piezoelectric current outputs with opposed polarity, i.e. a current dip instead of a current peak (see Fig. 4.14 and 4.15). In the case of the asymmetrical (bending) device, the situation is more

complicated, as the piezoelectric layer may be either under compression or under tension or even in a mixed, partially compressed and partially stretched, state. The distribution of stress and strain along the height of a bimorph beam is schematically shown in Fig. 4.17. (Note that here we neglect the impact of the electrode layers, which might be not negligible – vide infra.) On heating, the LS→HS transition in the bottom SCO layer leads to its expansion, which is maximal at the bottom surface. On the other hand, the piezoelectric (PE) top layer displays negligible thermal strain, but due to the mechanical coupling to the SCO layer, the beam bends and the PE layer suffers a compression, which is maximal at the top surface. The compressed and stretched regions are separated by a neutral layer, which does not necessarily coincides with the interface between the two materials [15]. As a mater of fact, due to the very large strain in the SCO layer, the expectation is that the neutral layer will be somewhere within the piezoelectric film. This means that part of the film will be under compression and another part under tension, which is obviously not a desirable situation, because the piezoelectric effects generated in these two regions will cancel each other out. It is also important to note that the axial strain (ε_x) varies linearly from the highest tension (at the bottom) to the highest compression (on the top), but the axial stress (σ_x) shows a discontinuity at the interface of the two materials because of their different Young's modulus. (N.B. Ultimately, this difference of stress at the interface might lead to delamination if the adhesion between the two layers is not enough strong.) From this simplified mechanical picture it becomes clear that the experimentally observed current peaks in the asymmetrical device and current dips in the symmetrical device are related to the sign of the averaged mechanical stress (σ_x) in the PE layer, mostly compressive in the former and tensile in the latter.

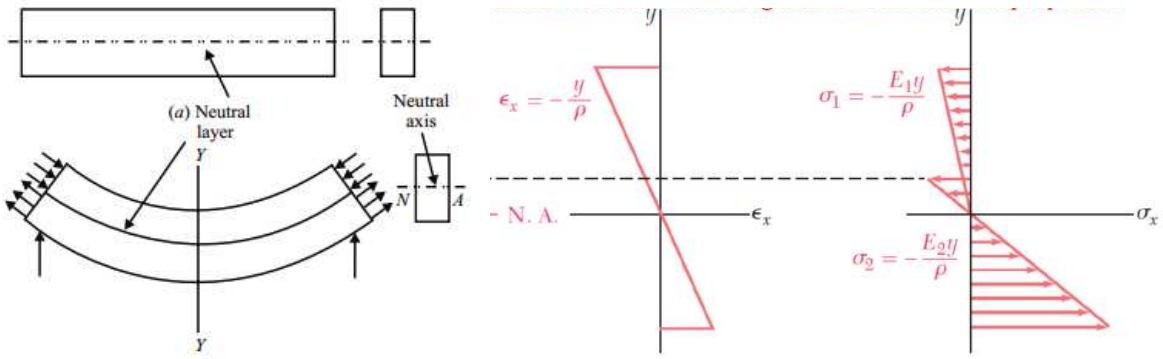

Figure 4.17. *Schematic axial stress and strain distribution across the height for a bending bilayer beam.*

4.5. Conclusions and perspectives

In summary, we have fabricated a multilayer cantilever device combining a pyroelectric polymer layer with a spin crossover-polymer composite layer, complemented by two electrically conducting composite layers. We designed this 31 type composite device with the aim to overcome the drawbacks of previously investigated 33 connectivity SCO@PE particulate composites, aimed for thermal energy harvesting purposes. Indeed, the separation of the two materials allowed us to optimize both the SCO strain, which reached 3 %, and the PE d_{33} coefficient, which was as high as -20 pC/N. We have hot pressed both symmetrical

devices (showing no bending motion) and asymmetrical ones, displaying large, reproducible deflections upon thermal cycling. Each device displayed significant piezo-currents upon finger tapping and pyro-currents in response to temperature changes. Most importantly, each device displayed clear anomalies of the pyro-current at the spin-transition temperature, providing proof for an extra piezoelectric charge generation due to the SCO actuation. Remarkably, the sign of these piezo-current anomalies was found to be the same (resp. opposite) as the sign of the ordinary pyro-current in the asymmetric (resp. symmetric) device, which we could attribute to the different sign of the mechanical stress generated in the two devices (compressive vs. tensile). Based on this proof of concept, further work should focus on the optimization of the device configuration (i.e. thickness and Young's modulus of the different layers) in order to bring the entire PE layer into compression and thus maximize the piezoelectric output. Alternatively, one can also envision the use of a different PE material (e.g. a polymer composite of $BaTiO_3$), which displays opposite PE effect when compared to the piezo-polymer, P(VDF-TrFE), used in the present work. In that case, device engineering should aim at bringing the PE layer fully under tension. Following this optimization, it will be important to quantify the harvesting properties and figures of merits in order to compare them with existing technologies.

References

[1] Habib, M., Lantgios, I., & Hornbostel, K. (2022). A review of ceramic, polymer and composite piezoelectric materials. Journal of Physics D: Applied Physics, 55(42), 423002, 10.1007/978-1-4615-3818-9_19.

[2] He, H., Lu, X., Hanc, E., Chen, C., Zhang, H., & Lu, L. (2020). Advances in lead-free pyroelectric materials: a comprehensive review. Journal of Materials Chemistry C, 8(5), 1494-1516, 10.1039/C9TC05222D.

[3] Bowen, C. R., Taylor, J., LeBoulbar, E., Zabek, D., Chauhan, A., & Vaish, R. (2014). Pyroelectric materials and devices for energy harvesting applications. Energy & Environmental Science, 7(12), 3836-3856, 10.1039/C4EE01759E.

[4] Rat, S., Piedrahita-Bello, M., Salmon, L., Molnár, G., Demont, P., & Bousseksou, A. (2018). Coupling mechanical and electrical properties in spin crossover polymer composites. Advanced Materials, 30(8), 1705275, 10.1002/adma.201705275.

[5] Piedrahita-Bello, M., Martin, B., Salmon, L., Molnár, G., Demont, P., & Bousseksou, A. (2020). Mechano-electric coupling in P (VDF–TrFE)/spin crossover composites. Journal of Materials Chemistry C, 8(18), 6042-6051, 10.1039/D0TC00780C.

[6] Angulo-Cervera, J. E., Piedrahita-Bello, M., Martin, B., Dantras, E., Nicu, L., Leichle, T., ... & Bousseksou, A. (2022). The crystallinity and piezoelectric properties of spray-coated films of P (VDF 70-TrFE 30): effects of film thickness and spin-crossover nanofillers. Journal of Materials Chemistry C, 10(21), 8466-8473, 10.1039/d2tc01162j.

[7] Sukumaran, S., Chatbouri, S., Badie, L., Thiebaud, F., Ben Zineb, T., & Rouxel, D. (2023). Processing of hybrid shape memory alloy coupled with P (VDF-TrFE) piezoelectric polymer composite for energy harvesting application. Journal of Intelligent Material Systems and Structures, 34(5), 595-608, 10.1177/1045389X221111550.

[8] Gusarov, B., Gusarova, E., Viala, B., Gimeno, L., Boisseau, S., Cugat, O., ... & Louison, B. (2016). Thermal energy harvesting by piezoelectric PVDF polymer coupled with shape memory alloy. Sensors and Actuators A: Physical, 243, 175-181, 10.1016/j.sna.2016.03.026.

[9] Hunter, S. R., Lavrik, N. V., Mostafa, S., Rajic, S., & Datskos, P. G. (2012). Review of pyroelectric thermal energy harvesting and new MEMs-based resonant energy conversion techniques. Energy harvesting and storage: materials, devices, and applications III, 8377, 77-90, 10.1117/12.920978.

[10] Piedrahita-Bello, M., Angulo-Cervera, J. E., Enriquez-Cabrera, A., Molnár, G., Tondu, B., Salmon, L., & Bousseksou, A. (2021). Colossal expansion and fast motion in spin-crossover@ polymer actuators. Materials Horizons, 8(11), 3055-3062, 10.1039/d1mh00966d.

[11] Alavi, S. E., Martin, B., Zan, Y., Yang, X., Piedrahita-Bello, M., Nicolazzi, W., ... & Bousseksou, A. (2023). Dynamical Mechanical Analysis and Micromechanics Simulations of Spin-Crossover@ Polymer Particulate Composites: Toward Soft Actuator Devices. Chemistry of Materials, 35(8), 3276-3289, 10.1021/acs.chemmater.3c00293.

[12] Zhang, L., Li, S., Zhu, Z., Rui, G., Du, B., Chen, D., ... & Zhu, L. (2023). Recent progress on structure manipulation of poly (vinylidene fluoride)-based ferroelectric polymers for enhanced piezoelectricity and applications. Advanced Functional Materials, 33(38), 2301302, 10.1002/adfm.202301302.

[13] Humphrey, K. J., Garner, G. M., & Whatmore, R. W. (1987). The dielectric and piezoelectric properties of vinylidene fluoride-trifluoroethylene copolymers. Ferroelectrics, 76(1), 383-391, 10.1080/00150198708016959.

[14] Zhang, Q. Q., Chan, H. L. W., & Choy, C. L. (1999). Dielectric and pyroelectric properties of P (VDF-TrFE) and PCLT–P (VDF-TrFE) 0–3 nanocomposite films. Composites Part A: applied science and manufacturing, 30(2), 163-167, 10.1016/S1359-835X(98)00113-4.

[15] Shapiro, B., & Smela, E. (2007). Bending actuators with maximum curvature and force and zero interfacial stress. Journal of intelligent material systems and structures, 18(2), 181-186, 10.1177/1045389X06063801.

Chapter 5. Novel Approaches for Electrical Sensing of Molecular Spin State Switching in Spin Crossover Materials

In this chapter, we discuss two unprecedented approaches for the electrical sensing of the spin state switching in SCO@polymer composites. A first approach uses a strain sensor, made of Ag@P(VDF-TrFE), which is attached to the SCO@polymer layer and which works on the basis of percolation effects (section 5.1). In a second part, we introduce a novel approach to study the properties of spin crossover molecular materials using a radio-frequency (RF) resonant tunnel diode oscillator (TDO) circuit (section 5.2).

5.1. Spin transition sensing in percolation devices

5.1.1. Introduction to percolation based strain sensors

The percolation threshold is a property of a composite system where an insulating matrix containing particles reaches a concentration where long-range electrical connections form through the material. For conductive particles, this connection significantly impacts the material's overall conductivity. Notably, the relationship between conductivity and particle concentration is not linear, exhibiting a step-like behaviour [1]. At low concentrations, the lack of particle contacts results in low conductivity, while at high concentrations, abundant particle contacts lead to high conductivity. Between these regions, a sharp change in conductivity, known as the percolation transition, occurs. The relationship between conductivity and mechanical properties at the percolation threshold allows for these composites to be used in sensor applications. The sensitivity of particle contacts to stretching can be exploited to create strain sensors [2]. Additionally, incorporating optically active polymers mixed with Au nanoparticles enables modulation of the percolation transition with light irradiation, facilitating the fabrication of photoresistors [3]. Spin crossover (SCO) materials, which respond to external stimuli, offer intriguing possibilities for modulating resistance through spin transitions. The interaction of SCO materials with conductive polymers can significantly change resistance or conductance with temperature-dependent spin states, showing a substantial difference of approximately 2000% between the two states [4]. For this type of interaction, conductivity typically increases in the high-spin (HS) state. However, in our study, we expect a decrease in conductivity during the HS state, attributed to the expansion of the SCO material, which we expect will reverse the system backwards the percolation threshold. This anticipated behaviour underscores the dynamic interplay between particle concentration and conductive pathways, offering new insights into the design and application of responsive composite materials.

5.1.2. Percolation device fabrication

In tour study we embark on an innovative exploration to modulate the electrical resistance of sandwich-structured devices by mechanically stretching the embedded silver particles by expansion of the spin crossover (SCO) materials. These sandwich type devices are engineered with a tri-layer configuration to harness the property of SCO materials of volume expansion due to spin state change in response to temperature change. The core of our device is a composite middle layer, consisting of silver (Ag) flakes dispersed within a polymer matrix

of poly(vinylidene fluoride-co-trifluoroethylene), denoted as P(VDF_{80}-$TrFE_{20}$). We experimented with various concentrations of Ag flakes in the composite to verify concentration effect on the electrical conductivity of the middle layer. The two outer layers are composed of a blend of 25% spin crossover (SCO) material and 75% P(VDF_{80}-$TrFE_{20}$).

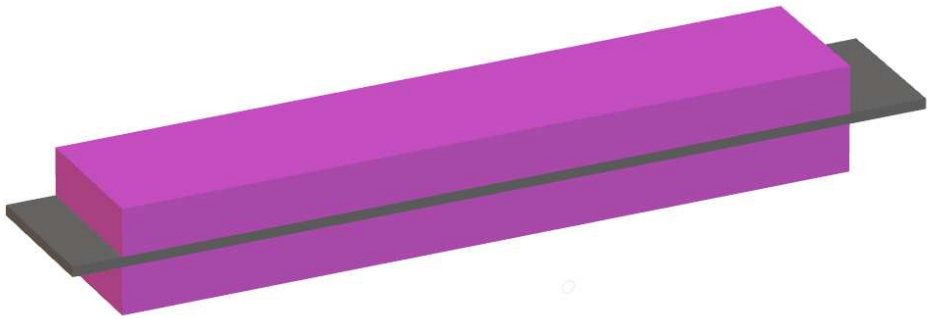

Figure 5.1. *The sandwich like device used for the study of SCO transition impact on electrical resistance. The gray (purple) layer represents Ag (SCO) composites.*

By integrating SCO materials into the composite structure, we aim to investigate how the electrical resistance of the sandwich device is influenced by the spin state of the SCO material. Specifically, we are interested in understanding the relationship between the resistance and the spin state under varying temperatures. Such understanding enables the development of advanced devices with potential applications in sensors and switches, where modulating electrical properties through mechanical means offers a new dimension of control within temperature change. For the electrode layer of the devices we explored silver with mass concentrations of 55%, 60% and 65% as we know the percolation threshold is in the region of 50-55 % [5].

Using blade casting we produced four membranes of differing thicknesses for each of the concentration to examine the interplay between resistivity, silver concentration, and material thickness. To fabricate the sandwich-like device, we followed several steps. Firstly, we prepared the composite solutions, ensuring a uniform mixture of the materials. Next, we cast thin films using the blade cast technique, which provides a controlled and consistent thickness across the film, followed by the use of a hot press to bond the films. The hot press process secures strong adhesion between the layers which prevents delamination, ensuring the integrity and durability of the device. For the SCO composite we used a similar as previously made solution of [Fe[(Atrz)(Htrz)(trz)]BF_4] + P(VDF_{80}-$TrFE_{20}$) in methyl-ethyl-ketone (MEK). 80 mg of [Fe[(Atrz)(Htrz)(trz)]BF_4] anisotropic particles, synthesized at the "Laboratoirre de Chimie de Coordination" (LCC), were added in a 10 ml beaker with 1.6 ml of MEK. The beaker was then sealed with parafilm and the mix was sonicated for 15 minutes foe even distribution of particles in solvent. Meanwhile, 240 mg of P(VDF_{80}-$TrFE_{20}$), purchased from Arkema Piezotech, were weighted and when the sonication is finished the polymer was added to the mix. Then a steering magnet was introduced to a beaker, which was sealed with parafilm. The mix has to be steered for at least 20 minutes so all of the polymer would dissolve in and all of the components would be homogeneously mixed. Also, it is important to avoid

formation of bubbles in the mix therefore the steering speed should be low ~150 rpm. In case of bubble formation, it is needed to sonicate for several seconds, so bubbles will aggregate on the surface and then to wait for several minutes for them to disappear. This recipe was repeated several times with the same materials to have enough quantity for all the devices.

For the Ag flakes composite three different solutions were prepared, each with different mass concentration of the flakes in polymer namely 55% (Solution 1), 60% (Solution 2), 65% (Solution 3). In the case of Solution 1, 295 mg of Ag flakes were added in 1.6 ml of MEK. The solution was sonicated for 15 minutes and afterwards 240 mg of P(VDF_{80}-$TrFE_{20}$) were added to the solution which was subsequently steered for 20 minutes. The fabrication process of solutions 2 and 3 is similar where the mass of polymer and the volume of solvent remains unchanged. The only difference is in the masses of the Ag flakes added to the mix. Therefore, in solution 2, 360 mg of Ag flakes were added, and in solution 3, 445 mg. The sonication and steering times are the same as for solution 1. The solutions were blade casted to form even thickness layers. The spin crossover solution was casted at the blade height of 1.300 mm on glass. To avoid the formation of bubbles in the process of drying of the solvent, the glass has to be preheated to 30-35 °C. Higher temperature will "boil" the solvent inside the layer. The usage of glass was chosen because the layer of the polymer and of the composite will stay firmly attached to the glass and therefore will keep its straight shape. The thickness of the resulting layer is around 80 μm. The thickness of the Ag flakes composites is also a part of the research therefore four different blade heights were selected for all the concentrations: 0.100 mm, 0.150 mm, 0.200 mm, and 0.3 mm.

The joint was constructed by hot pressing the layers. Given the melting point of the P(VDF_{80}-$TrFE_{20}$) of about 150 °C, the temperature for the press plates was selected to be 160 °C. For each obtained device we cut 3 layers of rectangular shapes, two of SCO composite and one of Ag composite. The width of the layers is about 5 mm and the length is about 20 mm. For each case the length of the Ag composite layer must be 1-2 mm bigger for the electrical contacts with wires. The order of the layers was SCO-AG-SCO, positioned on the bottom plate of the press as the structure was pressed from the top using the minimum possible pressure setting of ~0.2atm. The resulted device is similar to the model depicted in Figure 5.1. The cross section of one of the percolation devices is shown in the Figure 5.2. We can observe that the total thickness of the cantilever is 72 μm which is much less than the sum of the thicknesses of the three layers before pressing. The melting in the hot press favorized a strong bonding in between the layers. From the EDX image the three disctinct layers can be observed. The green color shows the position of SCO particles that contain Fe atoms. The navy colored area is filled with the Ag flakes.

The electrical contacts were fabricated by gluing the cooper wires on the longitudinal sides of the cantilevers as shown in the figure 5.3 bellow. The material used for this process was 66% mass Ag in P(VDF_{80}-$TrFE_{20}$), with lower concentration of solvent than in solutions used for blade casting, in order to not deteriorate the samples. The wire was dipped in the solution and placed on the edge of our composite sandwich where the middle electrode was exposed so it will form a firm electrical contact.

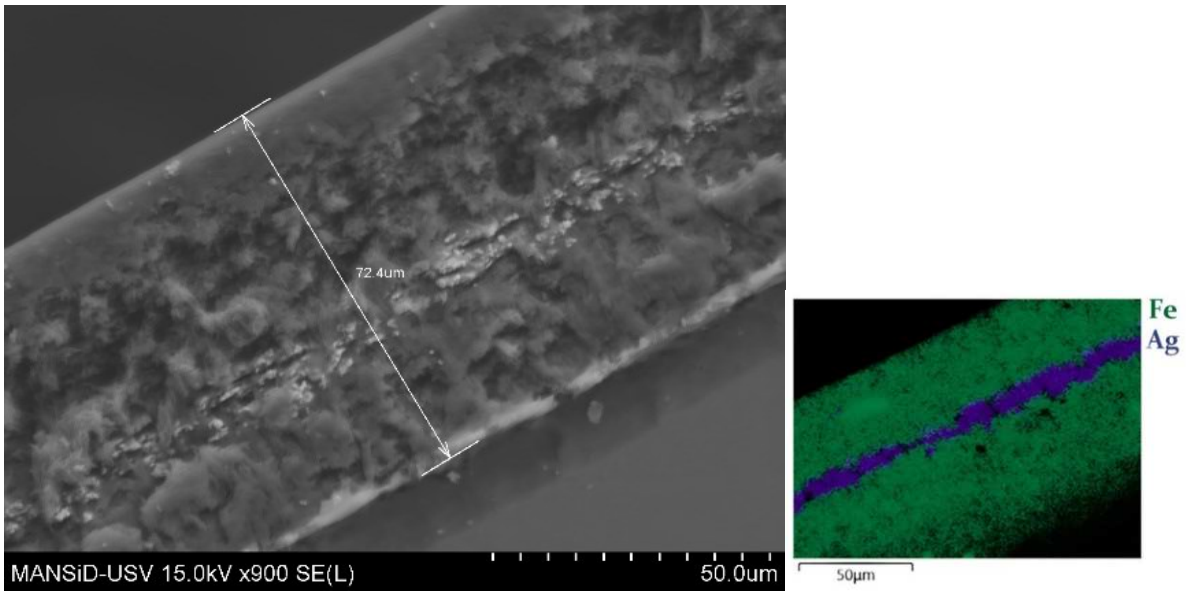

Figure 5.2. *SEM image of a percolation device containing a 60% silver composite (a), and the corresponding Energy-Dispersive X-ray (EDX) spectroscopy image of the same cantilever (b) showing the distribution of silver (Ag) in the middle layer (depicted in navy) and iron (Fe) from the Spin Crossover (SCO) composite layers (shown in green).*

5.1.3. Results and discussion of percolation device properties

The measurement setup is comprised of Keysight multimeter for the measurement of resistance and a Linkam T95 temperature controller. For increasing of the accuracy of the elctrical measurements the four wires method was used. The Linkam cell was connected via BNC cables to the multimeter and to the sample via soldered wires. The synchronous measurement was performed in heating and cooling modes, in the 30-120 °C range, with a 2 °C/ min rate, for two cycles each.

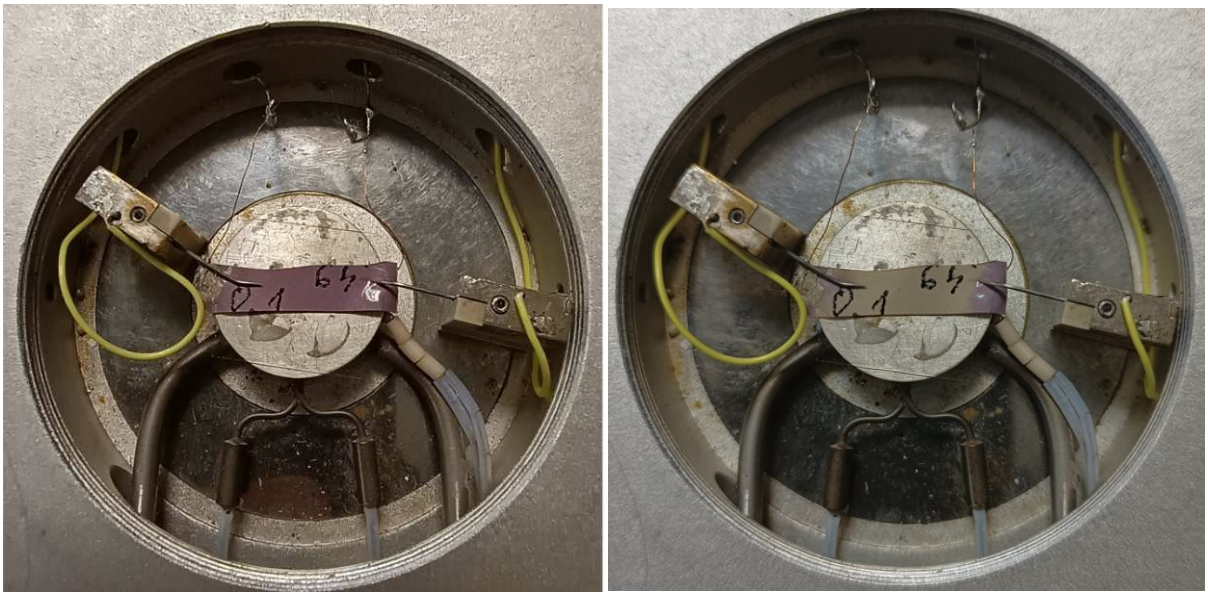

Figure 5.3. *The percolation device in the measurement setup in LS (left) and HS (right) states.*

The results of the second measurements cycle are presented in Figure 5.4. The percolation devices exhibit a similar change in resistance with the spin crossover transition for all of the concentrations of silver in the conductive composite and casting thicknesses presented above. However, the devices with 65% silver concentration and thin casting show a noteworthy difference in resistance values between the low-spin and high-spin states. This difference may be explained by the proximity to the percolation threshold, due to a wider separation of silver particles in the composite. This separation could be attributed to an uneven hot-pressing process. By subtracting the resistance increase attributed to the heating of the silver, we can isolate the "pure" spin crossover SCO-driven change in resistance (Fig. 5.5). This method allows for a better calculation of the resistance change between the low-spin (LS) and high-spin (HS) states.

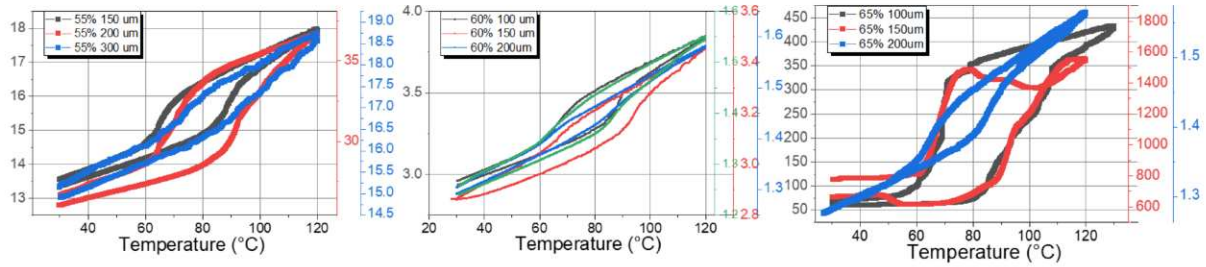

Figure 5.4. *The measured values of the resistances for the percolation devices*

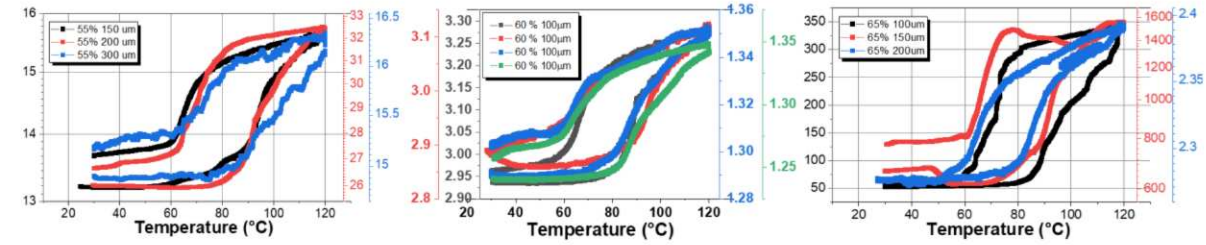

Figure 5.5. *The value of the resistances of the devices after the subtraction of thermal coefficient of resistance effect.*

We selected a temperature of 80°C, which is within the hysteresis loop, to ensure systematic measurements. Using the collected resistance values for both the HS and LS states, we then calculated the percentage change in resistance for each device. Figure 5.6 illustrates a change of around 10% in resistance for the 55% silver concentration, under 10 % for the 60% concentration and an exceptional 100% to 300% change for the two samples casted at 100 µm and 150 µm with 65% silver concentration.

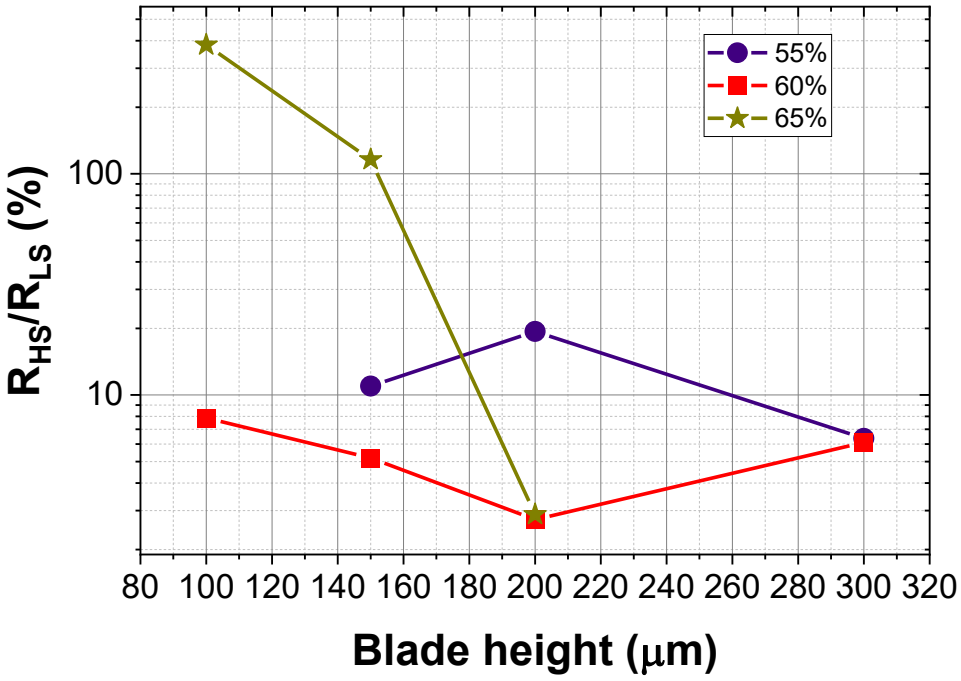

Figure 5.6. *The relative change in resistance of the percolation device between the LS and HS state, for the 80 °C temperature value state inside the hysteresis loop*

To better understand the differences in electrical resistance among the samples, we measured and compared the thickness of their silver (Ag) layers. We used Scanning Electron Microscopy (SEM) to take images of the cross-sections of the samples and determine the thickenss of the layers. Figure 5.7 shows SEM images of all three samples of different silver particles concentrations for the batch made using a blade casting process with a blade height of 150 μm.

We discovered that the sample with 65% silver concentration had clumps of silver particles amalgamated with areas with few particles. These presence of these “holes” is the likely reason for the sharp observed increase in electrical resistance because they led to poor contact between the particles.

In contrast, samples with higher initial thickens of the silver layer had particles spread out more evenly. This even distribution allowed for better contact between particles resulting in lower electrical resistance.

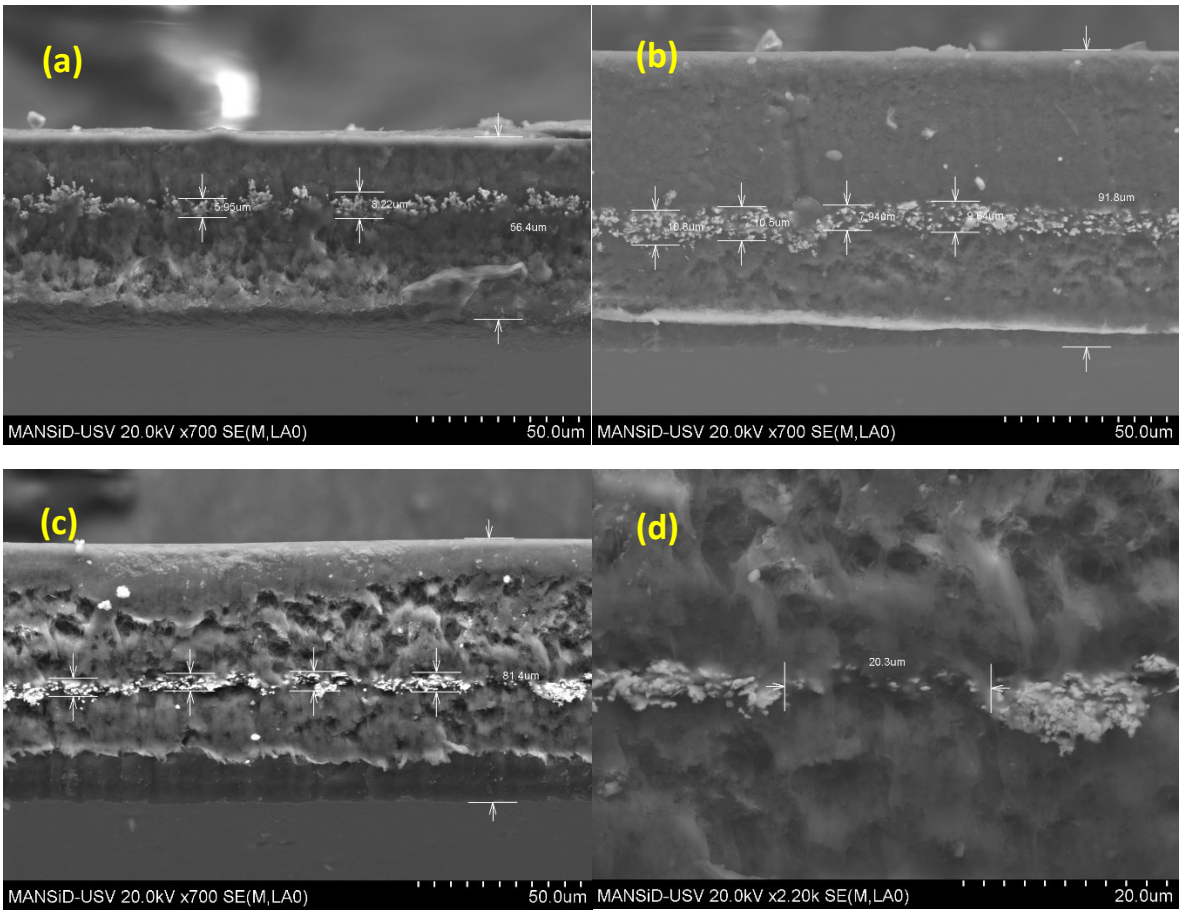

Figure 5.7 *The SEM image of the samples associated with 150um blade height fabrication of: 55% silver concentration (a), 60% silver concentration (b), 65% silver concentration (c), 65% silver concentration in a region of weak contact.*

By observing the thickness measurements from the SEM images of all the samples, we gather how changes in particle concentration and layer uniformity affect the electrical properties. By plotting the thickness of the silver layer in the samples in respect to the blade height in the blade casting process for the 3 concentrations (figure 5.8) we also remark that the thicknesses associated with 65% at blade height of 150 µm and 100 µm are less than 6 µm; that seems to be the percolation break point, because the value of the resistance is significantly higher for these samples (figure 5.6).

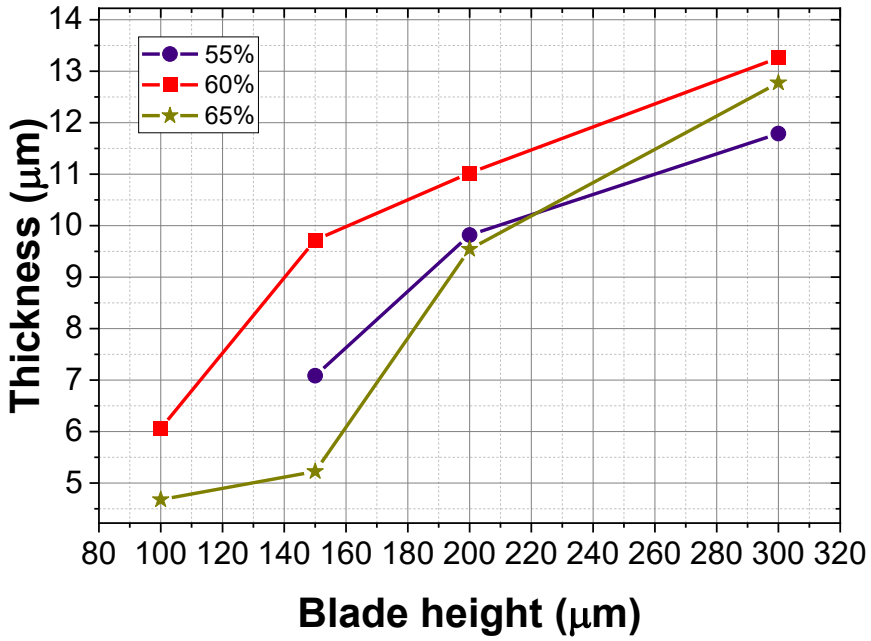

Figure 5.8 *The average thicknesses of the silver layer as a function of casting blade height of the percolation devices as extracted from SEM imaging.*

We can thus conclude that the developed percolation devices show promising properties for use in temperature sensors. Additionally, they offer a novel approach for measuring the spin crossover transitions electrically, while benefiting from the high conductivity of these devices. Moreover, if previous studies on SCO conductive composites show the resistance typically decreasing in the high-spin (HS) state, in our study we determine an increase in resistance values associated with the transition to HS state.

5.2. Spin crossover detection with the tunnel diode oscillator (TDO) technique

5.2.1. Introduction to the tunnel diode oscillator (TDO) technique

We propose here a novel method to study the RF properties of SCO materials. Typically used for magnetic susceptibility measurements, the tunnel diode oscillator (TDO) technique uses a simple electronic circuit based on the negative differential resistance of a tunnel diode to sustain oscillations in a LC tank. Since the circuit is always at resonance, minute variations in the values of capacity or inductance of the tank can yield easily measurable changes in frequency. It is a highly sensitive method that allows for the detection of small changes in the permittivity of the insulating material of the capacitor or permeability of the inductor core. The TDO method is most notably used in low temperature/ high magnetic field physics to investigate the magnetic susceptibility of insulators [13], organic compounds [14], ferromagnetic [15] or superconducting materials [16, 17] as a function of temperature or applied magnetic field; there are however very few studies that focus on the dielectric permittivity. In fact, one of the first to do a comprehensive study of the TDO method, Craig Van Degrift, built an extremely stable TDO circuit (0.001ppm) to probe the dielectric constant of liquid helium [18].

Our work involves using a SCO based capacitor as an LC tank component of a TDO circuit to investigate the dielectric permittivity of $[Fe(Htrz)_2(trz)](BF_4)$ particles by measuring induced changes in resonant frequency. We show how this simple technique can be used to study the temperature and frequency dependence of any nano/micro structured material in any temperature range and for a wide interval of RF frequencies with high resolution.

Furthermore, we construct, characterize and use flat spiral inductors embedded with SCO nanoparticles as an active part of the LC tank of the TDO to measure the magnetic susceptibility changes associated with the spin transition.

5.2.2. Construction and characterization of SCO/PVP thin film based capacitors

We constructed capacitors consists of two ITO (Indium Tin Oxide) transparent electrodes and a SCO embedded in a thin film polymer matrix as a dielectric medium. The spin-transition compound used is $Fe(Htrz)_2(trz)$ (Htrz = 1H-1,2,4-triazole) in powder form consisting of nanoparticles sized between 0.1 and 1 μm. This molecular complex exhibits a spin transition with hysteresis, having switching temperatures centered around 110°C upon heating and 60°C upon cooling. The SCO nanoparticles were mixed in EtOH and PVP solutions at various concentrations and spin coated onto the ITO glass substrates to obtain thin films (Figure 5.9 right). The concentration of SCO in the solutions allows for the modification of the signal under variable temperature, while the construction method alters the electrical capacitance value. The transparency of these capacitors allows, alongside other measurements, for optical/spectral analysis in reflectivity/transmission. This concept is novel, with a new research direction and high potential for applications.

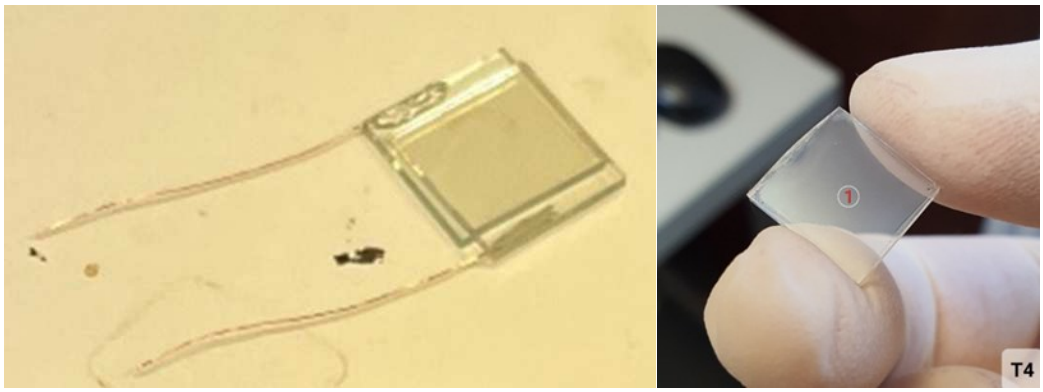

Figure 5.9 *Photograph of a double ITO-type capacitor with SCO+PVP (left) and an image of a thin high concentration SCO to PVP layer (right) obtained using spin coating*

We employed impedance spectrometry to study the AC electric response of the capacitor in variable temperature. The results illustrated below clearly show the capacity change attributed to the temperature induced change in the SCO dielectric permittivity. It is worth noting that, compared to the prevailing approach to study the dielectric properties of SCO powders using solid metal disc electrodes, our method requires a minuscule amount of SCO material for a clearly measurable signal. Concomitantly, one can probe the optical properties of the device in variable temperature. The obtained results in optical transmittance and reflectivity are displayed in Figure 5.11.

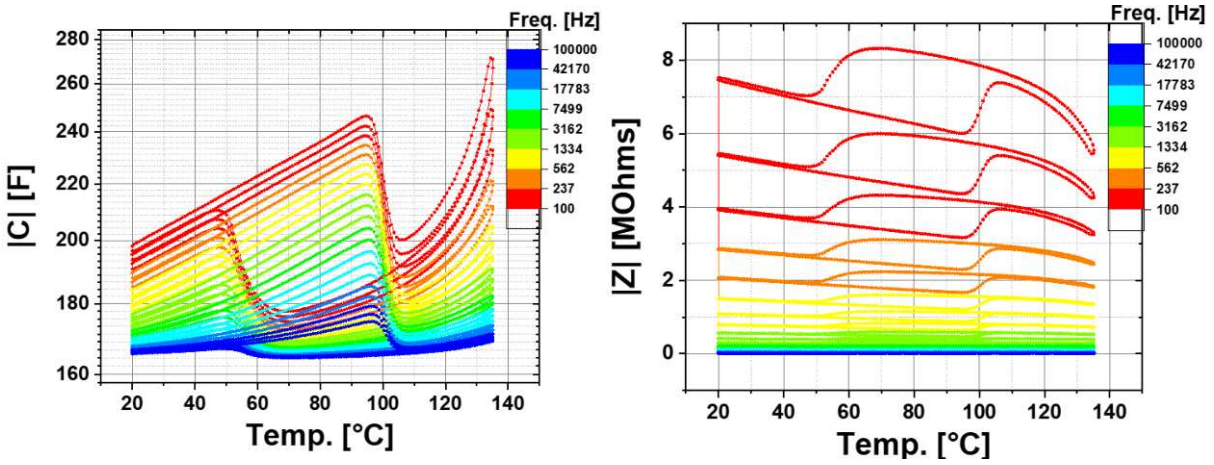

Figure 5.10 *Capacitance (left) and Impedance (right) vs. temperature for a double ITO-type capacitor with SCO+PVP, from impedance measurement at different excitation frequencies*

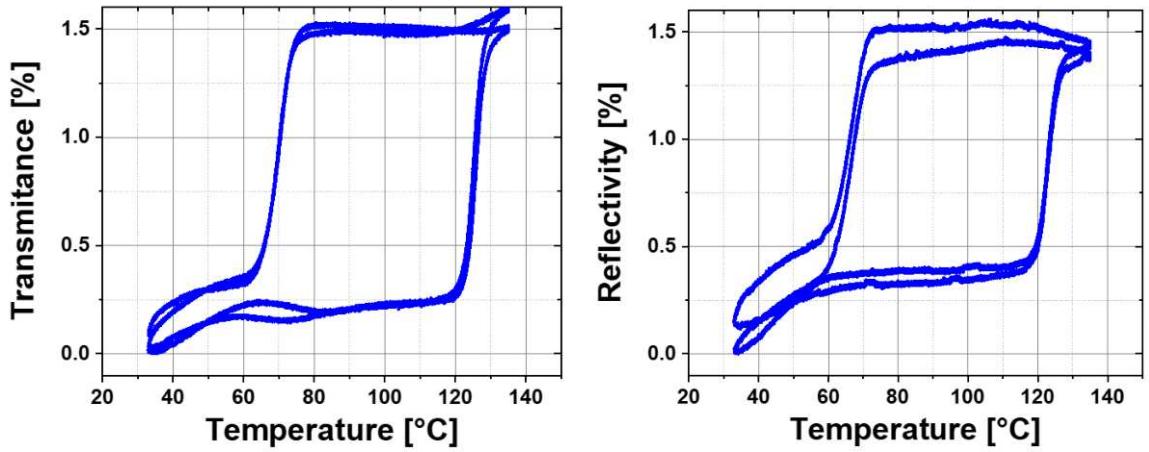

Figure 5.11 *Transmittance (left) and Reflectivity (right) vs. temperature for a double ITO-type capacitor with SCO+PVP*

We also studied the reflectivity spectrum of the SCO based capacitor versus temperature and show how one can use the spectral properties to extract information about the spin transition of the dielectric. We illustrate our results in Figure 5.12 where we show several obtained reflectivity spectra for various temperatures and relative count of a UV-VIS spectrometer for a specific wavelength to show the spin temperature induced hysteresis of the SCO/PVP dielectric.

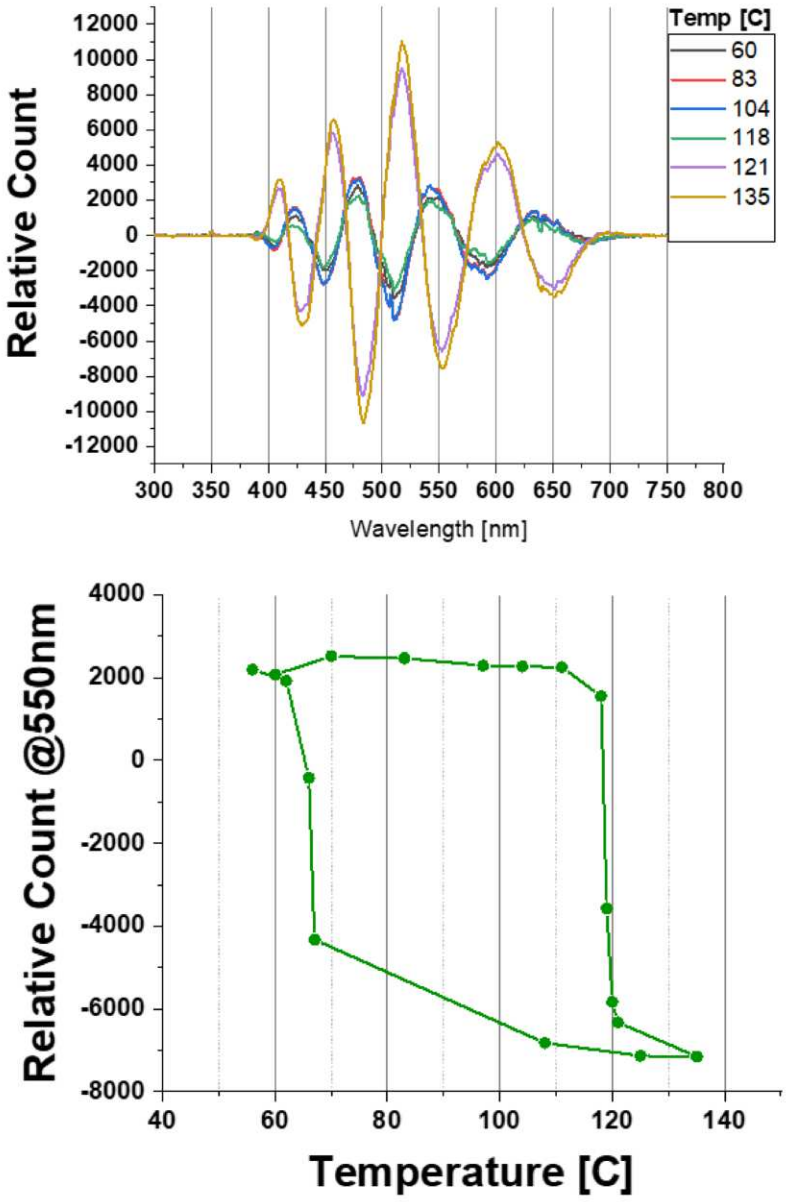

Figure 5.12 *Reflectivity spectrum and relative count value at 550 nm vs. temperature for a double ITO-type capacitor with SCO+PVP, from reflectivity and spectrometry measurements.*

5.2.3. Dielectric properties of SCO this films using a tunnel diode oscillator technique

We employ the TDO technique to study the properties of SCO thin film capacitors. $[Fe(Htrz)_2(trz)](BF_4)$ nanoparticles were embedded in a Polyvinylpyrrolidone (PVP) polymer matrix to be used as a dielectric to construct an ITO glass capacitance assembly. A diagram of the fabrication process is shown in Figure 5.13. Copper electrodes were attached to the exposed ITO sides of glass slabs using silver paste.

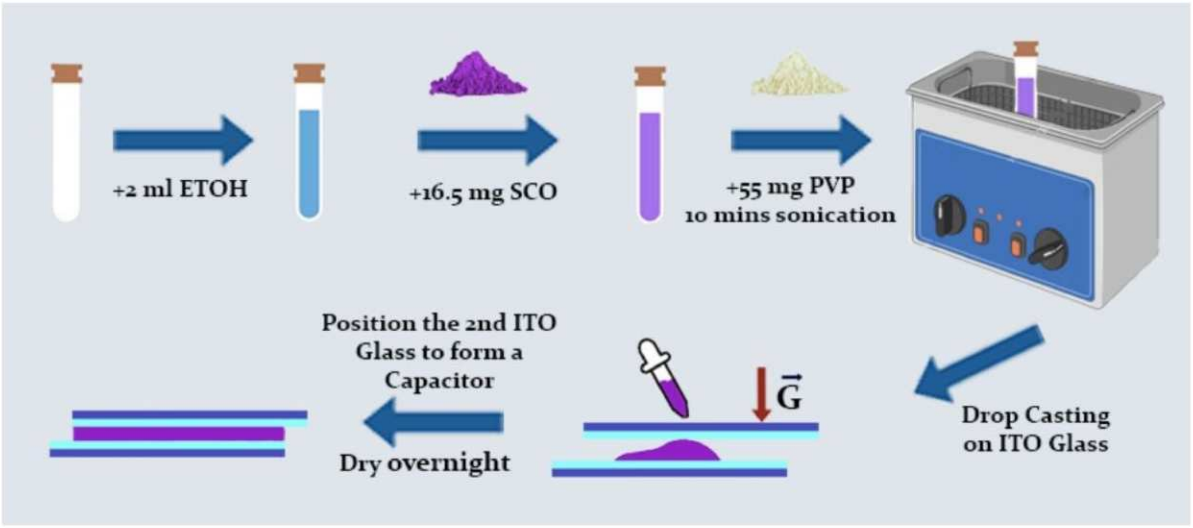

Figure 5.13 *Fabrication process of ITO glass SCO+PVP based capacitor*

The obtained capacitor is transparent (Figure. 5.14a), robust and was able to withstand multiple temperature cycles between room temperature (RT) and 155°C. The active area is ~1x0.8 cm^2 with a 25 microns thick SCO-PVP dielectric composite, with a quasi-uniform distribution of the SCO nano-particles in the PVP matrix (Figure. 5.14c). The volume ratio of SCO to PVP in the solid dielectric is 1/10. The capacitance value is around 120pF.

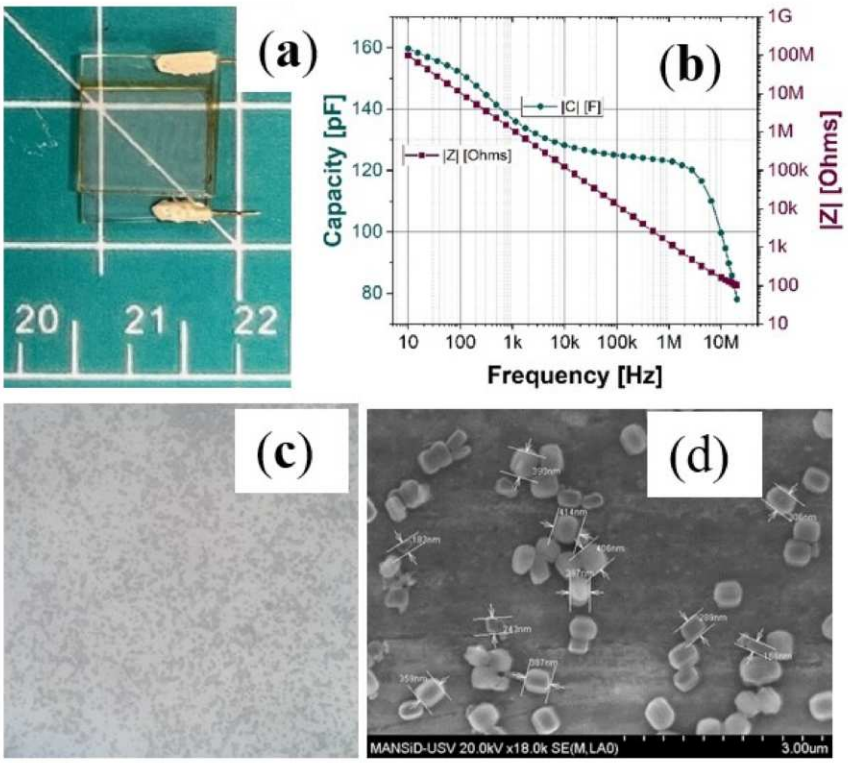

Figure 5.14. *(**a**) ITO Glass SCO+PVP intermix based dielectric capacitor; (**b**) Frequency dependent Capacity and Impedance values of the capacitor at RT as measured using broadband dielectric spectroscopy; **(c)** 50x optical image of the SCO+PVP intermix dielectric; **(d)** SEM image of $Fe[(Htrz)_2(trz)]BF_4$ particles used.*

One can easily adapt the capacity to any desired value by modifying the active contact area or dielectric thickness. We also constructed, using a similar approach, a PVP only capacitor that we tested in similar conditions to be able to extract, if any, polymer contributions to the dielectric properties results. We chose PVP as the insulating polymer for its availability, transparency and high melting temperature although we reckon any similar properties polymer could be used.

A major advantage of the TDO method is its simplicity. One only needs a few components and a frequency counter to achieve results comparable with, if not better than, expensive tools. Careful construction of the circuit can yield excellent stability and great resolution. We constructed a circuit to allow us to study the temperature variations of the capacity of our ITO Glass SCO+PVP intermix based dielectric capacitor by measuring the temperature induced resonance frequency shift of the TDO.

A schematic of the TDO circuit used is shown in Figure 5.9. It uses a MBD4057 tunnel diode along with commercially available components to drive sustained oscillations in an LC tank. The low power circuit requires a DC source (1-2V) to operate, a dc-block (or a high value capacitor), a x10 amplifier (optional) and a frequency counter. By choosing various values for L and C we can decide on the resonant frequency. In our setup, we were able to obtain oscillations ranging from 100 kHz to 50 MHz by constructing the LC tank with inductance values ranging from 0.5 μH to 150 μH and capacitor values from 10 pF to 12000 pF. Our setup has a typical frequency precision of less than 2ppm at RT meaning we can detected changes as small as 2 Hz for a 1 MHz resonant frequency considering that the stability and noise are mostly a result of outside temperature variations and electrical noise.

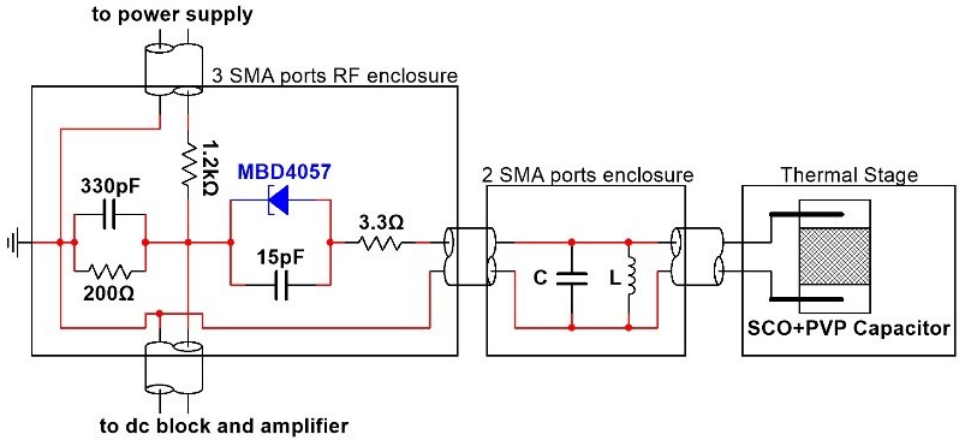

Figure 5.15. *TDO circuit design used for temperature measurements*

In order to study the temperature dependence on the SCO-PVP composite, we fitted the ITO Glass capacitor into a liquid nitrogen gas controlled temperature stage (for thermal uniformity across the capacitor assembly). The capacitor is connected in parallel, via a shielded cable, with the separate LC tank of the TDO circuit, where both the latter are kept at room temperature (RT). By choosing various values for L and C we can choose the frequency of

operation and, in turn, the frequency at which we wish to study the SCO-PVP dielectric behavior.

The operational principle of the TDO method are discussed at length in literature [19]. In order to have sustained oscillations some conditions regarding the L and C values must be met [20]. To satisfy the oscillation constraints we used Multisim to simulate and select appropriate capacitance and inductance values in order to get the desired frequency. The capacitors used are all NP0 commercial type capacitors however, the coils we built in house. We used COMSOL Multiphysics to simulate the number of magnet wire turns needed to obtain desired inductivity and DC resistance values of coils, which we then built using GE varnish to encapsulate the solenoid windings. Considering the capacitance value of ~ 120pF of our SCO-PVP based capacitor, we combined various values for the parallel C (namely 0, 470, 1000, 1500 and 10000pF) with inductors constructed with different L values (namely 3, 6, 21 and 100μH) to obtain different resonant frequencies. We were thus able to probe the SCO-PVP dielectric at 7.52MHz, 4.86 MHz, 2.32 MHz, 1.38 MHz, 873 kHz, 466 kHz and 152 kHz by measuring the frequency variation with temperature.

Since the resonant frequency of the circuit is dependent on most circuit components values, absolute values of L or C are difficult to extract from direct frequency measurements meaning the method is typically used for relative measurements. We are interested in the capacitance, C_T, variation as a function of temperature of our SCO-PVP based capacitor, which is in a parallel configuration with the fixed capacitance value capacitor in the LC tank kept at RT. The fixed value C is altered by the parasitic capacitance from connecting cables, which is a function of frequency and insignificantly affected by sweeping temperature variations; we can thus consider it as fixed. Nonetheless, we can get absolute capacitance values from the precise estimations of small variations of C_T, as in our case, if we know an approximate initial value. There are more accurate formulas for the resonant frequency of a TDO circuit [20, 21], which take into account most variables however, for our measurements the classical formula is more than adequate. Considering the resonant frequency:

$$f \cong \frac{1}{2\pi\sqrt{L(C+C_T)}} \tag{5.1}$$

it is easy to show that, for small variations of C_T

$$\delta C_T = -\frac{\delta f}{2\pi^2 f^3 L} \tag{5.2}$$

Knowing our L values, we can accurately estimate C_T as a function of temperature as $C_{RT}+\delta C_T$ from frequency measurements, where we consider C_{RT} as the capacity value of the SCO-PVP based capacitor at RT, as measured by any other capable instrument. The measurement does not have to be very precise or the value taken at RT. We did however considered the RT value of the capacity as extracted from the data represented in Figure 5.12(b). All temperature measurements herein were carried out in a similar way and entail three complete heating/cooling thermal cycles between 20°C and 130°C, at 2°C /min, with 5 min waiting time at each temperature extrema.

5.2.4. Results and discussion of TDO measured capacitive devices

The obtained SCO+PVP composite keeps its spin crossover properties being stable over several successive temperature cycles. Figure 5.16a shows the temperature dependence of the high spin fraction, $n_{HS,}$ recorded by using a MPMS3 Quantum Design magnetometer, on SCO+PVP intermix film obtained from drop casting the same solution used for fabricating our capacitor, albeit a thicker film for sufficient magnetic signal.

We show firstly one of the data sets obtained from the TDO resonant frequency measurements as a function of temperature for our ITO Glass SCO-PVP intermix based dielectric capacitor along with the data for the PVP based capacitor (Figure 5.16b). The curves shown correspond to the second (2/3) thermal cycles. The first thermal cycle (usually after a period of rest) exhibits strong, subsequently non-repeatable variations of the capacity of both PVP+SCO and PVP only capacitors and are most likely due to solvent evaporation in SCO or thermal relaxation effects in the PVP polymer.

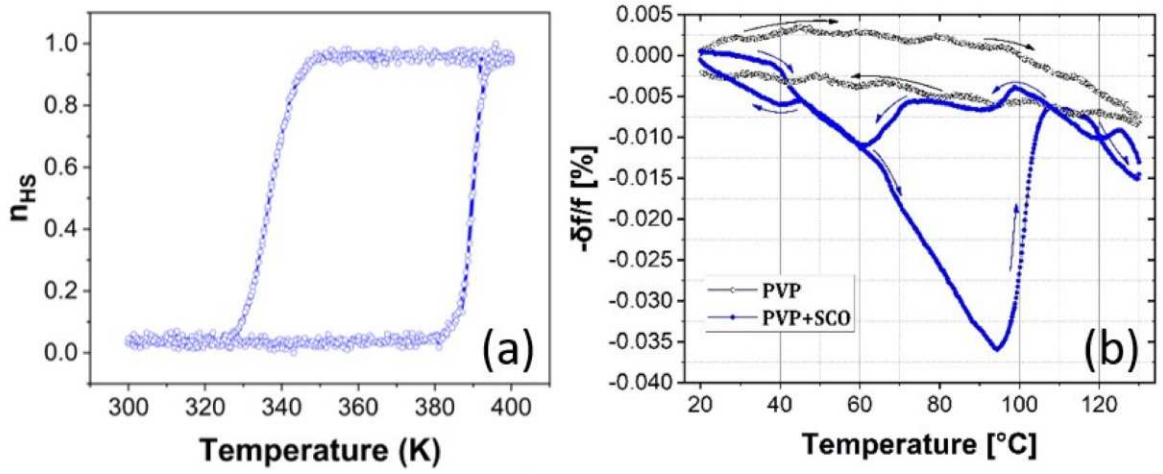

Figure 5.16. (a) *High-spin fraction (n_{HS}) as a function of temperature for the SCO-PVP composite, measured using an MPMS3 SQUID magnetometer; and (b) TDO frequency relative shift as a function of temperature for both the PVP only and SCO+PVP dielectric capacitor at ~ 0.9 MHz.*

In this particular case, we used a 21μH inductor and 1500pF capacitor for the LC tank with both ITO Glass capacitors. The resonant frequency at RT, i.e. at the start of the second cycle, for the ~ 120pF SCP+PVP capacitor is f_{RT} = 872800 ± 1Hz while for the ~ 80pF PVP only capacitor is 890300 ± 1Hz. The δf values are calculated as the difference in measured frequency f and f_{RT}. The solid polymer matrix widens the thermal hysteresis of the SCO. Transition temperatures, as extracted from the derivatives extrema of the T dependence, in heating/cooling modes, are 113/74°C for the unattended powder and 117/63°C respectively for the SCO+PVP intermix.

We show in Figure 5.17 the obtained results for the temperature dependent capacity variations, as estimated using Equation 2, of our SCO+PVP dielectric based capacitor for seven different resonant frequency of our TDO circuit

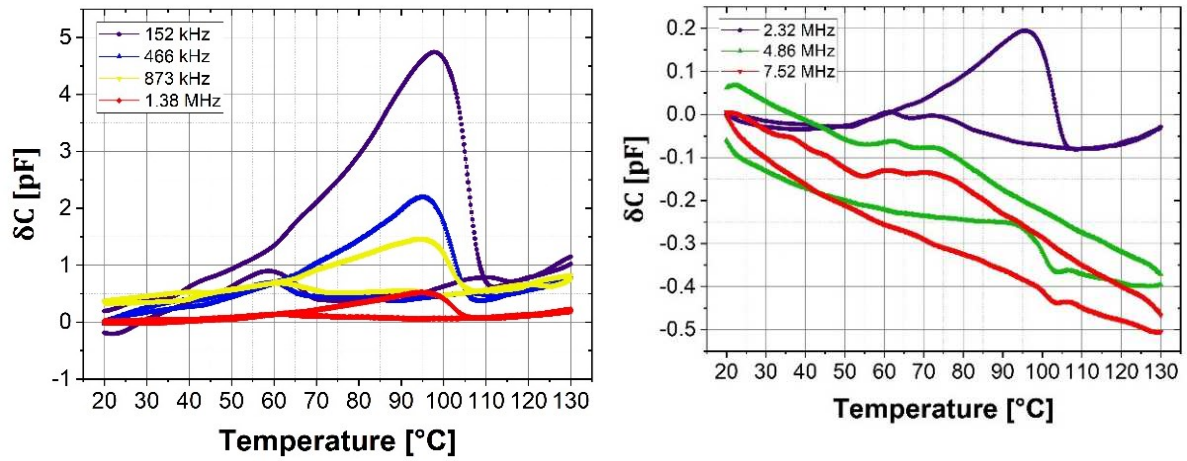

Figure 5.17. *Capacity variation with temperature δC_T of $[Fe(Htrz)_2(Trz)](BF_4)$ particles in PVP dielectric ITO glass capacitor (in pF) as extracted from TDO frequency measurements, for lower frequencies (left) and higher frequencies (right)*

The absolute capacity values $C_{RT}+\delta C_T$ can be easily calculated by adding the RT value for a given frequency. For example, at 873kHz, the room temperature value C_{RT} is 123pF (see Figure 5.14b) meaning that the highest LS TDO estimated value is 123 + 1.5pF. The relative dielectric permittivity can be estimated knowing the area and separation distance between the electrodes. The temperature variation of ε_r as inferred from capacitance results, for various TDO frequencies, is shown in Figure 5.18.

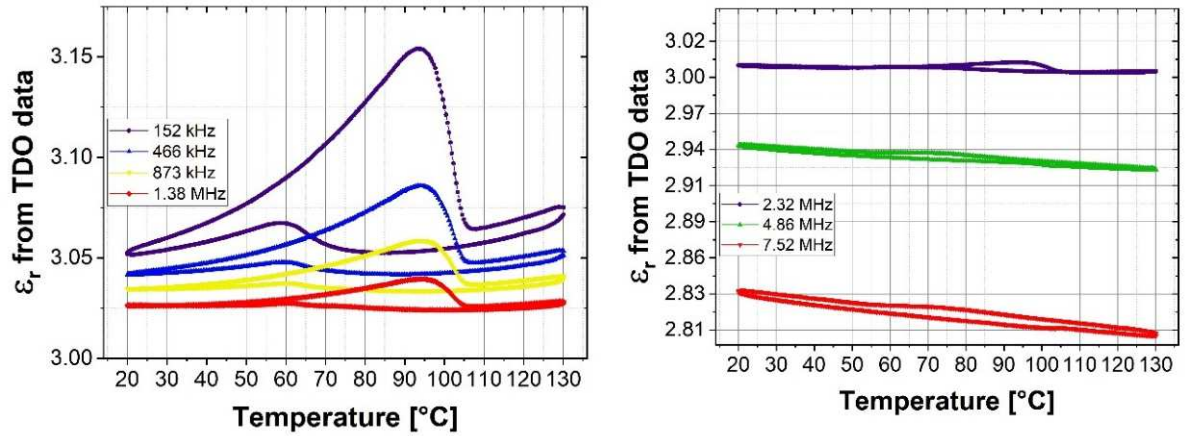

Figure 5.18. *Dielectric permittivity of $[Fe(Htrz)_2(Trz)](BF_4)$ particles in PVP matrix, for lower measured TDO frequencies (left) and higher measured TDO frequencies (right)*

The results are strongly matching the broadband spectrometry dielectric measurements reported in literature for this SCO compound [2]. If we now plot the frequency dependence of δC_T, which is the capacity value as measured by the TDO minus the capacity value at RT, for several temperatures (Figure 5.19), we get the typical relaxation process of electric dipoles in

SCO where we have a reduction in dielectric permittivity with increasing frequency [22]. We chose to show δC_T rather than absolute C_T values due to scaling issues in distinguishing any dependence with temperature. All curves seem to indicate the presence of an inflection point around 600kHz with a maximum at ~900kHz.

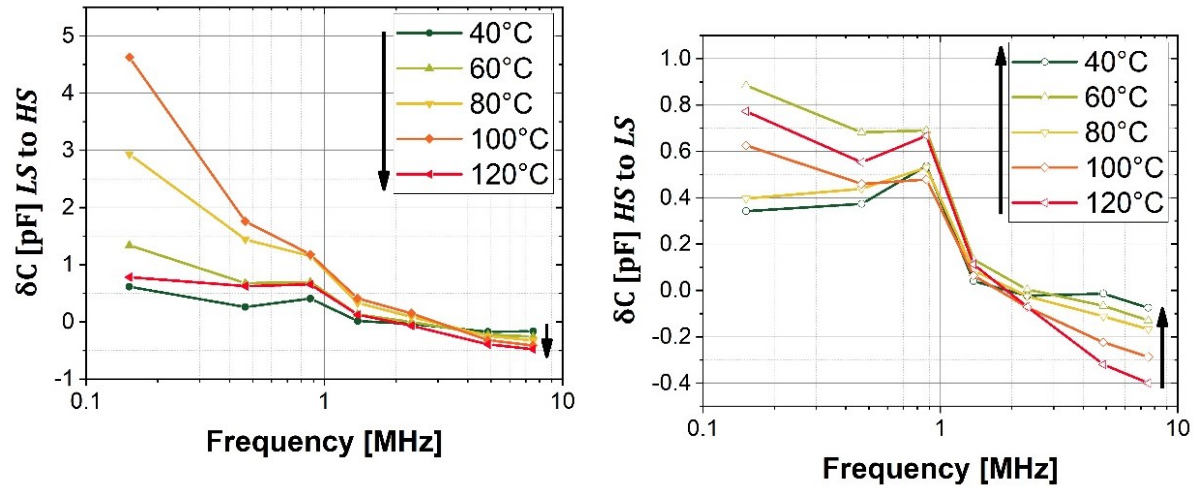

Figure 5.19. *Capacity shift from RT value as a function of TDO resonant frequency for 6 temperature values in:* ***(left)****. heating mode;* ***(right)*** *cooling mode.*

5.3. Magnetic measurements of spin crossover composites.

The LC resonant circuit at the base of the TDO measurement technique allows us to measure not only the capacitance, and thereby the electrical properties of the material inside the capacitor, but also the magnetic properties of the SCO material by integrating it into the coil of the resonant circuit. The starting point of the idea of using the TDO to measure the magnetic susceptibility changes of SCO materials came from the results described below, where we measure inductance of a planar coil covered with SCO nanocrystals.

The SCO compound was dispersed by ultrasonic sonication in EtOH and deposited either as a colloidal solution or mixed with the polymer PVP (PVP = polyvinylpyrrolidone). The methods used for depositing SCO solutions on the fabricated inductors include drop-casting, dielectrophoresis, and spin-coating. The morphological properties of the obtained structures were investigated using optical microscopy and electron microscopy (FE-SEM). The spin transition properties were monitored through electrical (inductive) measurements in dynamic, AC mode, and optical (reflectivity) measurements under variable temperature conditions.

A series of flat spiral coils were fabricated by either a CNC machine on a printed circuit board (PCB) or using a PCB printer. We firstly used impedance spectrometry to probe the inductance of the coils embedded with SCO particles, in variable frequency, temperature and even pressure.

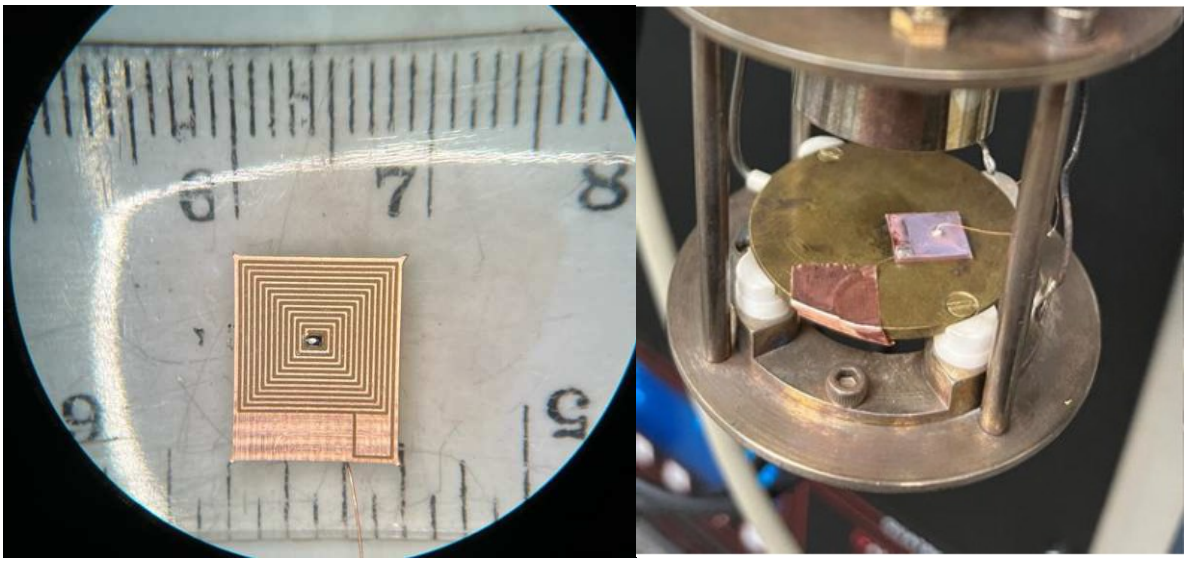

Figure 5.20. *The images of coils used for magnetic measurements with Impedance spectroscopy.*

The EtOH + spin-crossover particles solution was added on top of the coil to cover all the surface of it. When the solvent evaporates the particles cover all of the coil area.

The SCO dopped coil was inserted in the temperature chamber of the impedance spectroscopy apparatus where the measurement was performed in thermal cycles (heating and cooling) from 20°C to 130 °C.

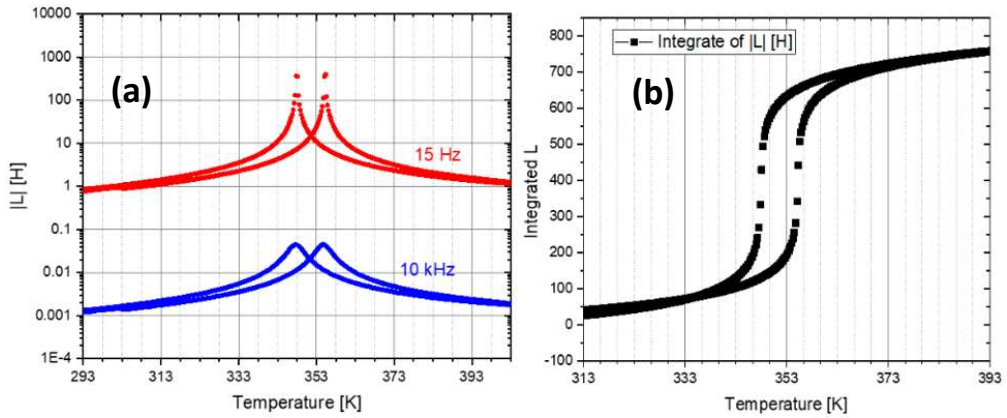

Figure 5.21*. The values of the measured inductance of the coil with SCO in temperature (a). The integral of the inductance that reveals the spin transition hysteresis(b).*

The result of the measurements expose, for the first time, the two heating and cooling transition peaks in the values of inductance. The one that occurs at the heating ramp is associated to the transition from low spin to high spin while the other one, in cooling ramp, associated with the transition from high to low spin (Figure 5.21).

We also tested the effect of pressure on spin transition via magnetic measurements as it has been previously measured and observed in the electrical properties of the spin crossover materials.

As in the previous experiment, the measurement is done on a fabricated coil but in pressure cell with silicone oil, as the agent of heat transfer and the medium for hydrostatic pressure. To prevent the scattering of the particles in oil, we coated the coil this time with SCO composite mixed with commercial type epoxy. The image of the filled coil is presented in figure 5.22

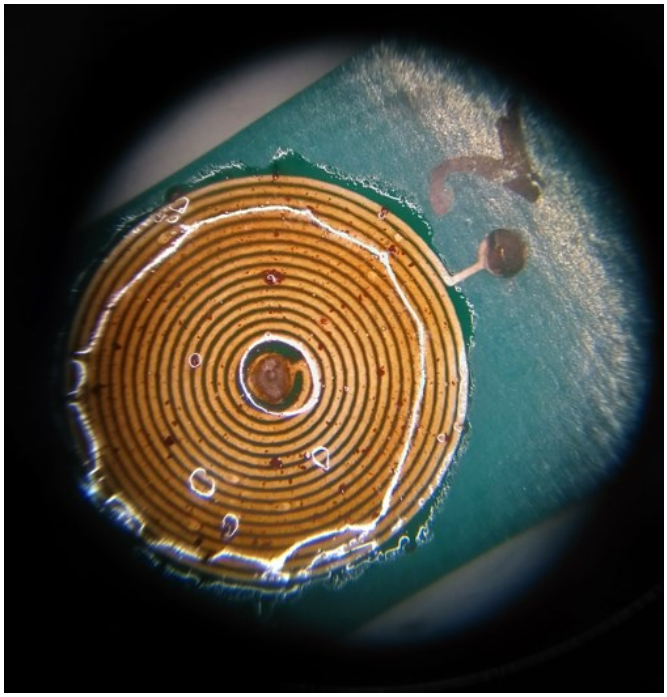

Figure 5.22. *The image of the coil used in magnetic measurements under pressure covered in epoxy with spin crossover particles*

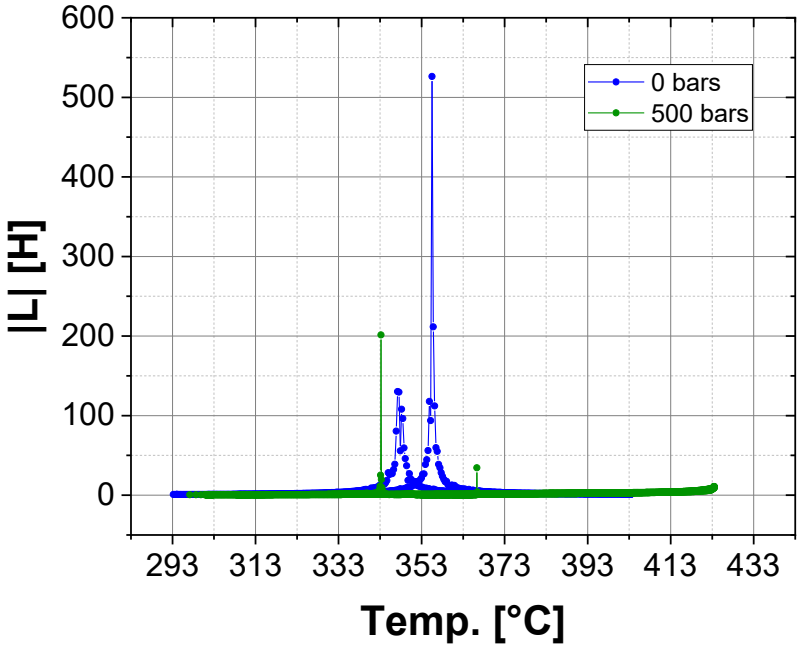

Figure 5.23*. The temperature values of inductance measured for a flat spiral coil with spin crossover particles under pressure.*

The variable temperature measurements were performed under 2 different pressure values: 0 bars and 500 bars. From the measurement results (Figure 5.19) we observe the same behavior for inductance as at ambient pressure with two transition peaks associated to the spin crossover transition. The effect of pressure in increasing the transition temperature in heating and decreasing the transition temperature values in cooling, thereby increasing the hysteresis width with the pressure increase, can clearly be seen in the inductance values versus temperature. It is worth mentioning that the amount of change in inductance value during the LS-HS/HS-LS transition is several order of magnitude greater than other reported results. This measured inductance value change is more pronounced at lower excitation frequencies (tens and thousands of Hz) and less so at higher frequencies (MHz) of the AC probing voltage. In principle, this especially large signal induced by the SCO transition, combined with the sensitivity of the TDO resonant method, should allow for the detection of a minuscule amount of nano-sized SCO particles. We show below an example of such a measurement in which we used the TDO to study the frequency shift induced be the SCO transition.

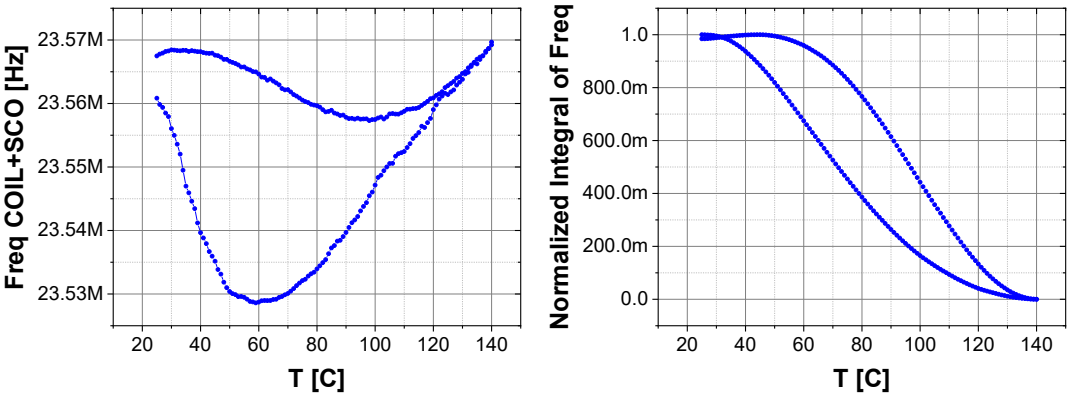

***Figure 5.24**. The temperature values of TDO frequency measured for a coil containing spin crossover particles (left) and the integral (right) showing the SCO hysteresis*

5.4. Conclusions

We show for the first time how a percolation-based strain sensor can be used to study the spin state of SCO materials. We also show, for the first time, how a tunnel diode oscillator can be used to study the spin state from dielectric permittivity measurements of sub-micron particles in variable temperature and frequency. The results obtained for $[Fe(Htrz)_2(Trz)](BF_4)$ particles imbedded in a PVP matrix, used as dielectric filling for a parallel plate ITO Glass capacitor, show the proof of concept and validity of the TDO method in characterizing the dielectric permittivity of SCO materials. The capacitor can be easily build to accommodate a wide range of materials of various particle shape and sizes or structures. Due to the micron size separation of the electrodes, the active dielectric material quantity required is very low. It can be constructed in any shape, area and thickness and can be made to resonate with a wide range of inductance and parallel capacity values to allow for a large range of RF excitation frequencies. The construction of the circuit is simple and accessible with results comparable with complex and expensive instrumentation. One can, in principle, build a TDO circuit to suit a wide

range of applications most notably any that require temperature changes, pressure variations, optical excitation or applied magnetic field.

References

[1] Rahaman, M., Aldalbahi, A., Govindasami, P., Khanam, N. P., Bhandari, S., Feng, P., & Altalhi, T. (2017). A new insight in determining the percolation threshold of electrical conductivity for extrinsically conducting polymer composites through different sigmoidal models. Polymers, 9(10), 527.

[2] Kim, K. K., Hong, S., Cho, H. M., Lee, J., Suh, Y. D., Ham, J., & Ko, S. H. (2015). Highly sensitive and stretchable multidimensional strain sensor with prestrained anisotropic metal nanowire percolation networks. Nano letters, 15(8), 5240-5247.

[3] Jaafar, A. H., O'Neill, M., Kelly, S. M., Verrelli, E., & Kemp, N. T. (2019). Percolation threshold enables optical resistive-memory switching and light-tuneable synaptic learning in segregated nanocomposites. Advanced Electronic Materials, 5(7), 1900197.

[4] Nieto-Castro, D., Garcés-Pineda, F. A., Moneo-Corcuera, A., Sánchez-Molina, I., & Galán-Mascarós, J. R. (2021). Mechanochemical processing of highly conducting organic/inorganic composites exhibiting spin crossover–induced memory effect in their transport properties. Advanced Functional Materials, 31(33), 2102469.

[5] Piedrahita-Bello, M., Zan, Y., Enriquez-Cabrera, A., Molnár, G., Tondu, B., Salmon, L., & Bousseksou, A. (2022). Effect of the spin crossover filler concentration on the performance of composite bilayer actuators. Chemical Physics Letters, 793, 139438.

[6] Habbal, F.; Watson, G. E.; Elliston, P. R., Simple cryostat for measuring rf susceptibility from 4.2 to 300 K. Review of Scientific Instruments 2008, 46, (2), 192-195.

[7] Riet, B. V.; Gerven, L. V., A cryogenic RE oscillator, the heart of a new NMR dispersion spectrometer. Journal of Physics E: Scientific Instruments 1982, 15, (5), 558.

[8] Spinu, L.; Srikanth, H.; Gupta, A.; Li, X. W.; Xiao, G., Probing magnetic anisotropy effects in epitaxial ${\mathrm{CrO}}_{2}$ thin films. Physical Review B 2000, 62, (13), 8931-8934.

[9] Diaconu, A.; Martin, C.; Hu, J.; Liu, T.; Qian, B.; Mao, Z.; Spinu, L., Possible nodal superconducting gap in Fe${}_{1+y}$(Te${}_{1\ensuremath{-}x}$Se${}_{x}$) single crystals from ultralow temperature penetration depth measurements. Physical Review B 2013, 88, (10), 104502.

[10] Kim, H.; Tanatar, M. A.; Prozorov, R., Tunnel diode resonator for precision magnetic susceptibility measurements in a mK temperature range and large DC magnetic fields. Review of Scientific Instruments 2018, 89, (9), 094704.

[11] Van Degrift, C. T., Tunnel diode oscillator for 0.001 ppm measurements at low temperatures. Review of Scientific Instruments 1975, 46, (5), 599-607.

[12] Diaconu, A.; Spinu, L. In Design of a tunnel diode oscillator for material properties investigations, 2014 International Conference on Optimization of Electrical and Electronic Equipment (OPTIM), 22-24 May 2014, 2014; 2014; pp 858-865.

[13] Gevorgyan, S. G.; Movsesyan, G. D.; Movsisyan, A. A.; Tatoyan, V. T.; Shirinyan, H. G., Modeling of tunnel diode oscillators and their use for some low temperature investigations. Review of Scientific Instruments 1998, 69, (6), 2550-2560.

[14] Van Degrift, C. T.; Love, D. P., Modeling of tunnel diode oscillators. Review of Scientific Instruments 1981, 52, (5), 712-723.

[15] Soroceanu, I.; Graur, A.; Coca, E.; Salmon, L.; Molnar, G.; Demont, P.; Bousseksou, A.; Rotaru, A., Broad-Band Dielectric Spectroscopy Reveals Peak Values of Conductivity and Permittivity Switching upon Spin Crossover. The Journal of Physical Chemistry Letters 2019, 10, (23), 7391-7396.

GENERAL CONCLUSIONS AND PERSPECTIVES

The unique switchable physical properties of molecular spin crossover compounds provide an attractive research field for the development of a wide range of applications requiring stimuli-responsive, 'active' materials, including sensors, actuators and heat management devices. However, interfacing SCO materials with electronic devices remains currently a considerable bottleneck due to the rather weak changes of electrical properties (conductivity, permittivity) that most SCO compounds display at the spin transition. To make SCO compounds "electroactive" the SCO community proposed several approaches, which are usually based on a smart combination of SCO materials with various electroactive materials within composites or within more complex systems. The present thesis is devoted thus to the exploration of novel ideas, which could contribute to the development of innovative electronic devices based on SCO molecules.

To this aim we have fabricated various SCO@polymer composite materials by embedding SCO nanoparticles of the iron(II)-triazole family within a ferroelectric polymer matrix, poly(vinylidene fluoride-co-trifluoroethylene), P(VDF-TrFE). In certain cases, a polyvinylpyrrolidone (PVP) matrix was also used for prototyping. We explored two different composite fabrication methods. In a first approach, we used a blade casting technique to form composite films, which was subsequently hot pressed to achieve good crystallinity and high density of the polymer matrix. As a promising alternative route, we also explored the use of electrospinning to form SCO@polymer composite nanofibers. Whatever the fabrication method, we observed a small, but clearly detectable impact of the polymer matrix on the spin transition behavior, manifested by an increase of the hysteresis width and a less abrupt transition, whereas the barycenter of the hysteresis did not change considerably. This means that the matrix (and/or the processing method) does not impact the spin state equilibrium, but it alters the cooperativity and givers rise also to a broader distribution of transition temperatures.

We have also conducted a detailed analysis of the electrical properties of the composite materials by means of variable temperature, broadband dielectric spectroscopy, focusing mostly on the electrospun composites. We employed the Havriliak-Negami approach to separately investigate the different contributions to the global dielectric response. Through this analysis we made correlations between the reduced conductivity in the composite nanofibers (vs. the neat SCO powder) and the dielectric relaxation parameters. We have also established the links between the spin state of the composite and its dielectric properties. In particular, we have evidenced a strongly reduced dielectric relaxation strength in the high spin state, suggesting possible applications in charge storage and manipulation through the SCO phenomenon.

Although we could not yet characterize the piezoelectric properties of the electrospun SCO@P(VDF-TrFE) composite nanofibers, it remains thus an important perspective for future work. On the other hand, using electrical poling, we could demonstrate remarkable piezoelectric properties for the hot pressed SCO@P(VDF-TrFE) composite films. Subsequently, we have conducted very careful experiments to examine the controversial question of the effect of ferroelectric polarization on the spin crossover properties, both in 33 and 31 connectivity

SCO@P(VDF_{80}-$TrFE_{20}$) composites, however no sizeable effect could be observed, despite a relatively high degree of polarization. The results show that recent reports in the literature about this type of effects certainly cannot be generalized and further work is necessary to address the effect of strong local electric fields on the spin-state equilibrium.

In the next step, we have fabricated a multilayer cantilever device combining a pyroelectric P(VDF-TrFE) polymer layer with our SCO@P(VDF-TrFE) films, complemented by electrically conducting Ag@P(VDF-TrFE) composite layers. We designed this 31 type composite device with the aim to overcome the pitfalls of previously studied 33 connectivity SCO@ P(VDF-TrFE) particulate composites, aimed for thermal energy harvesting purposes. Indeed, the separation of the two materials allowed us to optimize independently the SCO strain, which reached a remarkable value of 3 %, and the piezoelectric charge coefficient, which was as high as -20 pC/N in our experiments. We have hot pressed both symmetrical devices (showing no bending motion) and asymmetrical ones, displaying large, reproducible deflections upon thermal cycling. Each device displayed significant piezo-currents upon finger tapping and pyro-currents in response to temperature changes. Most importantly, each device displayed clear anomalies of the pyro-current at the spin-transition temperature, providing evidence for an extra piezoelectric charge generation due to the SCO actuation. Remarkably, the sign of these piezo-current anomalies was found to be the same (resp. opposite) as the sign of the ordinary pyro-current in the asymmetric (resp. symmetric) device, which we could attribute to the different sign of the mechanical stress generated in the two devices (compressive vs. tensile). Based on this first proof of concept, further work should focus on the optimization of the device configuration, using continuum mechanics simulations, in order to bring the entire piezoelectric layer into compression and thus maximize the harvester output. Obviously, it will be also important to better quantify the figures of merits of the harvester devices, to evaluate their relevance in comparison with already existing technologies.

During the work on the harvesters, we have serendipitously discovered that the Ag@P(VDF-TrFE) composite films can be also used for electrical sensing the SCO phenomenon in attached SCO@polymer layers. In this case the conducting silver composite works as a strain sensor, exploiting percolation effects, when the concentration of Ag particles is optimized. We have shown that these percolation devices are promising candidates for temperature sensors. On the other way around, they offer a novel means for the detection of the spin crossover phenomenon electrically. In a parallel approach, we have also worked on a tunnel diode oscillator (TDO) based sensing method, which can be used to study the frequency dependent dielectric permittivity, and thus the spin state, of sub-micron sized particles as a function of the temperature. The results obtained for $[Fe(Htrz)_2(Trz)](BF_4)$ particles imbedded in a PVP matrix, used as dielectric filling for a parallel plate capacitor, allowed us to validate the TDO method in characterizing the dielectric permittivity of SCO materials. The capacitor can be easily built to accommodate a wide range of materials of various particle shapes and sizes or structures. Due to the micron size separation of the electrodes, the active dielectric material quantity required is very low, which is an interesting asset for device integration. The implementation of these different methods for electrical sensing of the SCO phenomenon is

simple, does not require expensive instrumentation, compatible with various external stimuli (temperature changes, pressure variations, optical excitation or applied magnetic field) and easily amenable to be integrated into more complex systems.

Overall, this thesis work demonstrates how by developing synergies between the bistable properties of SCO compounds and the electrical characteristics of associated materials in hybrid systems affords for innovative solutions for sensing spin state changes, mechanically actuating electrical devices and harvesting different forms of energy. As such, it opens promising perspectives for future collaborative work between material scientists and electronic engineers.

RÉPUBLIQUE FRANÇAISE
Liberté
Égalité
Fraternité

Université de Toulouse

Titre : Contributions au développement des dispositifs électroniques basés sur des molécules à transition de spin

Mots clés : Dispositifs électroniques, Transition de spin, Propriétés électriques

Résumé : Dans cette thèse, nous étudions la conception, la fabrication et la caractérisation de matériaux et de systèmes hybrides combinant des complexes à transition de spin (TS) avec des polymères électro-actifs. L'objectif est de créer des synergies entre les propriétés bistables des composés à TS et les caractéristiques électriques des matériaux associés, ouvrant la voie à des applications innovantes: capteurs, actionneurs et générateurs d'énergie. La thèse aborde la fabrication et l'analyse de matériaux composites intégrant des nanoparticules à TS de la famille des complexes fer(II)-triazole dans une matrice polymère ferroélectrique, le poly[(vinylidènefluorure-co-trifluoroéthylène], P(VDF-TrFE). Dans certains cas, une matrice polyvinylpyrrolidone (PVP) a été également utilisée pour prototypage. Les composites sont élaborés à l'aide des techniques de 'blade-casting', combiné avec un pressage à chaud, et de l'électrofilage, suivi par leur caractérisation à l'aide des techniques de magnétométrie, microscopie électronique à balayage, calorimétrie et spectroscopie diélectrique. Dans un premier temps, nous étudions l'effet de la polarisation électrique de la matrice sur les propriétés de transition de spin des nanoparticules incorporées. L'impact des substrats ferroélectriques, P(VDF80-TrFE20), sur des films à TS nanométriques est également exploré. Malgré une polarisation effective, manifestée par des coefficients piézoélectriques d33 élevés (-20 pC/N), nous montrons que l'équilibre de spin ne subit pas de modification notable. En revanche, nous mettons en évidence des effets subtils de la matrice polymère sur les propriétés à TS. Un aspect innovant de la thèse est le développement de dispositifs multicouches pour la récupération d'énergie thermique. Composés d'un film pyro/piézoélectrique P(VDF-TrFE), associé à des couches composites TS@P(VDF-TrFE) et Ag@P(VDF-TrFE), ces dispositifs génèrent deux types de courants en réponse de la variation de la température: l'un dû à l'effet pyroélectrique ordinaire, l'autre dû à l'effet piézoélectrique, induit par la déformation thermique du composite à TS. En ajustant le signe de l'effet piézoélectrique, ces contributions peuvent être additionnées pour améliorer l'efficacité du dispositif. Enfin, la thèse présente deux approches novatrices pour la détection électrique du changement d'état de spin dans les matériaux composites TS@polymère. La première utilise un capteur de déformation, Ag@P(VDF-TrFE), attaché à la couche active et fonctionnant sur les effets de percolation. La seconde introduit une méthode pour étudier la permittivité diélectrique des matériaux à TS via une diode à effet tunnel résonnant, utilisée en oscillateur radiofréquence.

Title: Contributions to the development of electronic devices based on spin crossover molecules

Key words: Electronic Devices, Spin Crossover, Electrical properties

Abstract: In this thesis, we investigate the design, fabrication, and characterization of hybrid materials and systems, which combine spin crossover (SCO) complexes with electroactive polymers. The aim is to develop synergies between the bistable properties of SCO compounds and the electrical characteristics of the associated materials, leading to innovative applications in sensors, actuators and energy harvesting technologies. The work starts with the fabrication of composite materials incorporating SCO nanoparticles of the iron(II)-triazole family within a ferroelectric polymer matrix, poly(vinylidene fluoride-co-trifluoroethylene), P(VDF-TrFE). In certain cases, a polyvinylpyrrolidone (PVP) matrix was also used for prototyping. The composites are fabricated by blade casting, combined with hot pressing, and electrospinning methods, and their characterization employs magnetometry, scanning electron microscopy, calorimetry and dielectric spectroscopy. First, we study the effects of the electrical polarization of the matrix on the SCO properties of the embedded nanoparticles. Additionally, the impact of ferroelectric P(VDF-TrFE) substrates on nanometric SCO films is also explored. Despite a good effective polarization, witnessed by a substantial piezoelectric coefficient d33 of -20 pC/N, we show that the spin-state equilibrium remains unaltered. On the other hand, we evidence subtle matrix effects on the SCO properties. An innovative aspect of the thesis is the development of multilayer devices aimed for thermal energy harvesting. The devices consist of a pyro/piezoelectric P(VDF-TrFE) film, combined with SCO@P(VDF-TrFE) and Ag@P(VDF-TrFE) layers. By leveraging the actuation properties of the SCO material, the devices generate two current outputs under thermal load: one from the ordinary pyroelectric effect and another from the piezoelectric effect induced by SCO thermal strain. Adjusting the sign of the piezoelectric effect allows these contributions to be effectively summed, enhancing the energy harvesting capability of the devices. Finally, the thesis presents two novel approaches for electrically sensing the spin state switching in SCO@polymer composites. The first approach employs a strain sensor made of Ag@P(VDF-TrFE) attached to the SCO@polymer layer, operating through percolation effects. The second introduces a method to study the dielectric permittivity of SCO materials using a radio-frequency resonant tunnel diode oscillator circuit.